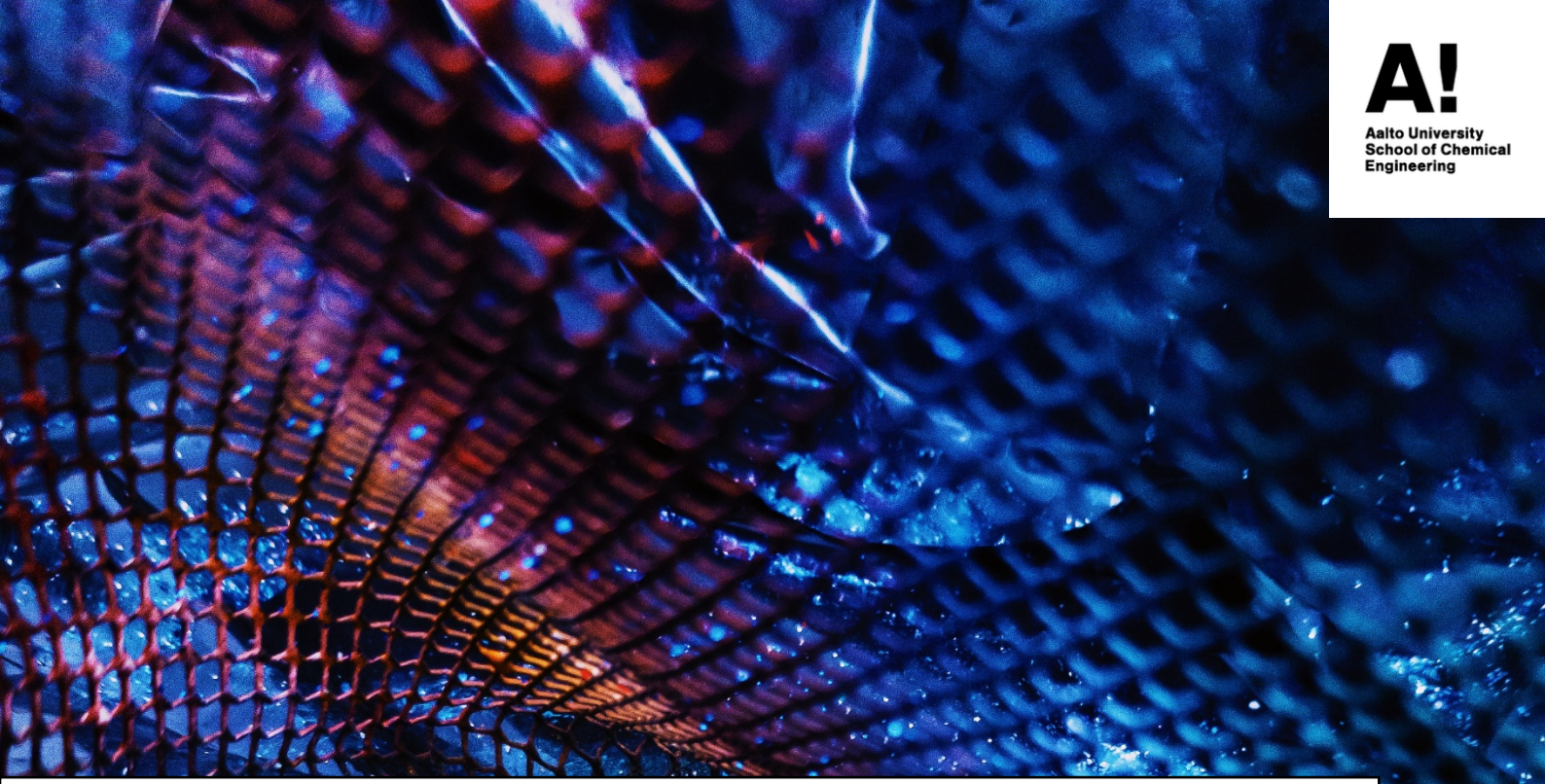

Aalto University
School of Chemical
Engineering

LIGHT RESPONSIVE ACTIVE PLASMONIC SURFACES

Al Hussain, Mohammed Mustafa A

30th July 2021

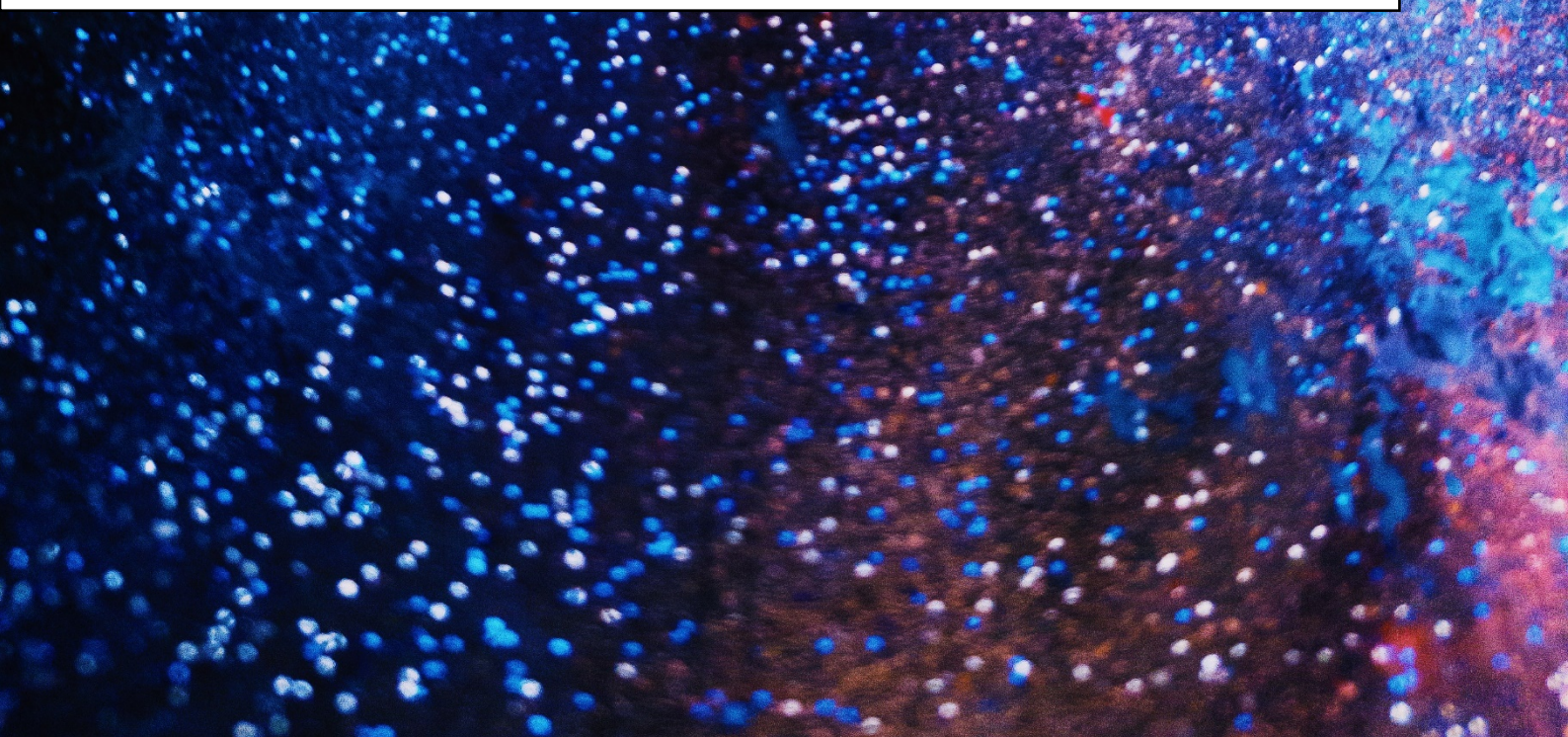

Aalto University
School of Chemical
Engineering

Mohammed Mustafa A Al Hussain

LIGHT RESPONSIVE ACTIVE PLASMONIC SURFACES

Master´s Programme in Chemical, Biochemical and Materials Engineering
Major in Functional Materials

Master's thesis for the degree of Master of Science in Technology submitted for inspection, Espoo, July 2021.

Supervisor Prof. Dr.-Ing. habil. Mady Elbahri

Advisors Assoc. Prof. Anton Kuzyk
Dr. Sesha Sarathchandra Manuguri
MSc. Joonas Ryssy

Aalto University
School of Chemical
Engineering

Aalto University, P.O. BOX 11000, 00076 AALTO
www.aalto.fi

Abstract of master's thesis

Author	Mohammed Mustafa A Al Hussain
Title of thesis	Light Responsive Active Plasmonic Surfaces
Degree Programme	Master's Programme in Chemical, Biochemical and Materials Engineering
Major	Functional Materials
Thesis supervisor	Prof. Dr.-Ing. habil. Mady Elbahri
Thesis advisors	Assoc. Prof. Anton Kuzyk, Dr Sesha Sarathchandra Manuguri and MSc. Joonas Ryssy
Date 30.07.2021	**Number of pages** 92+8 **Language** English

Abstract

The fascination with understanding light started in Greek ancient times. Light plays a vital role in how we perceive the world, which was the main reason behind studying it initially. However, the recent progress and development in technology allowed to harness light to design new applications and materials or enhance existing ones in a wide range of fields from astronomy to nanotechnology. Plasmonic surfaces are a prime example of that. Plasmonic surfaces exhibit unique properties that are traditionally difficult to be achieved in conventional materials, such as a high refractive index, quality factor and resonant absorbance. However, the high cost and the complexity of fabrication have limited plasmonic surfaces and materials. Thus, a system of active plasmonic surfaces is designed here to dynamically tune light for colouration. Initially, this work investigated an existing layer-by-layer (LBL) dip-coating system of polyelectrolytes (PEs) on a thin film of Au with silver nanocubes (AgNCs) used as plasmonic nanoantennas. Excellent colour tuning in the visible spectra region from green to red with good chromaticity was obtained by controlling the number of PEs layers. Moreover, resonant absorption greater than 90% was achieved with a quality factor up to ~ 16.7. Then, the LBL plasmonic surfaces were modified with a photoactive molecule (disperse red 1) to modulate light dynamically. The designed photoactive plasmonics surfaces were exposed to linearly and circularly polarized light for different time durations to tune their properties. Colour tuning in the visible region was possible within a wavelength range of ~ 112 nm. Additionally, the plasmonic sensitivity of the samples was estimated before and after exposure. Overall, the system exhibited an increase in the refractive index and sensitivity with the increase of irradiation time as well as encouraging values of the quality factor and the figure of merit. It is anticipated that the methodology developed in this thesis will advance the development of active plasmonic surfaces that are used for colouration and sensing due to its simplicity, efficiency and low cost compared to current techniques.

Keywords Plasmonics, Photoactive molecules, Silver, Nanocube, Disperse Red 1, Polyelectrolyte, Colours, Sensitivity, Refractive index, Quality factor

Preface

This thesis was submitted as a part of the fulfilment of the master's degree in functional materials at Aalto University. The work was conducted between January and July 2021, and it was a part of the project (Photo-Controlled Active Plasmonics) founded by the Academy of Finland. One of the aims of this project was to fabricate simple, yet effective, plasmonic surfaces for different applications. The work was conducted with the Molecular Nanoengineering Group in the Department of Neuroscience and Biomedical Engineering at Aalto University.

First and foremost, I would like to express my gratitude to my supervisor Prof. Dr.-Ing. habil. Mady Elbahri and advisors Assoc. Prof. Anton Kuzyk (for his understanding), Dr Sesha Sarathchandra Manuguri (for his patience, kindness and positivity) and MSc. Joonas Ryssy (for his encouraging words) as well as thanks for their great help through all this journey. Additionally, I thank all the members of the Molecular Nanoengineering Group for their support and for creating an amazing environment. I would like to express my warmest appreciation also to Dr Jafar Albinmousa for his encouragement and guidance in my whole academic journey. Also, I would like to acknowledge the support we received from our collaborators at Tampere University - Prof. Arri Priimägi and his group.

Furthermore, I would like to send my sincere gratitude to certain individuals who have been giving me continuous support in all its forms: my loving parents, my four beautiful sisters as well as my little brother. Last but not least, I am wholeheartedly thankful to Sir Bergman, who has been unlimitedly giving me his time, care and support here in Finland as well as my sincere friend Esa-Pekka Kortesmaa.

Mohammed Mustafa Al Ali Hussain, Espoo
30.07.2021

TABLE OF CONTENTS

List of The Abbreviations and Symbols

Abbreviation	Definition
AONP	All Optical Nano-Patterning
BSE	Backscattered Electrons
CF_3COOAg	Silver Trifluoroacetate
DMF	Dimethylformamide
DR1	Disperse Red 1
EBE	Electron Beam Evaporator
EC	Electrochromic
EG	Ethylene Glycol
K-K	Kramers-Kronig
LBL	Layer-By-Layer
LC	Liquid Crystal
LED	Light-Emitting Diode
LSP	Localized Surface Plasmon
LSPR	Localized Surface Plasmon Resonance
NC	Nanocube
NIR	Near-Infrared
NP	Nanoparticle
PAH	Poly(allylamine hydrochloride)
PE	Polyelectrolyte
PP	Plasmon Polariton
PSP	Propagating Surface Plasmon
PSS	Poly(styrenesulfonate)
PVP	Poly(vinylpyrrolidone)
rcf	Relative Centrifugal Force
RIU	Retractive Index Unit
rpm	Revolution Per Minute
SE	Secondary Electrons
SEM	Scanning Electron Microscope
SERS	Surface-Enhanced Raman Scattering
SP	Surface Plasmon
SPP	Surface Plasmon Polariton
SRG	Surface Relief Grating
sRGB	Standard Gamut (Red, Green and Blue)
TEM	Transmission Electron Microscope
UV-Vis	Ultraviolet-Visible
vis	Visible
WD	Working Distance

Symbol	Description	Unit
μ	Magnetic Permeability	H/m
Abs	Absorbance	%
c	Speed of Light in Vacuum	m/s
E_o	Electric Field	N/C
FOM	Figure of Merit	-
$FWHM$	Full Width at Half Maximum	nm
k	Extinction Coefficient	-
l	Average Edge Length of Nanocube	nm
Q	Quality Factor	
R	Reflectance	%
R_{co}	Reflection Coefficient	-
S	Sensitivity	nm/RIU
T	Transmittance	%
v	Speed of Light in Medium	m/s
z	Impedance	**Ω**
ε	Electric Permittivity	F/m
ε_r	Real Part of The Dielectric Function	F/m
ε_r	Imaginary Part of The Dielectric Function	F/m
n	Refractive Index	-
n^*	Complex Form of The Refractive Index	-
θ	Angle of Refraction	Degree
λ	Wavelength	nm
λ_{LSPR}	Localized Surface Plasmon Resonance Peak Position	nm
λ_r	Resonance Wavelength	nm
Φ	Phase Change	Degree
ω	Exaction Frequency	Hz

Chapter 1: Introduction

The history of understanding the nature of light started in the Greek civilization around 800 BC [1]. White light consists of multiple electromagnetic waves at different frequencies. The perceived colours of an object are mainly determined by the absorption and reflection of certain wavelengths of these electromagnetic waves by the object. Colours do not only give our world its beauty but they are also used widely in modern applications especially displays [2]-[5]. Moreover, colours have been used for centuries in therapy and marketing as they proved to have an impact on our psychology [6]-[8].

The discoveries and the understanding of light throughout the previous centuries as well as the developments made in nanotechnology have enabled researchers to design materials with useful properties and attractive colours [2], [9]-[12]. Metal nanoparticles due to plasmons, the collective oscillations of electrons, have paved the way to synthesize long-lasting and various colours using the same material without a need to modify the chemical composition [13], [14]. Unfortunately, most of the colouration of surfaces and materials using metal nanoparticles have been either static or not dynamically tuneable in a wide range of the visible spectra region [2], [3], [5], [15]-[19]. Additionally, surfaces with a wide range of dynamic tunability of light and precise colouration generally require complex and costly fabrication methods (e.g., lithography), which reduces their applicability [20], [21].

Hence, this work aims to fabricate active plasmonic surfaces for dynamic colour modulation by utilizing an established simple and low-cost layer-by-layer dip-coating technique [22], [23]. The fabricated surfaces are comprised of silver nanocubes (AgNCs), gold film and a thin spacer layer. Here, a photoactive molecule, namely disperse red 1 (DR1), from the azobenzene family, is incorporated into the thin spacer layer to produce dynamically tuned colours by isomerisation (e.g., cis-to-trans/trans-to-cis). DR1 was used here for light modulation as it is studied well in the literature and is known to have several attractive features for photonic applications, such as All-

Optical Nano-Patterning (AONP), photomechanics and photoinduced birefringence studies [24]-[26]. These features include stability, large dipole moment (i.e., fast alignment of the molecules) and enhancing the photorefractive effect (i.e., the response of materials to light) [27], [28]. Similarly, light was selected here as a stimulus due to its accessibility, speed, remote control and precision. Furthermore, the utility of the fabricated active plasmonic surfaces for surface plasmon sensing was also investigated.

This thesis consists of four main chapters. Chapter 2 provides a theoretical background to guide the reader and provide essential knowledge on the topic from some fundamentals of lights and plasmonics to selected recent fabrication techniques of plasmonic colouration. In chapter 3, a detailed experimental procedure is provided for the synthesis/fabrication and characterization of the fabricated nanostructures and plasmonic surfaces. In chapter 4, the results obtained in this work are presented and evaluated in comparison to other similar systems reported in the literature. Finally, a summary of the main outcomes and future suggestions is given in chapter 5.

Chapter 2: Theoretical Background

The properties and behaviour of light are studied extensively in a major branch of physics called optics. Even though light plays a significant role in our daily life from the sunlight in the early morning to the bed lamp that we use while reading late at night, it is still not fully understood. Colours, most importantly, have always had an influence in shaping societies and have been used since ancient times for symbols and representations [29]. This fascination has continued [30], and thus motivating researchers to create more precise, vivid and environmentally friendly colours as technology advanced [3], [9], [31]. This chapter starts by introducing some fundamentals and effects of light followed by an overview of advanced light modulation techniques. Lastly, common plasmon colouration methods are described.

2.1.Fundamental Features of Light

Light-matter interactions allow us to perceive the world by providing us with visual information. The appearance of the rainbow after a rainy day or the disjoint straw in a glass of water are all examples of the many effects of light that we encounter. The most well-known effects are reflection, refraction, absorption and transmission.

2.1.1. Reflection

Reflection occurs when a wave or a part of it moves back to the medium it originated from after hitting the interface of different media. Reflection of light is referred to as specular if it occurs on a smooth mirror-like surface, while denoted as a diffuse reflection on rough surfaces. As a result, light theoretically reflects at one angle in specular reflection, while diffused at multiple angles from rough surfaces as illustrated in Figure 2.1. However, most of the surfaces in real life are a combination of both. On the other hand, the term reflectance indicates the ratio of the power that is reflected to the incident power.

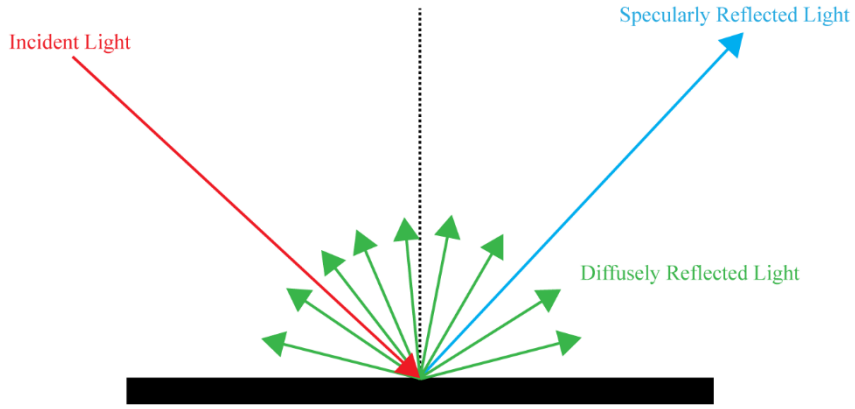

Figure 2.1. A schematic of types of reflection of incident light.

2.1.2. Refraction

Refraction is the bending of light at certain angles after passing through an interface of two transparent media. The relation between the angles due to refraction between two media is expressed by Snell's law[1]:

$$n_1 \sin(\theta_1) = n_2 \sin(\theta_2) \tag{2.1}$$

where θ_1 is the angle of incidence, θ_2 is the angle of refraction, and $n_{1,2}$ are the refractive indices of the media as shown in Figure 2.2.

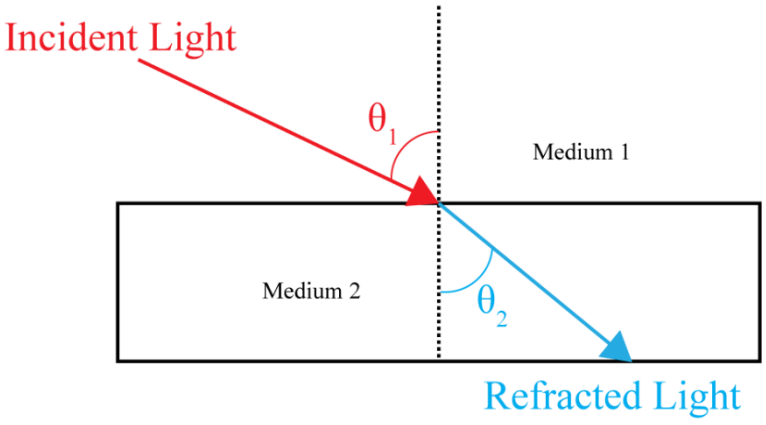

Figure 2.2. A schematic illustrating the Snell's law and the refraction effect.

[1] Recent studies show that the original equation is attributed to Ibn-Sahl (940-1000) [1]. It was a lemma in one of his derivations for a hyperbolic lens.

The refractive index (n) is a parameter defined as the ratio of the speed of light in a vacuum (c) over the speed of light in another medium (v) and can be expressed as follows:

$$n = \frac{c}{v} \tag{2.2}$$

From the above equations, it can be seen that a larger refractive index would generally result in larger refraction. The value of the refractive index is also strongly dependent on the wavelength/frequency of light at which the measurement is taken - higher frequencies often result in larger refractive indices. Other factors including temperature, stress, density and the composition of the material have a weaker influence on the refractive index [32]. Generally, the refractive index is expressed in its full form as a complex number (n^*) as shown in equation (2.3). The imaginary part, which is often referred to as the extinction coefficient (k), represents the strength of the relative absorption loss.

$$n^* = n + ki \tag{2.3}$$

It should be noted that the structure of a material influences its optical properties, and thus its refractive index. Isotropic materials are independent of the direction of travelling light. Thus, they have approximately a constant value of refractive indices for each wavelength as both c and v in equation (2.2) are constant. Gases would normally fall under this category, and a prime example of that is air which has a refractive index of ~ 1 over the whole spectrum. For anisotropic materials, the refractive index would be affected by the direction of the travelling light. Thus, such materials exhibit a range of refractive indices constrained between two extreme values for each wavelength as the speed of light in the medium (v) changes.

2.1.3. Other Effects of Light

Dispersion is an effect of light that results from the variation of the refractive index with the wavelength. This effect can be noticed in the case of the production of different colours of light that resulted from white light dispersed by a prism of glass. The different colours are yielded due to the difference in the angle of refraction at

different wavelengths. Longer wavelengths have larger refractive angles, which means lower refractive indices.

Transmission is defined as the electromagnetic radiation (light) that passes through a medium. As light enters a material, part of its energy would be lost in form of heat, which reduces its intensity. This loss of energy is known as absorption of light. This is an important effect, which indicates that some part of the light is absorbed and thus is neither transmitted nor reflected. The observations and understanding of the fundamental effects of light have opened the door to manoeuvre light on a deeper level utilizing the recent advanced technologies.

2.2. Light Modulation

Light is an electromagnetic wave comprised of oscillating magnetic and electric fields that travels as a transverse wave (i.e., vibrates perpendicularly to its travelling path). However, light waves vibrate in multiple directions along their travelling path. This non-uniformity in the vibrations prevents the utilization of light in direction-dependent applications, such as optical magnifiers [33]-[35]. One of the common tools used to modulate the vibration of light waves are polarizers. A polarizer allows restricting the vibrations of light waves to distinct directions or planes by absorbing the vibrations in other directions. Even though traditional manipulation methods of light (e.g., polarizers) helped to progress the field of optics, it was not until plasmons came into the picture in 1952 and enabled unprecedented possibilities of modulation.

2.2.1. Plasmonics

Nanoscale metal optics, which is simply known as nanoplasmonics or plasmonics, is a field that is concerned with optical phenomena and photonic applications of metal nanostructures [36]. Plasmonics is based on manipulating the electromagnetic waves coupled to the oscillations of free electrons in metals. These oscillations on the metal surface at the metal/dielectric interface are known as surface plasmons (SPs). Plasmon polariton (PP) is the coupling between a plasmon and a photon, and the electromagnetic waves that propagate along the interface are called surface plasmon

polaritons (SPPs). Thus, SPPs enable metal nanostructures to guide the light with nanoscale precision and/or can be used as nanoantennas to propagate, receive and/or transmit electromagnetic waves [37].

Two main types of surface plasmon excitation are supported in plasmonic metal nanostructures: localized surface plasmon (LSP) and propagating surface plasmon (PSP) [38]-[41]. In LSP, the negatively charged cloud of electrons oscillates collectively due to a force generated from the varying electric field with light (E_o). When the collective oscillation matches the resonance of light at a specific excitation frequency (ω), a magnified oscillation is generated that is referred to as localized surface plasmon resonance (LSPR), as can be seen in Figure 2.3A. Nanostructures that exhibit LSPR experience a highly uniform E_o due to their sizes being significantly smaller than the wavelength of the exserted light. On the other hand, structures with PSP experience varied E_o as they have at least one dimension that is close to the excitation wavelength, as shown in Figure 2.3B.

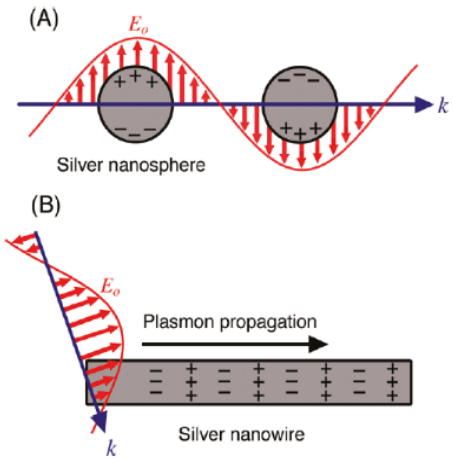

Figure 2.3. Schematic of two types of nanostructures that are excited by the varying electric field of light (E_o) of incident light with wavevector (k): **(A)** Localized surface plasmon resonance (LSPR); and **(B)** Propagating surface plasmon (PSP), adapted with permission from [42]. Copyright © (2011) American Chemical Society.

The ability to focus light in SP modes is highly dependent on the size of the nanostructures [42]. Thus, manipulating the size, environment and shape of metal nanostructures opens the doors for endless ways to tune light effectively in different applications including metasurfaces [43], [44].

2.2.2. Metal Nanostructures

Because of their outstanding physiochemical properties, noble metal nanocrystals have gained significant interest [45], [46]. Today, silver is generally considered the most attractive metal for the development and technology of plasmonics due to its unique properties and high compatibility with a wide range of applications, such as LSPR, surface-enhanced Raman scattering (SERS) and antibacterial and antiviral technologies [42], [47]-[50]. The shape, size and morphology of Ag nanocrystals are among the main factors in determining their physiochemical properties [51]. As a result, Ag nanocrystals with a wide variety of shapes or morphologies can be prepared currently (e.g., cubes, spheres, octahedrons and rods) [52], [53].

Silver exhibits attractive features in both the visible (vis) and near-infrared (NIR) spectra regions as compared to other plasmonic metals, such as Cu, Au and Al [54], [55]. Silver nanoparticles (AgNPs) are able to support a strong SP in a wide range of the spectrum (i.e., 300 to 1200 nm) [40], [56]. The SP mode in NPs is closely related to the dielectric function, which is, in turn, depends on the excitation wavelength. The dielectric function describes the interaction of the electrons of a material with light, and it is an important parameter to determine the quality factor of the plasmonic system. The quality factor (Q), or also known as damping, is commonly used to assess the SP strength as follows:

$$Q = \frac{\omega\left(\frac{d\varepsilon_r}{d\omega}\right)}{2(\varepsilon_i)^2} \tag{2.4}$$

where, ω is the excitation frequency, ε_r is the real part of the dielectric function and ε_i is the imaginary part of the dielectric function.

For plasmonic applications, the value of Q should preferably exceed 10 [42]. The quality factor values of some representative metals are plotted in Figure 2.4. It can be seen that Ag is almost surpassing all the other metals in the full range of 300 to 1200 nm. Additionally, silver exhibits higher values of thermal and electrical conductivities than the rest of the plasmonic metals making it highly attractive in electronics. Unfortunately, silver ions (Ag^+) are limiting silver use because of their

known toxicity and oxidation issues. It should be noted, however, that the material properties of metals have a generally stronger impact in practical applications. This impact is clear as in the case of Li, which has a good quality factor making it an attractive candidate, but it is not widely used due to its high reactivity [42].

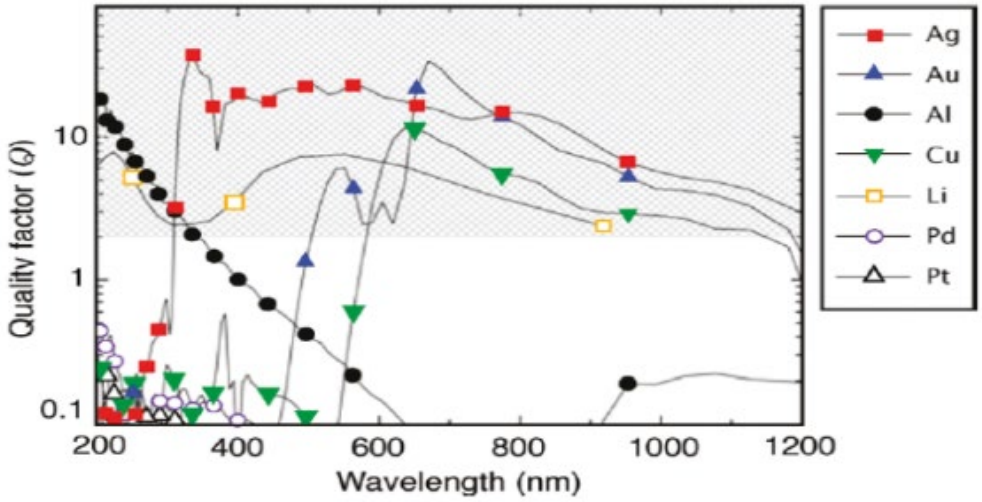

Figure 2.4. Quality factor across a range of wavelength for main plasmonic metals, adapted with permission from [55]. Copyright © 2009 Elsevier.

Size Control

Controlling the size of metal nanostructures is a powerful tool to tune their plasmonic properties, such as the number of modes and peak position of LSPR, PSP localization as well as the absorption to scattering ratio [41], [53], [57]. AgNPs that have a size smaller than 30 nm exhibit stronger absorption relative to scattering [58]. In contrast, those that are larger than 50 nm can scatter light more efficiently [59]. In Figure 2.5A, the size of the AgNPs is around 40 nm (i.e., between 30 and 50 nm), and thus the absorption dominates over the scattering. In comparison, the scattering is more dominant with AgNPs that have a size of 140 nm, as shown in Figure 2.5B. Similarly, the number of the LSPR peaks (i.e., dipole excitations) increases with the increase in the AgNPs size, as seen from Figure 2.5 below.

Additionally, the dipole resonance peak starts to redshift with the increment of size as the frequency of the collective oscillations decreases. This shift is due to the increase of the charge separation on the NPs, which is irrelevant to the shape of the nanostructures [60]. Figure 2.6 shows this trend with AgNCs with varied edge lengths

from 36 to 172 nm. Monitoring such behaviour allows for efficient and accurate control of the size of AgNCs during synthesis (e.g., polyol synthesis) [61], [62].

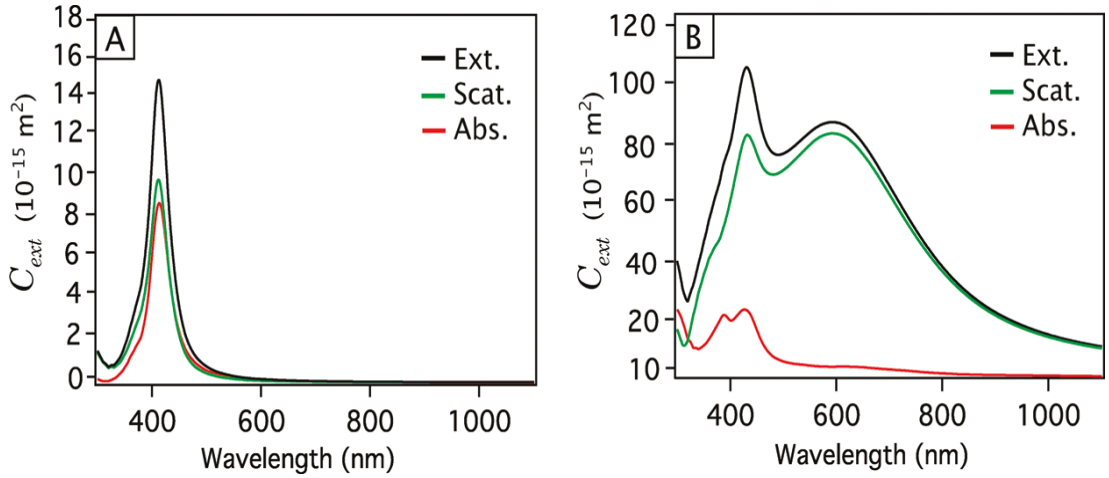

Figure 2.5. Spectra of excitation, scattering and absorption for Ag nanospheres **(A)** 40 nm; and **(B)** 140 nm in diameter, adapted with permission from [43]. Copyright © (2011) American Chemical Society.

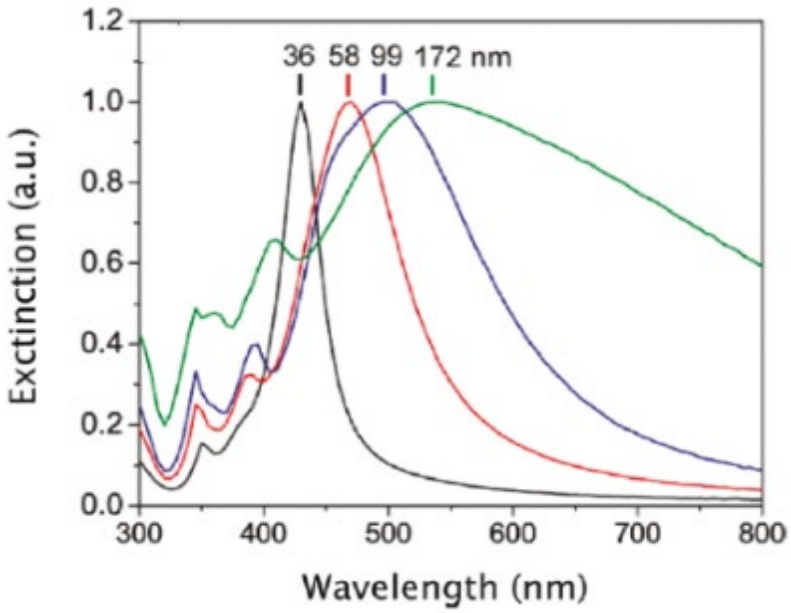

Figure 2.6. Effect of edge size of AgNCs on LSPR, adapted with permission from [75]. Copyright © (2010) American Chemical Society.

Shape Control

As illustrated previously, the size of the NPs affects the plasmonic properties. The same can be said for the geometry including the sharpness of the corners. Generally, the peaks start to redshift as the corners become sharper as can be seen in Figure 2.7.

This shift is due to the reduction of the restoring force for the dipole oscillation and the increase of the charge separation [42].

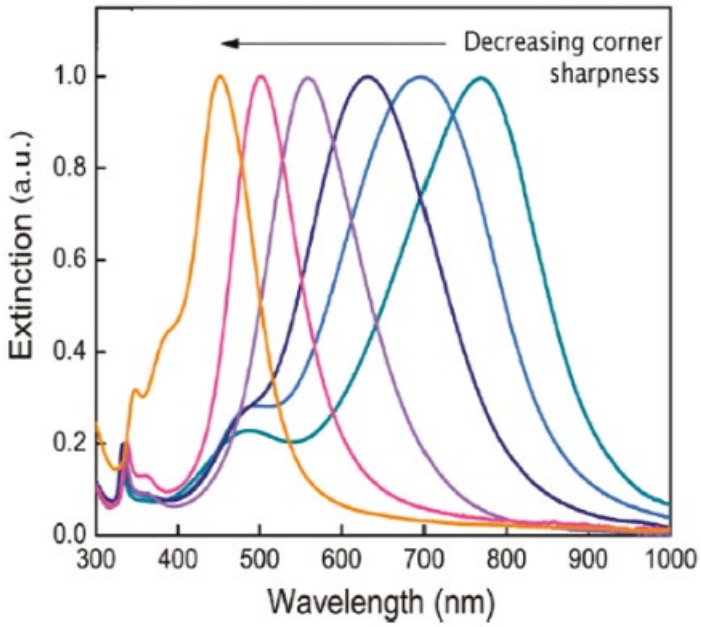

Figure 2.7. Effect on corner sharpness on Ag triangular nanoplates, adapted with permission from [167]. Copyright © (2010) John Wiley and Sons.

Similarly, controlling the shape of the synthesized nanostructures allows for significant modifications and tuning of the plasmonic properties. Figure 2.8 presents the experimental and theoretical extinction spectra of Ag nanostructures of common geometries. Several aspects can be observed from the figure. First, structures with a higher symmetry ratio have a fewer number of resonances (e.g., sphere vs cube). The symmetry can also affect the strength of absorption and scattering [53]. Centrosymmetric geometries (e.g., cubes, octahedrons) tend to support strong dipole excitation due to charge separation into the corners of the structure [42]. Second, a redshift is observed in LSPR peaks for geometries with sharp corners (e.g., cubes) because of the relatively large charge separation and low restoring force [63], [64].

Table 2.1 below shows a comparison between different plasmonic metals. Based on the previously presented data as well as the ones shown in the table, it can be seen why silver seems to get most of the attention in plasmonics as it offers an excellent

combination of a high-quality factor, a wide range coverage in the spectrum, attractive material properties and a relatively low price.

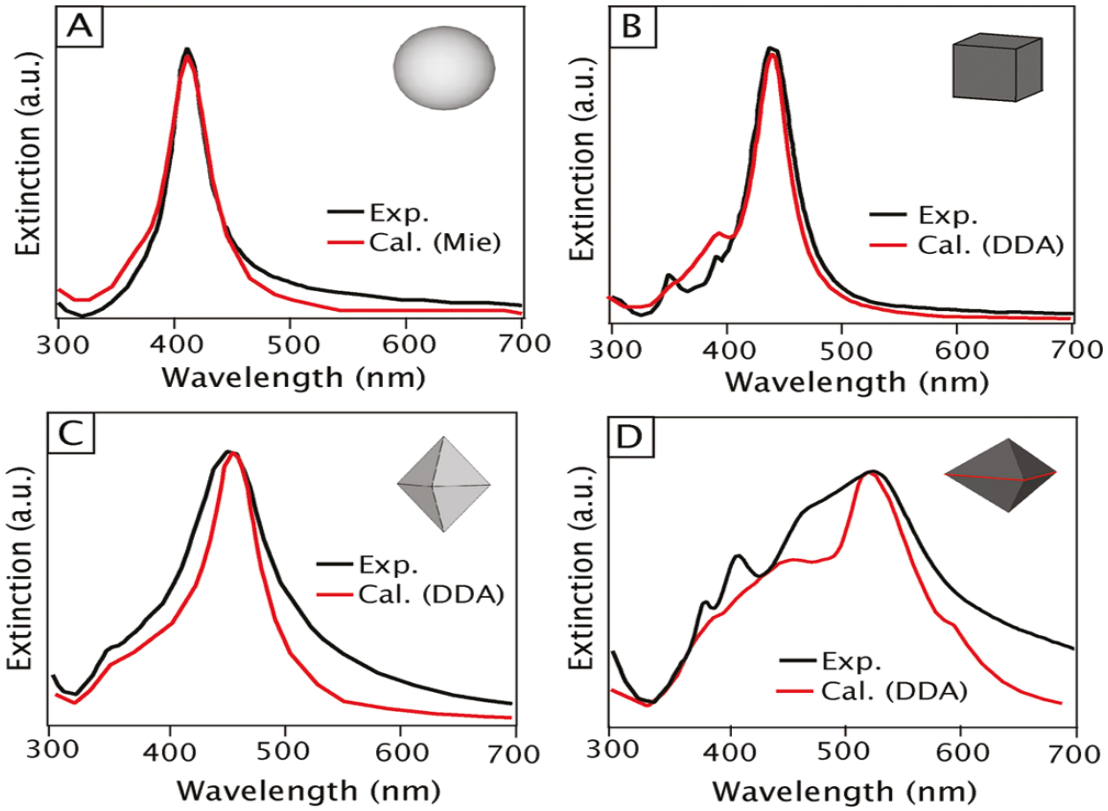

Figure 2.8. Experimental and calculated extinction spectra for silver: **(A)** spheres, **(B)** cubes, **(C)** octahedrons, **(D)** and right bipyramids. (A-C) have a diameter/edge length of 40 nm, while the edge length in (D) is 75 nm, adapted with permission from [42]. Copyright © (2011) American Chemical Society.

Table 2.2 below presents different silver nanostructures and their applicability in the plasmonic field. Furthermore, plasmonic nanostructures are extensively used in molecular spectroscopies [65], [66] and refractive index sensing [67], [68], as they generate noticeably high localized electric fields [69]. Coupling for plasmonic nanostructures, such as clusters [70] and dimers [71]-[73], depends strongly on the gap between them and is used to control the optical properties [69].

Taking it a step further, researchers have investigated incorporating stimuli-responsive materials into plasmonic surfaces to achieve further modulation of the properties. There are six main types of stimuli used to manipulate the plasmonic behaviour of metal nanostructures: i) chemical [74]; ii) mechanical [75]; iii) optical [76]; iv) thermal [77]; v) electrical [78]; and vi) magnetic [79]. However, optical modulation offers a

number of attractive features. First, both natural and synthetic light is relatively easy to access. This leads to the second point that is different responses can be triggered in the material using various wavelengths [80]. Third, the light-responsive materials can be remotely controlled without direct contact [81]. Furthermore, light travels at high speed in most of the media allowing it to be delivered near instantly. Additionally, the irradiation of light can be precisely controlled and directed to specific locations of the material resulting in a material with multiple properties. Consequently, light-responsive materials and surfaces have been studied extensively, especially the azobenzene family [82]-[86].

Table 2.1. A comparison of different metals for plasmonic application, edited with permission from [42].

Metal	Plasmonic Ability	Chemical	Nanostructure Formation	Cost ($/oz)
Aluminium (Al)	Good in UV region	Stable after surface passivation	-Limited nanostructures -Used in lithographic patterning	0.049
Copper (Cu)	Interbrand transitions below 600 nm	Easy oxidation	Limited nanostructures	14.8
Gold (Au)	-Interbrand transitions below 600 nm -High-quality factor	-Very stable -Biocompatible	Multiple structures	950
Palladium (Pd)	-Low-quality factor -Not suitable for plasmonics	Stable	Multiple structures	265
Platinum (Pt)	-Low-quality factor -Not suitable for plasmonics	Stable	Multiple structures	1207
Silver (Ag)	Very high-quality factor	-Oxidation -Biocompatibility issues	Multiple structures	13.4

Table 2.2. A comprehensive summary of different shapes of silver nanostructures, reproduced with permission from [42]. Copyright © (2011) American Chemical Society

Shape	Illustration	LSPR [nm]	Applications	Method of Synthesis
Sphere and quasi-sphere	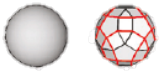	320-450	-SERS -LSPR sensing -Assembly	-Polyol process (single-crystal) -Citrate reduction (quasi-sphere)
Cube and truncated cube		400-480	-SERS -LSPR sensing -Assembly	-Polyol process -Seed-mediated growth
Tetrahedron and truncated tetrahedron		350-450	SERS	-Polyol process -Light-mediated growth
Octahedron and truncated octahedron	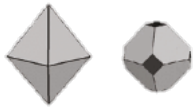	400-500	Assembly	-Polyol process -Light-mediated growth -Seed-mediated growth
Bar		350-900	SERS	Polyol process
Spheroid		350-900	SERS	Polyol process
Right bipyramid		500-700	-	Polyol process
Beam		-	Electron transport	Polyol process

(Continued)

Shape	Illustration	LSPR [nm]	Applications	Method of Synthesis
Decahedron		350-450	-	-Citrate reduction -Light-mediated growth -Seed-mediated growth
Wire and rod		380-460	-Waveguiding -Electronics -SERS -Assembly	Seed-mediated growth
Polygonal plates and disc	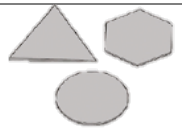	350-1000	-SERS -LSPR sensing	-Polyol process -Light-mediated growth
Branched structures		400-1100	SERS	Seed-mediated growth
Hollow structures		380-800	-SERS -LSPR sensing	Template-directed growth

2.2.3. Photoactive Molecules

Photoactive molecules alter the optical properties by influencing the refractive index as well as the birefringence. Photoactive molecules from the azobenzene family have demonstrated their suitability for a wide range of applications including colouration and electro-optic liquid crystals [87]. The azobenzene disperse red 1 (DR1) is an example of a molecule with such behaviour, and its chemical structure is shown in Figure 2.9A. DR1 yields noticeable changes in the refractive index once exposed to light around the absorption resonance due to its trans-cis isomerization nature [88]. In the azobenzene class of chromophores, two phenyl groups can be linked using the azo bond (- N = N -), which provides the enhanced optical properties and absorption of light [89]. The photochemical isomerization of DR1 (i.e., the absorption of a photon by the chromophore) is essential to obtain thermally stable states (i.e., trans- and cis-). Irradiating DR1 with light at specific wavelengths allows for switching between the cis-trans isomerization states, as can be seen in Figure 2.9B.

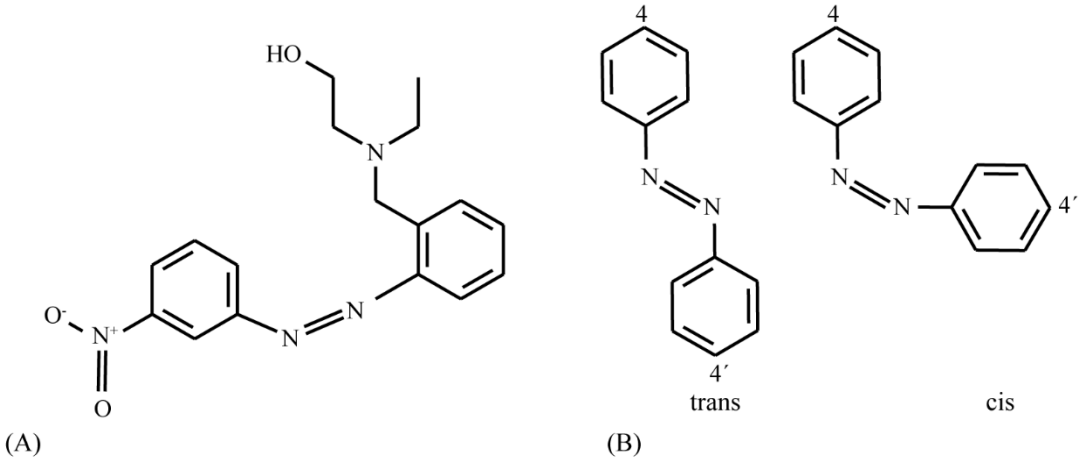

Figure 2.9. (A) Chemical structure of disperse red 1; and **(B)** The trans-to-cis conversion in azobenzene.

DR1 is specifically from the pseudo-stilbenes class, which is known for its excellent photo-switching ability due to its: i) strong asymmetric electron distribution (i.e., push/ pull substitution pattern); ii) large and wide absorption in the visible regime; and iii) nonlinear optical properties – as a result of the asymmetry of the electron distribution [87], [88], [90].

The significant changes in the refractive index observed using DR1 are attributed to: i) the reduction in the distance between the two carbon atoms; ii) change in the dipole moment of the molecule; and iii) alteration of the polarizability of the material [90]. Irradiation with polarized light can results in alignment of the chromophores in DR1, while illumination with circularly polarized light (or in some cases unpolarized light) can restore the random distribution [88], as shown in Figure 2.10. Based on what has been discussed so far, the attractive features of plasmonic nanostructures (e.g., SPs and LSPRs) coupled with light-responsive materials have the potential to shift the implementation of colours in technologies, such as displays, significantly.

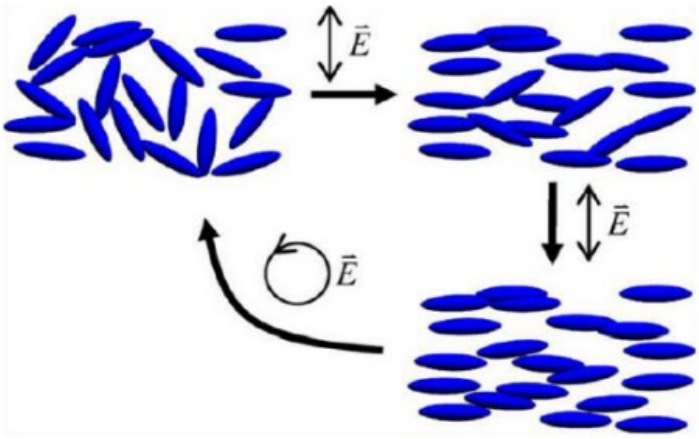

Figure 2.10. Photo-isomerization and reversibility of disperse red 1, edited with permission from [57]. Copyright © (2006) Elsevier.

2.3.Plasmonic Colours

Colours generated due to the resonant interactions between the metallic nanocrystals and light are known as plasmonic colours. Plasmonic colours are independent of the angle of viewing, which means that they appear the same from different angles. In addition, they have excellent durability, if coated, against colour alteration due to long exposure to sunlight, bleaching and abrasion [21]. An excellent example of their durability is the popular ancient stained glass [91]. Furthermore, plasmonic colours extend the spatial resolution to the submicrometre range. Thus, for example, plasmonic colours can be integrated into security applications that are not possible to be

performed with the naked eye [92]. Figure 2.11 compares different colouring techniques based on five key parameters.

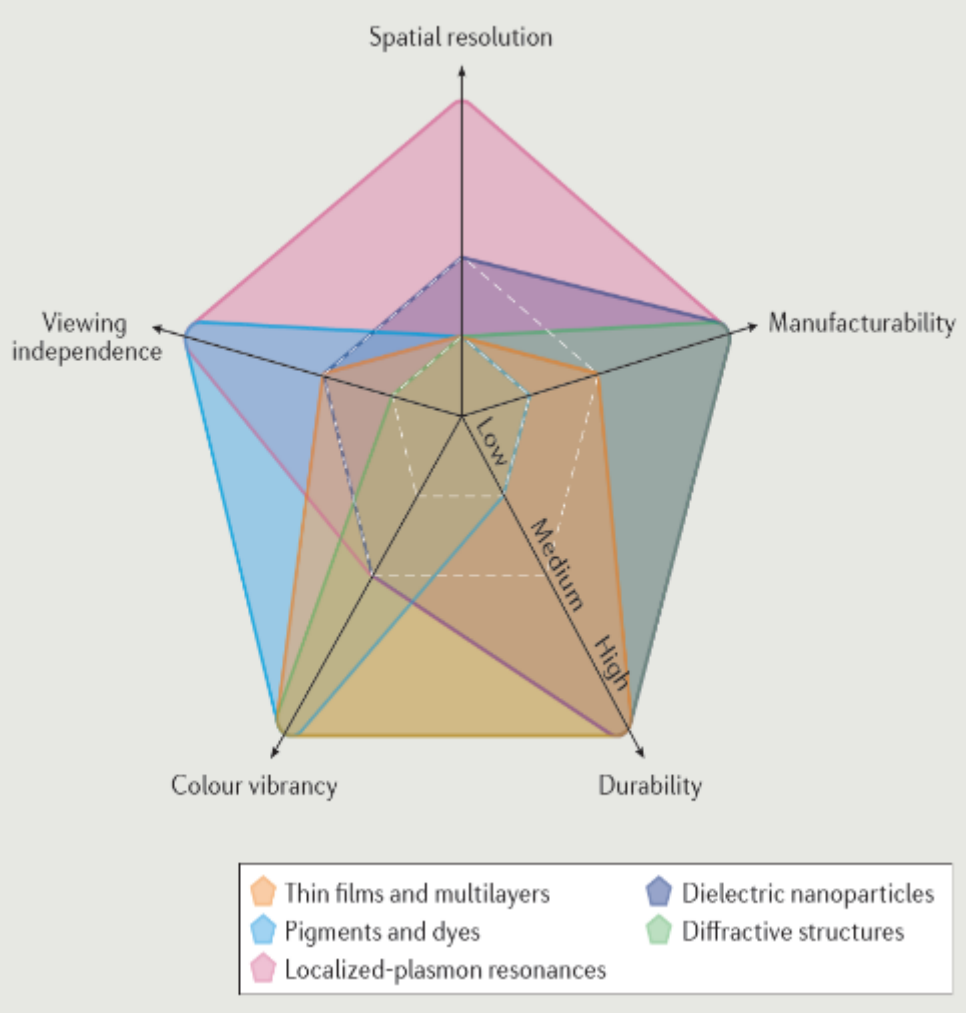

Figure 2.11. Technology performance indicators: spatial resolution, manufacturability, durability, vibrancy and viewing independence, adapted with permission from [21]. Copyright © (2016) Springer.

The tight confinement of the light energy by LSPRs is a critical factor for obtaining high-resolution plasmonic colours. It is known that nanoantennas absorb and scatter light with wavelengths larger than their physical cross-sections, as can be seen in Figure 2.12 [93]. All the presented groups in the figure have sizes smaller than the wavelength of light in the visible spectra region. However, only plasmonic nanocrystals have extinctions that surpass their physical cross-sections. Additionally, plasmonic colours can be adjusted by nanocrystals as synthetically tuneable LSPRs are supported [94], thus opening the doors for different colouration techniques.

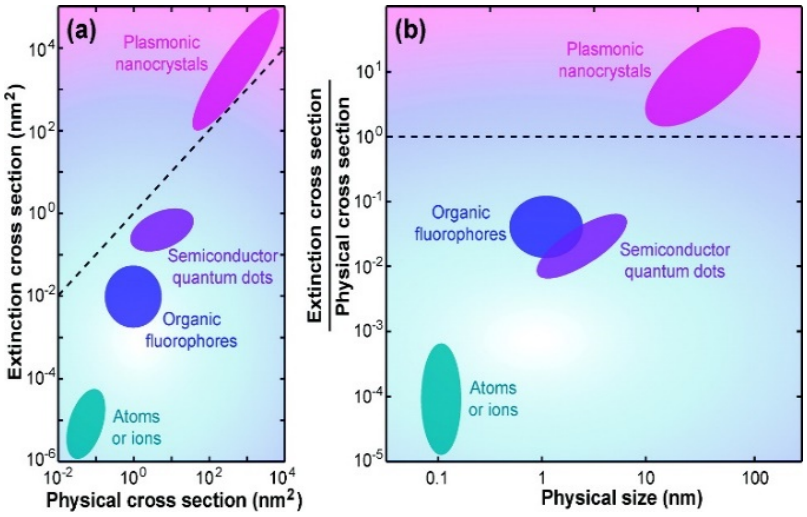

Figure 2.12. A comparison of different nanoscale optical materials in terms of: **(a)** The extinction cross section against the physical cross section; and **(b)** The extinction over physical cross sections against the physical size of the optical material, adapted with permission from [81]. Copyright © (2012) American Chemical Society.

2.4.Plasmon Colouration Methods

Dynamic plasmon colour generation schemes have two main parts: i) colouration mechanism, which involves the method that the colours are generated by (e.g., varying the size or the dielectric properties of the nanostructures); and ii) colouration control, which underlines the techniques utilized to tune the generated colours experimentally (e.g., light, gases, electric and magnetic fields or pH). In this section, different common methods that utilize plasmonics for colour generation and modulation are presented.

2.4.1. Electrochemical Deposition

Electrochemical cells consist of two main electrodes (i.e., a working electrode and counter electrode) and metal ions with all the components placed in an electrolyte solution. The metal ions are deposited onto an electrode, usually in the form of metal nanoparticles once they get reduced by applying a voltage. On the other hand, applying an inverse voltage oxidizes the deposited metals, and thus dissolving them back.

Electrochemical deposition can be used to control the colouration by tuning the size of the nanoparticles, as presented in Figure 2.13A. It is well documented that the

perceived colouration from nanoparticles and the LSPR is highly dependent on the charge distribution on their surfaces [64], [95]. For small particles, the excitation of dipolar mode governs the resonances. With the increase of the particle size, there would be a decline in the restoring force (i.e., Coulombic force that drives the electron cloud to its original position) leading to a redshift of the plasmonic band [9]. Furthermore, changing the size of the particle would have a noticeable effect on the interparticle distances between the nanoparticles. The near-field or far-field coupling plays an important role in the plasmonics modes depending on the separation distance between the nanoparticles [96]. After fabrication, however, controlling the separation distance between particles and/or their size is generally hard to achieve, and thus reducing the practicality of the method [9].

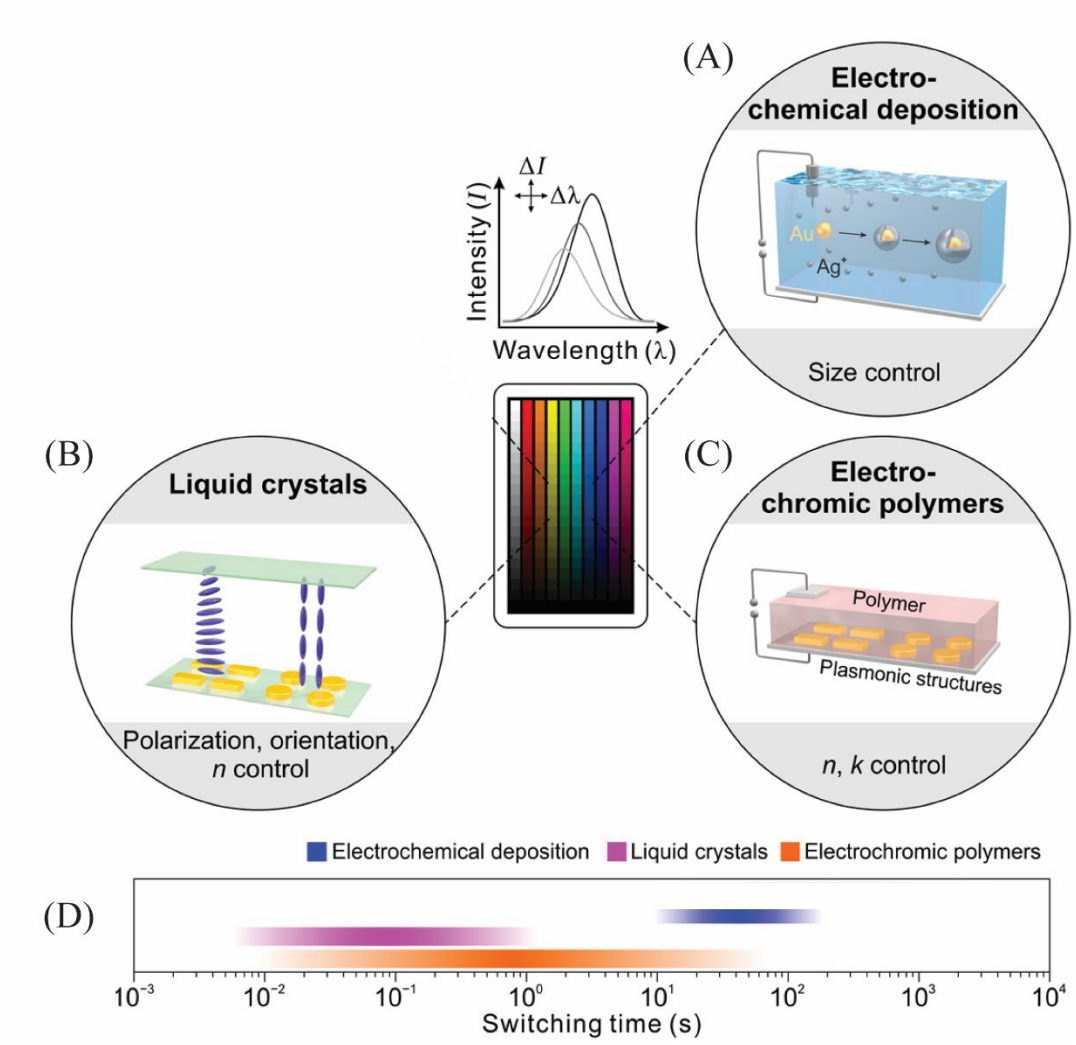

Figure 2.13. Some dynamic plasmonic colour generation methods: **(A)** Electrochemical deposition, **(B)** Liquid crystals, **(C)** Electrochromic polymers, and **(D)** A comparison between the methods in terms switching time, edited with permission from [9]. Copyright © (2020) American Association for the Advancement of Science.

Surfaces and nanostructures of metals and metal oxides can be deposited with precisely controlled layers on the nanometre scale using electrochemical deposition [97]. Thus, this method has been investigated to generate dynamic plasmonic colours by several research groups [98]-[101]. For example, Araki *et al.* [98] used silver ions in a gel electrolyte and two electrodes made of indium tin oxide (ITO), with one being flat while the other is particle-modified. The cell appeared black when the deposition of Ag was done on the particle-modified electrode. This was attributed to the absorption and/or scattering of light by the Ag particles that aggregated. In contrast, the cells appeared as a silver mirror as the Ag particles were deposited on the flat electrode resulting in a specular reflection. In 2013, the same group was able to expand the concept to generate red and blue colours by controlling both Ag particles nucleation and growth with a varied voltage [99].

The electrochemical deposition has been successfully used to produce dynamic plasmonic colours that cover the whole visible region of light with acceptable brightness [9]. However, this method has a few limitations including the low purity and durability of colours as well as the colouration time [9].

2.4.2. Liquid Crystals

Liquid crystals (LCs) have unique properties due to their liquid-solid intermediate state that enables them to be implemented in a wide range of applications (e.g., liquid crystal displays, cellphones and synthetic biodegradable materials) [102], [103]. An interesting characteristic of LCs is the ability to switch their birefringence (i.e., the orientation of their constituent molecules) electrically, optically or thermally infinitely without a decline in the quality within milliseconds [9]. This is illustrated in Figure 2.13B and Figure 2.13D.

Neubrech *et al.* [9] described three main mechanisms used to generate/modulate plasmonic colours dynamically by LCs. The first mechanism is related to their birefringent nature. Unique colours can be obtained by selecting specific polarization states of plasmonic excitation if LCs are combined with a polarizing element. This is

because of the anisotropic nature and birefringence allowing for excellent tuning of the polarization state of light. The second method of colour tuning can be achieved by controlling the refractive index of LCs around the nanostructures optically or electrically. This can be attributed to the variation of the plasmonic resonance frequency associated with the change in the refractive index. The third mechanism is based on dispersing anisotropic nanoparticles in LCs and then aligning them with an electrical field. After that, distinct plasmonic colours, as well as polarization states, can be obtained with the help of a polarizer.

Overall, LCs offer fast switching times and can be integrated easier than other methods because of the existing knowledge about them. Some of their shortcomings include: i) thick layers of polarizers with LCs cells (i.e., micrometre range); ii) relatively low reflection efficiency; iii) fabrication complexity; and iv) relatively high-power consumption [9].

2.4.3. Electrochromic Polymers

Electrochromic (EC) polymers (e.g., polypyrrole and polyaniline) can be used to generate/modulate colours under controlled redox reactions, as shown in Figure 2.13C. The method is based on producing variations in the absorption of colours resulted from changes in the dielectric function of the material. This leads to a drastic change of the electronic properties of the conductive polymers during one of the redux processes (i.e., reduction or oxidation) [104].

The outstanding reversibility and excellent control over different redux states have enabled EC polymers to be one of the most promising materials for several applications (e.g., electrochromic strips) [105]. The low cost and power consumption as well as the vibrant colour associated with EC polymers make them especially attractive for reflective displays, such as electronic billboards and papers [9]. Unfortunately, among the major drawbacks hindering their implementation commercially is the large thickness of polymers needed to generate suitable contrast. Such thick layers lead to significantly longer switching times due to the constrain of ionic diffusion, thus, making them impractical [4].

Furthermore, the contrast is also dependent on the availability of high electrochemical potentials, which decrease the quality of the polymers significantly. Additional conjugated polymers and space layers are required to incorporate sub-pixels in order to cover the whole visible spectra range. However, this leads to a decline in the switching time, reflection efficiency and further complexity in the fabrication process [9]. Fortunately, hybrid systems that join plasmonic nanostructures with EC polymers have the potential to surpass these obstacles. The thick layers of EC polymers can be replaced with thinner layers in the hybrid systems by placing them in the plasmonic hotspots.

2.4.4. Layer-By-Layer Deposition

Another emerging method to modulate light for colouration is based on plasmonic resonators/nanoantennas on thin metal surfaces. The nanoantennas (i.e., usually colloidal metallic nanoparticles) are deposited on a metallic thin film (e.g., Au or Ag) with a varied number of layers of mostly polyelectrolytes (PEs) in between. The different layers of the system need to be coated such that they have alternating charges. For example, if the substrate has a negative charge, then the next layer needs to be positively charged and *vice versa*. This allows for excellent adhesion, and thus better

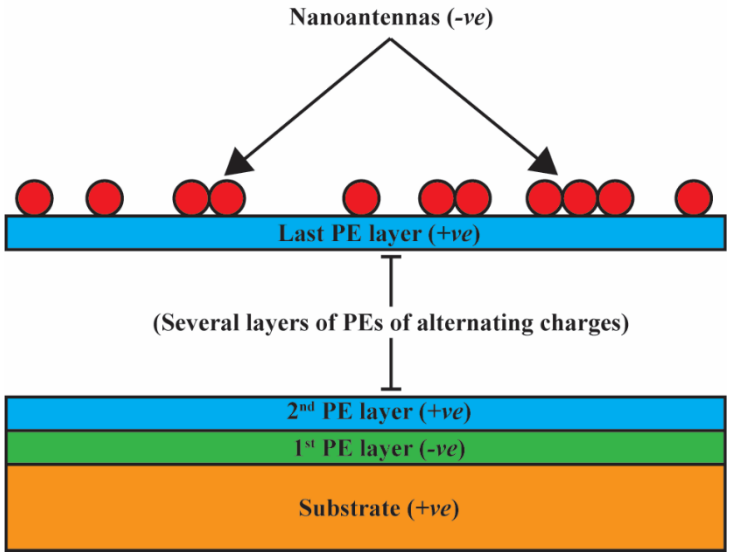

Figure 2.14. A schematic illustration of a typical configuration plasmonic surfaces using the LBL technique.

properties and predictability. A typical configuration of this system is shown in Figure 2.14.

The layer-by-layer deposition provides significant simplicity due to its few nondemanding steps of the overall fabrication process (i.e., mainly dip-coating and colloidal synthesis) making it highly attractive for large scale productions. Also, it allows for a wide range of spectral tuning of around $\Delta\lambda \sim 800$ nm based on the gap layer and the size of the nanoparticles [22]. Additionally, the optical properties can be controlled effectively by changing the surface coverage density and/or plasmonic properties of nanoantennas (e.g., material and shape) [23], [106]. This technique, however, has a number of limitations. First, the nanoantennas need to be optimized and arranged carefully to match the impedance of the plasmonic surface to produce consistent results [22]. Second, the plasmonic gap needs to be controlled with nanoscale precision for accurate tuning of the plasmon resonances. Even though this method is simple, highly effective and has great potential, the required initial optimization of the parameters of the system, such as the desired size of NPs, can be challenging and time-consuming.

In summary, using plasmonic nanostructures to generate or tune colours offers several attractive features. First, thin layers (<1 μm) can generate highly intense colouration due to fields enhancement and the strong interaction with light [107]. Second, they have greater colour stability over a long period of time compared to traditional dyes. This is especially noticeable in noble metals, such as gold and silver. Third, plasmonic nanostructures can achieve significantly high resolutions over relatively large areas [108], [109]. Table 2.3 below summarizes the different designs of nanostructures and their suitability for plasmonic colouration, while Table 2.4 presents a comparison between the three common categories of plasmon colouration for displays.

Table 2.3. Summary of main designs of nanostructures for plasmonics colour generation, reproduced with permission from [21]. Copyright © (2016) Nature.

Nanostructure Design	Known Properties	Drawbacks
Nanoantennas above a back-reflector including, continuous metal–insulator–metal (MIM) disk arrays and holey back-reflectors (hybridized antenna-hole arrays)	-Suited for reflection-mode operation with high-resolution [~ 100,000 dots per inch (DPI)] -Colour control at the single nanoantenna level -Viewing-angle independent (for subdiffraction periodicities) -Polarization dependence (with asymmetric geometries)	-Limited colour gamut -Tight critical-dimension control in fabrication (sensitive colour dependence on nanoantenna dimensions)
Nanoantenna arrays, including isolated metallic structures on transparent substrates.	-Suited for transmission-mode operation or dark-field illumination -Polarization dependence (with asymmetric geometries) -Vivid colours (when combined with diffractive effects)	-Low reflectance -Viewing-angle dependent
Hole arrays above back reflector	-Suited for reflection-mode operation -Colours sensitive to periodicity of array -Near-perfect absorption	-Limited colour gamut -Limited spatial resolution (owing to periodicity requirement)
All-metallic structures, including nanopost and nanotrench structures	-Suitable for reflection-mode operation -Single constituent material -Near-perfect absorption -Viewing-angle independent	-Limited colour gamut -Challenging fabrication

Table 2.4. A comparison of major plasmonic colouration techniques in displays, reproduced with permission from [3].

Specification	LC modulation	Reversible electrodeposition	Electrochromic switching
Colour spectrum	Full colour	Full colour	Full colour
Colour contrast	Low	Very high	High
Reflectivity/brightness	>20%	>20%	>20%
Spatial resolution	≈10,000 PPI	-	≈10,000 PPI
Largest viewing angle with correct colours	≈20º	-	≈60º
Refreshing rate	≈14 Hz	<1 Hz	≈1-100 Hz
Switching mechanism	-Polarization modulation -Refractive index tuning -Orientation modulation	Material/shape change of plasmonic structures	-Intensity modulation -Refractive index tuning
Compactness/thickness	Medium	Low	High
Flexibility	Limited	Limited	High
Energy efficiency	High	High	Very high
Lifetime	-	>200 cycles	>10,000 cycles
Cost	High	Low	High
Compatibility with existing industry	High	Low	Medium
Critical issues for practical applications	-To increase colour contrast -To improve refreshing rate	-To prolong the lifetime -To improve refreshing rate -To enhance the spatial resolutions -To improve compactness	-To improve compactness -To enhance refreshing rate

Chapter 3: Experimental Implementation

This chapter starts by briefly describing the working principles of instrumentations used for the characterization in this work. Then, the synthesis method for silver nanocubes (AgNCs) is given followed by a description of the characterization. Finally, the fabrication processes used to prepare the active plasmonic surfaces are presented along with the tools, techniques and equations that are utilized for the analysis and characterization.

3.1. Instrumentations

3.1.1. Scanning Electron Microscopy

A scanning electron microscope (SEM) utilizes a beam of focused electrons into a small probe to scan the surface of the sample. Several signals (e.g., X-rays, Auger electrons, secondary electrons) are generated as a result of the interaction between the beam and the atoms in the sample. Thus, information about the surface topography and composition can be obtained by detecting these signals and correlating the signal intensity with the probe position. SEM can be used for a wide variety of applications by selecting the proper signals. The main operation modes of SEM are based on: i) the secondary electrons (SE), which are used to study the surface morphology; ii) the backscattered electrons (BSE) utilized for compositional imaging (e.g., multiphase structure); and iii) X-rays, which are typically used for compositional analysis (e.g., elemental mapping). SEM is generally limited by the vacuum environment and the need for conductive coating for the samples.

3.1.2. Transmission Electron Microscopy

A transmission electron microscope (TEM) is similar in many aspects to a transmission light microscope but consists of additional parts: i) an electron source; and ii) electromagnetic lenses (i.e., condenser, objective and projector). TEM operates under

a vacuum to prevent the depletion of the energy of electrons due to the collision with air molecules. Samples need to be relatively thin for the electron beam to pass through them and meaningful results to be obtained. As in the case of SEM, TEM is capable of performing different types of characterization, such as crystal structure and chemical analysis. Additionally, it provides images with high resolutions that enable accurate analysis of the quality, size, shape and density of nanostructures.

3.1.3. Electron Beam Evaporation

An electron beam evaporator (EBE) operates starting with the heating of a tungsten filament by applying current to emit electrons. Then, high voltage is applied to accelerate the electron beam, which is focused with a magnetic field, towards a crucible with the material intended for deposition. The material then begins to evaporate gradually due to the transformation of energy from the electrons and deposits onto the substrate. EBE offers several attractive features over conventional coating methods (e.g., resistive thermal evaporation) including: i) high deposition rate; ii) high evaporation temperature allowing for more options of materials to be used (e.g., Ti and Ta); iii) higher purity of deposition; and iv) evaporation of different materials using one electron source.

3.1.4. Ultraviolet-Visible Spectrophotometry

An ultraviolet-visible (UV-Vis) spectrophotometer is a device used to measure the absorption, transmission or reflectance of light by a material against the wavelength. Generally, molecules transfer from ground to excited state after light absorption leading to atomic excitation. In a UV-Vis spectrophotometer, the sample and a reference (e.g., an aluminium mirror or a blank solution) are exposed to several monochromatic wavelengths that are being recorded in one of the three modes described earlier (i.e., transmission, absorption or reflection). Additionally, a UV-Vis spectrophotometer can be used to determine the concentrations of substances in the sample as well as tracking chemical reactions.

3.2.Silver Nanocubes

3.2.1.Synthesis

A polyol synthesis procedure was used to synthesize the AgNCs in three main stages. First, aqua regia solution was used to clean all the glasswares used for 30 min. Then, the glasswares were washed with plenty of purified water and were dried later using nitrogen.

Second, a 50 mL round bottom flask was filled with 5 mL of ethylene glycol (EG, 99%+ extra pure, Acros Organics), and then was heated at 151 ºC and placed in an oil bath. After 40 min, 60 µL of sodium thiosulphate (NaSH, Sigma-Aldrich, 3 mM in EG) was added rapidly into the heated solution. A minute later, 450 µL of hydrochloric acid (HCl, Fisher Scientific, 3 mM in EG, MW ~ 36.46 g/mol) prepared by diluting 1 M aqueous HCL solution by EG was added into the mixture. Immediately, 1.2 mL of poly (vinylpyrrolidone) (PVP, Sigma-Aldrich, 20 mg / mL in EG, MW ~ 55,000 g/mol) was added into the flask. After two minutes, 400 µL of silver trifluoroacetate (CF_3COOAg, Sigma-Aldrich, 282 mM in EG) was added to the solution. The solution was kept for 90 min for the reaction to complete. The solution was stirred at 300 revolution per minute (rpm) using a temperature-controlled magnetic stirrer (AREX-6 Digital Pro, VELP® Scientifica Srl). The flask was kept closed with a glass stopper during the full synthesizing process.

Third, the flask of the mixture was quenched in an ice bath until it cooled down. Next, the mixture was transferred into a 50 mL centrifuge tube and centrifuged twice using an electric lab centrifuge (Megafuge™ 16R Centrifuge, Thermo Fisher Scientific) at 14,000 relative centrifugal force (rcf) for 12 min to remove excess PVP. After each centrifugation, the supernatant was discarded, but the pellet was washed with acetone the first time and with purified water the second time. Finally, the synthesized AgNCs were re-dispersed in 1.5 mL of purified water and stored at 4 ºC. The main steps of the synthesis process are summarized in Figure 3.1.

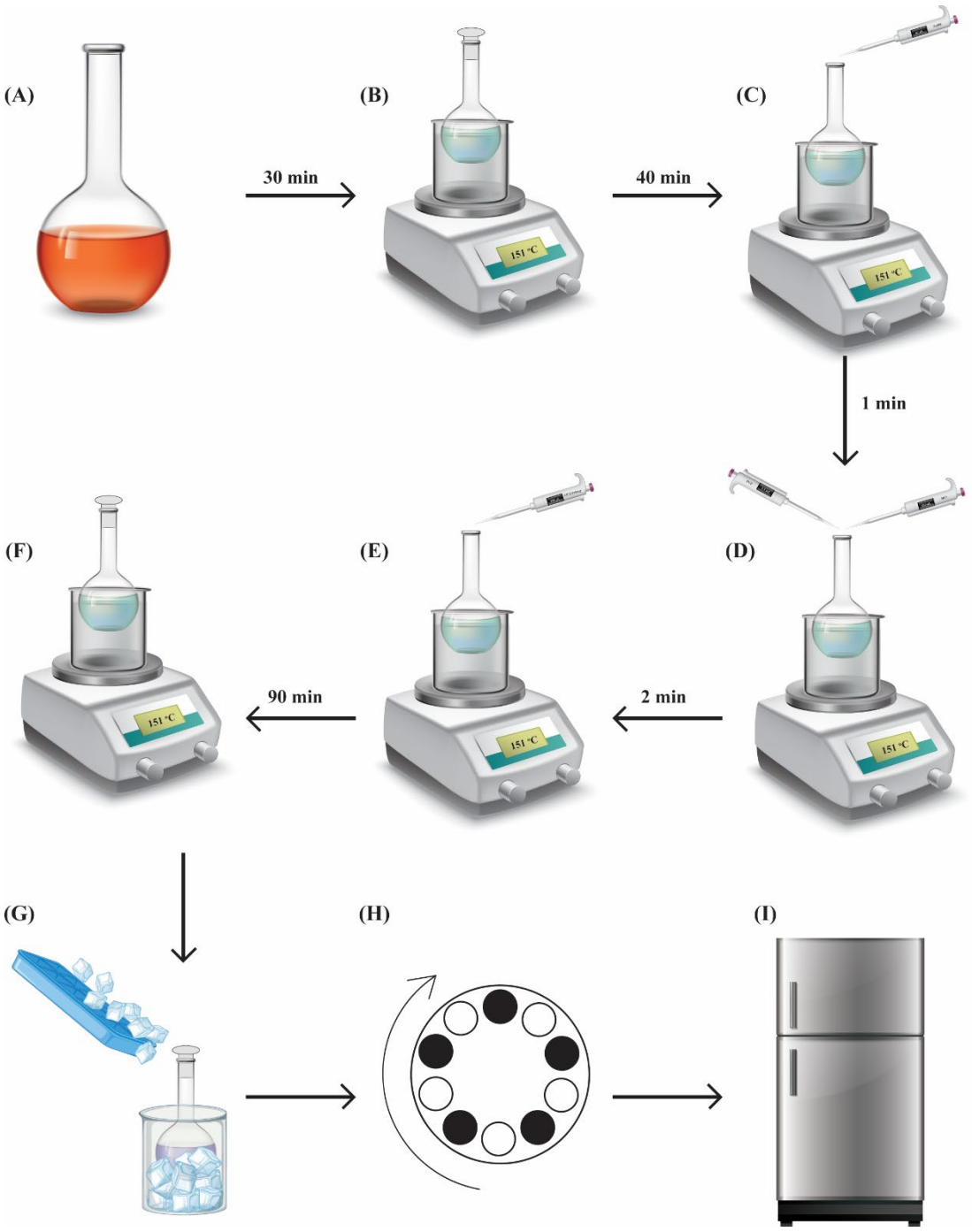

Figure 3.1. AgNCs preparation process: **(A)** Cleaning glassware with aqua regia solution for 30 min; **(B)** Heating 5 mL of EG in an oil bath at 151 ºC for 40 min; **(C)** Adding 60 µL of NaSH; (D) Adding 450 µL of HCl and 1.2 mL of PVP; **(E)** Adding 400 µL of CF_3COOAg; **(F)** Processing for 90 min; **(G)** Quenching the solution in an ice bath; **(H)** Centrifuging twice at 12,000 rcf for 12 min each; **(I)** Storing AgNCs at 4 ºC.

3.2.2. Characterization

First, the UV-Vis spectra of the AgNCs were taken using (BioSpectrometer®, Eppendorf) to determine the plasmonic resonances. A cuvette of 10 mm was used with a 70 µL of purified water as the blank solution, and then measurements were taken with 2 µL of AgNCs and 68 µL of purified water. The spectra were measured between wavelengths of 230 nm and 830 nm.

TEM images were captured for the AgNCs using (FEI Tecnai 12, Tecnai) operating at 120 kV. The samples for the TEM were prepared by dropping 5 µL of the AgNCs solution onto a carbon-coated copper TEM grid. After that, the size and monodispersity of the AgNCs were analysed using ImageJ Fiji and Origin Pro®, respectively.

3.3. Plasmonic Surfaces

3.3.1. Preparation of Substrates

Silicon wafers prime grade (diameter = 100 mm ± 0.5 mm; thickness = 525 µm ± 25 µm) from (PI-KEM Limited, UK) were used as the substrates. The wafers were coated with Ti and Au thin films using an EBE (Evaporator MASA, Micronova, Finland) under a high voltage of 10 kV. A 5 nm layer of Ti was coated first using an emission current of ~ 35 mA and an evaporation rate of ~ 0.2 Å/s. Then, an Au layer with a 50 nm thickness was deposited using an emission current of ~ 37 mA and an evaporation rate of ~ 1 Å/s. Before the deposition process, the EBE was pumped for at least an hour to reach a high vacuum. Once the wafers were fully deposited, a dicing saw (DAD3220, Disco, Japan) was used to cut the wafer into 25×25 mm substrates.

3.3.2. Layer-By-Layer Deposition

For preliminary studies, a well-established system utilizing the LBL disposition technique with PEs compromising poly(allylamine hydrochloride) (PAH) and Poly(sodium 4-styrene sulfonate) (PSS) was investigated. Such a system has been

widely used in literature, for example, to build near-perfect absorbers [22], [23], [69], [110], [111].

To prepare the (PAH) solution, 23.2 g of sodium chloride (NaCl, Sigma-Aldrich, > 99.5%, MW~ 58.44 g/mol) was mixed with 400 mL of purified water. Then, 300 mg of PAH (Sigma-Aldrich, MW~ 17,500 g/mol) was added to the solution. The other solution used contained (PSS) and was prepared in two steps. First, 0.9 g of PSS in powder form was mixed with 5 mL of purified water. Second, 1.2 mL of the PSS prepared solution was added to a solution of 400 mL of purified water and 23.2 g of NaCl. Additionally, a solution of 23.2 g sodium chloride in 400 mL of purified water was prepared.

Before starting the dip-coating process, the substrates were first plasma cleaned with O_2 (75%) and H_2 (25%) for 2 min using (NanoClean Model 1070, Fischione Instruments). The dip-coating procedure varied depending on the desired number of layers. Three 50 mL tubes were filled with 20 mL of one of the three prepared solutions (i.e, NaCl, PAH and PSS). The dip-coating of both the PAH and PSS solutions was assumed to give a thin film with a thickness of 1 nm per deposition [23]. Different substrates were prepared with various odd numbers of layers from one to seven. Figure 3.2 shows a step-by-step procedure for the preparation of layers.

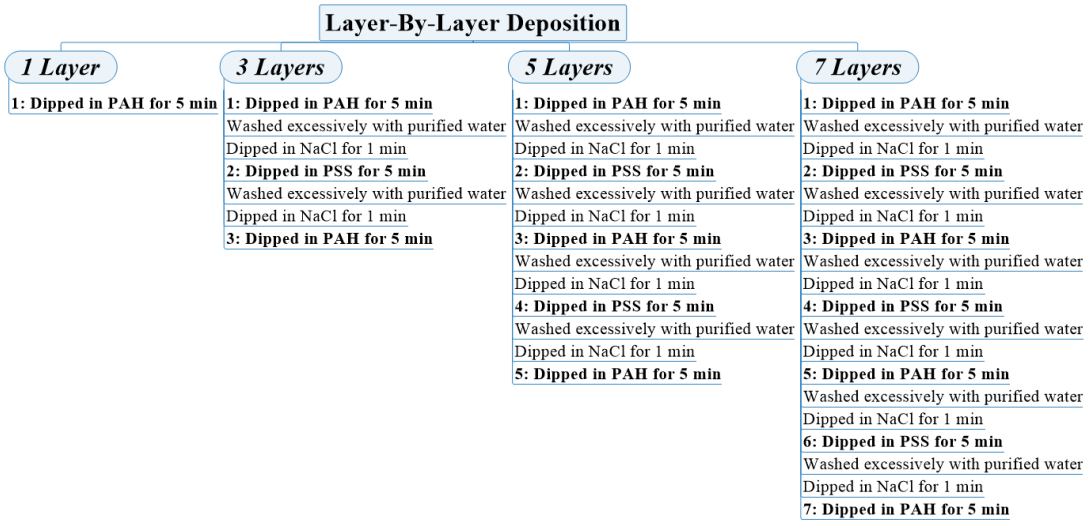

Figure 3.2. A step-by-step procedure used for deposition on substrates with different number of layers of PAH and PSS.

After that, the substrates were rinsed excessively with purified water and dried with nitrogen gas. Then, 200 µL of AgNCs was deposited on each substrate, and the substrates were covered by a microscope cover glass (24×24 mm; thickness ≈ 0.15 ± 0.02 mm) for an hour. Finally, purified water was used to wash the samples in steps (e.g., 5 mL with 1 mL at a time) followed by drying with nitrogen gas. After AgNCs deposition, the samples were stored in a desiccator. Schematics of samples with various layers as well as a 3D illustration of a substate with AgNCs are shown in Figure 3.3.

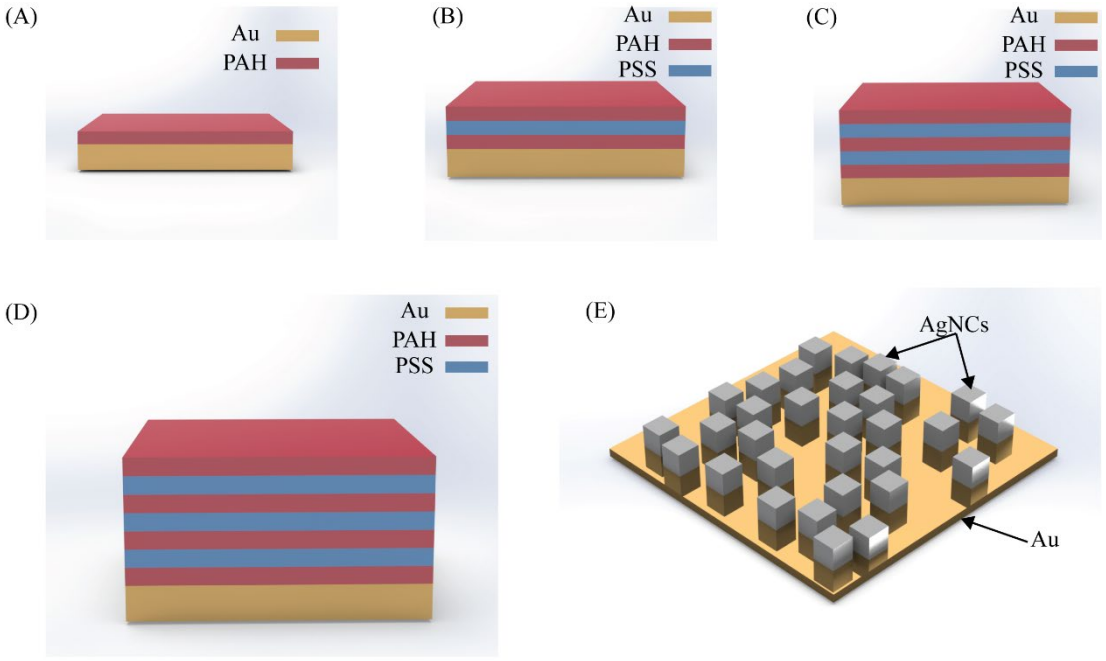

Figure 3.3. Schematic of samples deposited with: **(A)** 1 layer; **(B)** 3 layers; **(C)** 5 layers; and **(D)** 7 layers of PEs using the LBL technique. **(E)** A 3D illustration of a sample after deposition of AgNCs on an Au substrate with layers of PEs.

3.3.3. Deposition of Disperse Red 1

Samples deposited with disperse red 1 (DR1) as the photoactive molecule were prepared in a similar way to the LBL deposition method. However, the samples with DR1 only utilized PAH (i.e., PSS was not used). The PAH solution, as well as the NaCl solution used here, were prepared the same way as in the previous section. The DR1 solution was prepared by dissolving 1% w/v of DR1-glass (SOL80485, >99%,

Solaris Chem), shown in Figure 3.4, in a dimethylformamide (N,N-DMF, ≥ 99.8%, Acros Organics, MW ~ 73.09 g/mol) solution (e.g., 1 mg of DR1 in 100 µL of DMF).

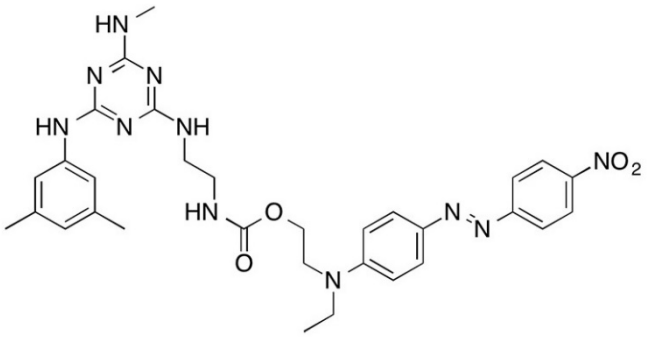

Figure 3.4. Chemical structure of the used DR1-glass, adapted with permission from [155]. Copyright © (2016) Elsevier.

Before starting the deposition process, the substrates were plasma cleaned using the earlier mentioned procedure. The substrates were spin-coated with 80 µL of the DR1 solution at 5,000 rpm for 45 seconds using a spin coater (WS-650-SX-6NPP/LITE, Laurell Technologies) to obtain 2 to 8 nm thick films. Then, the substrates with DR1 films were baked at 60 ºC for 30 min in an oven (Heratherm™ General Protocol Oven, Thermo Fisher Scientific).

After baking, the substrates with DR1 were dip-coated with PAH and deposited with AgNCs. First, the substrates were dipped in a 50 mL tube filled with 20 mL of the NaCl solution for a minute. Second, they were dipped in a 50 mL tube filled with 20 mL of the PAH solution for 5 min to obtain 1 nm thick film [23]. After that, the substrates were washed excessively with purified water and dried with nitrogen gas. Later, 200 µL of AgNCs was drop cast on the substrates, and then the substrates were covered using a microscope cover glass (24×24 mm; thickness ≈ 0.15 ± 0.02 mm) for an hour. Finally, purified water was used to wash the samples in steps (e.g., 5 mL with 1 mL at a time) followed by drying with nitrogen gas. The samples were stored in a dry and dark environment. Figure 3.5 shows schematics of the spin coating process as well as the layers of the prepared samples and a 3D illustration of the substrate with AgNCs.

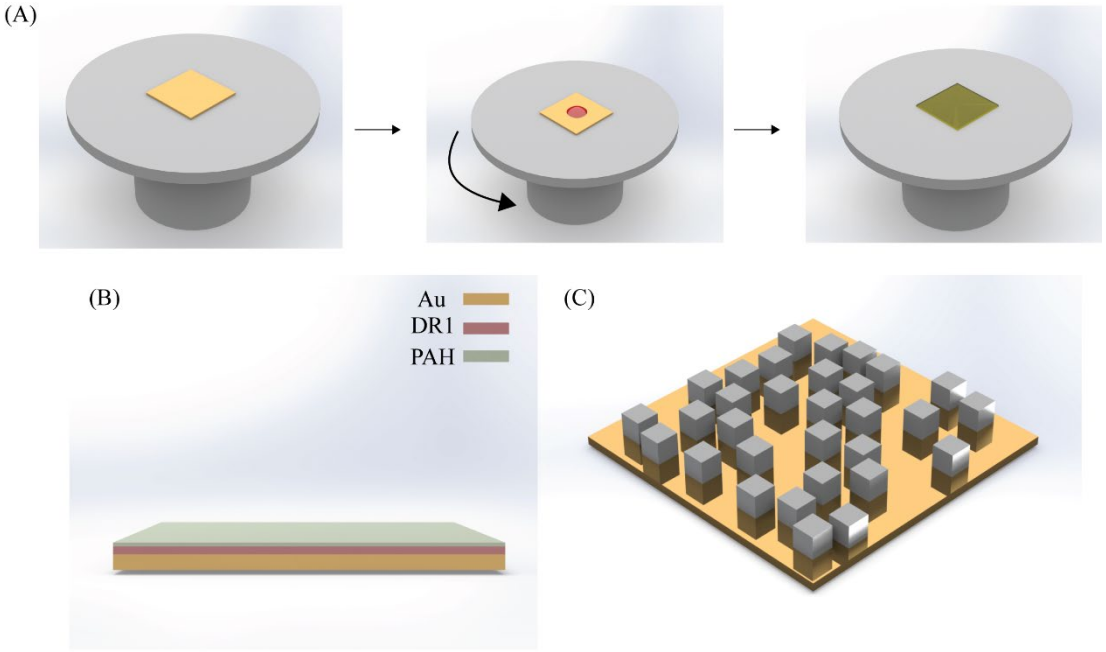

Figure 3.5. (A) Different steps of the spin coating process of DR1 on am Au substrate at 5,000 rpm for 45 seconds (Initial → after drop casting → after spin coating); **(B)** A substrate with a DR1 layer and a PAH layer before deposition of AgNCs; and **(C)** A 3D illustration of an Au substrates with a spacer layer of PAH and DR1 after AgNCs deposition.

3.3.4. Characterization

Surfaces of the samples were imaged using SEM (Sigma VP, Zeiss). The images were taken under high vacuum (i.e., $< 10^{-5}$ Pa) using an In-lens detector, acceleration voltage of 7 kV and a working distance (WD) between 5 and 9 mm.

The reflection and transmission spectra of the samples were measured using (V-770 UV-VIS/NIR Spectrophotometer, JASCO) equipped with a reflection accessory unit (ARSN-917, JASCO). Spectra Manager™ software was utilized to acquire the data. All the measurements were taken in a wavelength range between 250 and 2000 nm with a normal incidence angle of 6^{o} and a white plate standard as the baseline spectrum. Further details of the specifications used for the measurements can be found in Table 3.1.

Table 3.1. Different specifications used for spectra measurements with the reflection accessory unit.

Specification	**Description**
Wavelength range	250 to 2000 nm
Angle of incidence	Absolute reflectance: 6º Transmittance: 6º
Sample size	25×25 mm
Detectors	Photomultiplier tube PbS photoconductive cell
Inner surface of integrating sphere	Barium sulphate
Bandwidth	UV: 5 nm NIR: 20 nm
Absolute reflectance accuracy	±1.5% (angle of incidence 6º)
100% line flatness	±1% (bandwidth: UV 5 nm and NIR 20 nm)
Response rate	0.24 sec
Scan speed	1000 nm/min
Data interval	2 nm

The absorbance (*Abs*) [%] can then be calculated as suggested in the literature [111] as follows:

$$Abs = 100\% - (R + T) \tag{3.1}$$

where, R [%] is the reflectance and T [%] is the transmittance.

The quality factor for the fundamental mode was calculated based on the equation from Rozin *et al.* [111] as follows:

$$Q = \frac{\lambda_r}{FWHM} \tag{3.2}$$

where, λ_r [nm] is the resonance wavelength and *FWHM* [nm] is the full width at half maximum. The values of the *FWHM* were measured by the Spectra Manager™ software.

The refractive index (n) and the extinction coefficient (k) of the samples were estimated using the built-in UV-Vis K-K Conversion program in the Spectra Manager™ software. The programme utilizes Kramers-Kronig (K-K) conversion to calculate the phase change (Φ), and then estimate the complex refractive index (i.e., n and k) based on the reflectance and phase change as follows:

$$n = \frac{1}{1 + R - 2\sqrt{R}\cos\Phi} \tag{3.3}$$

An Au substrate with a thickness of ~ 50 nm was used to determine the suitable transparent region of the samples needed by the programme. Iterations were performed and a region between 350 to 475 nm produced the best results for similar reported data in the literature. The same parameters were then used to estimate the refractive index values for the DR1 samples.

Additionally, the sensitivity (*S*) and the figure of merit (*FOM*) of the DR1 samples before and after exposure to polarized light were calculated based on [20], [112]-[117] at the resonant wavelengths as follows:

$$S = \frac{\Delta\lambda_r}{\Delta n} \tag{3.4}$$

$$FOM = \frac{S}{FWHM} \tag{3.5}$$

However, it should be noted that for calculating the sensitivity, the reference used here was the substrate before light exposure (i.e., at 0 min) and not air. The sensitivity was calculated in nanometre per refractive index unit [nm/RIU].

3.3.5. Light Exposure Measurements

Samples prepared with DR1 were exposed to a mounted light-emitting diode (LED) (M490L4, Thorlabs). Key specifications of the LED used are provided in Table 3.2. The LED was used along with a LED driver (LEDD1B T-Cube, Thorlabs) and an adjustable collimation adapter (SM1U25-A, Thorlabs). Samples were exposed to either one or two types of polarized light for varying durations of time from 1 to 60 min. The first set of samples were exposed to light with a linear polarizer (XP42-200, Edmund) on a cage rotation mount (CRM1/M, Thorlabs). The second set of samples were irradiated with circularly polarized light using a left-handed circular polarizer (CP1L488, Thorlabs) on a lens mount (LMR1/M, Thorlabs). Finally, samples from each set were exposed to a polarized light using the other polarizer (i.e., Linear → Circular or Circular → Linear). The setups for the patterns of light exposure used in this work are illustrated in Figure 3.6.

Table 3.2. Specifications of the mounted LED used to irradiate DR1 samples.

Specification	Description
Colour	Blue
Peak wavelength	490 ± 10 nm
Output power	240 mW
Distance between LED and sample	30 mm
Forward voltage	3.2 V
Current	350 mA

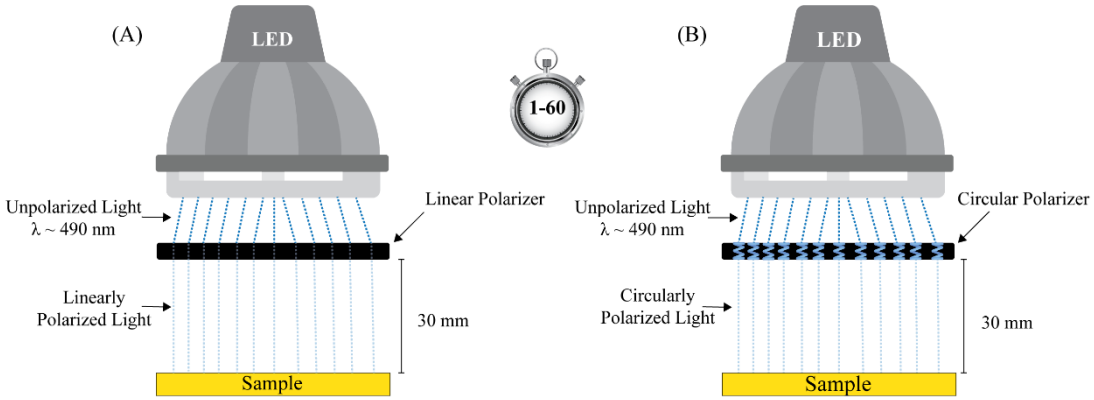

Figure 3.6. Setups for light exposure for DR1 samples using: **(A)** Linear polarizer; and **(B)** Circular polarizer. Samples were exposed for different durations of time from 1 to 60 min.

Chapter 4: Results and Discussion

The evaluation of the proposed active plasmonic surfaces is the main focus of this chapter. Experimental analyses have been conducted as well as estimations for the refractive index. Furthermore, the fabricated plasmonic surfaces were assessed against similar works as applicable. This chapter is divided into three main parts: i) characterization of the synthesized AgNCs; ii) characterization of plasmonic surfaces using the LBL deposition; and iii) characterization of the plasmonic surfaces with DR1.

4.1.Characterization of Sliver Nanocubes

AgNCs play a vital role in the performance of plasmonic surfaces as they support surface plasmon (SP) and exhibit relatively low ohmic losses and large bandwidth [22], [23], [110], [111]. As a result, it can be stated that the synthesis process of AgNCs must be performed with ultimate care to minimize the influence of unwanted effects. For optimizing the synthesized AgNCs, it is important to understand the different stages of their growth that are shown in Figure 4.1. To begin, ethylene glycol (EG) is used to form highly volatile nuclei by reducing Ag^{+} ions. After that, the formed nuclei start to grow and have a more defined structure as fluctuations stop. Then, the structures of Ag^{+} ions take one of three main forms: i) single crystalline free from boundary defects; ii) single twinned boundary defects; or iii) multiply twinned boundary defects. Finally, the newly formed silver structures grow further to form

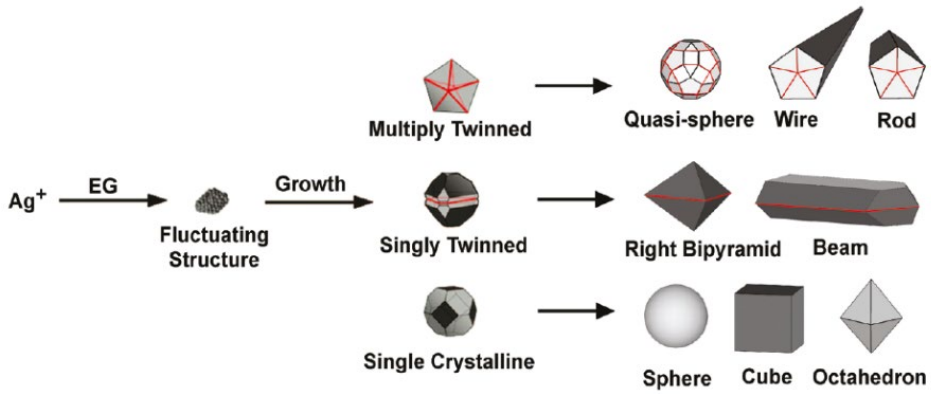

Figure 4.1. Synthesis of Ag nanostructures by a polyol method with ethylene glycol (EG), adapted with permission from [42]. Copyright © (2011) American Chemical Society.

nanostructures with desired morphology based on the treatment and path taken during the synthesis.

Based on the synthesis processes conducted during this work and those found in the literature [51], [118]-[122], some remarks can be given. First, the edge length of AgNCs increases as the reaction time increases. Second, EG cannot be used to obtain AgNCs with an edge length below 30 nm as the reaction is fast in the first 15 min. Third, a mole ratio of about 2:1 (PVP:CF_3COOAg) at a temperature near 150 ºC was found to be optimal for obtaining AgNCs with the least irregularities. Additionally, the concentration of HCl was found to be more important than that of NaHS for the overall quality of the formed AgNCs. As the concentration of HCl increases, the size of AgNCs increases and other AgNPs structures are observed. Moreover, the formation of single-crystal seeds is mainly governed by NaHS, while HCl helps to significantly reduce twinned AgNCs by acting as a ligand (i.e., due to Cl^- ions) for oxidative etching. Finally, PVP, which is a negatively charged polymer, is used to facilitate the adhesion of NCs on the positively charged polyelectrolyte (i.e., PAH) as well as to form a protective layer against oxidation of silver [22], [23], [69], [110], [111].

The synthesized AgNCs are shown in Figure 4.2. It can be noticed that the particles are, in general, highly monodisperse as shown in Figure 4.2A. The AgNCs have an average size of ~ 66 ± 8 nm as presented in Figure 4.2B. The UV/Vis spectra shown in Figure 4.2C is useful to identify the size during the synthesis process. The sharpness of the LSPR peak (i.e., at ~ 464 nm) helps in assessing the monodispersity, while the wavelength can be used to estimate the average edge length of AgNCs. For example, Zhang *et al.* [118] proposed a formula with an accuracy of (R^2 = 0.99). The average edge length of AgNCs synthesized here were estimated to be around 62 nm using their proposed formula. This is close to the measured value (i.e., 66 nm) and falls within the margin (i.e., ± 8 nm). Their equation for the calibration curve using the LSPR peak position (λ_{LSPR}) and the average edge length of AgNCs (l) is as follows:

$$\lambda_{LSPR} = 1.3927 \times l + 378.25 \tag{4.1}$$

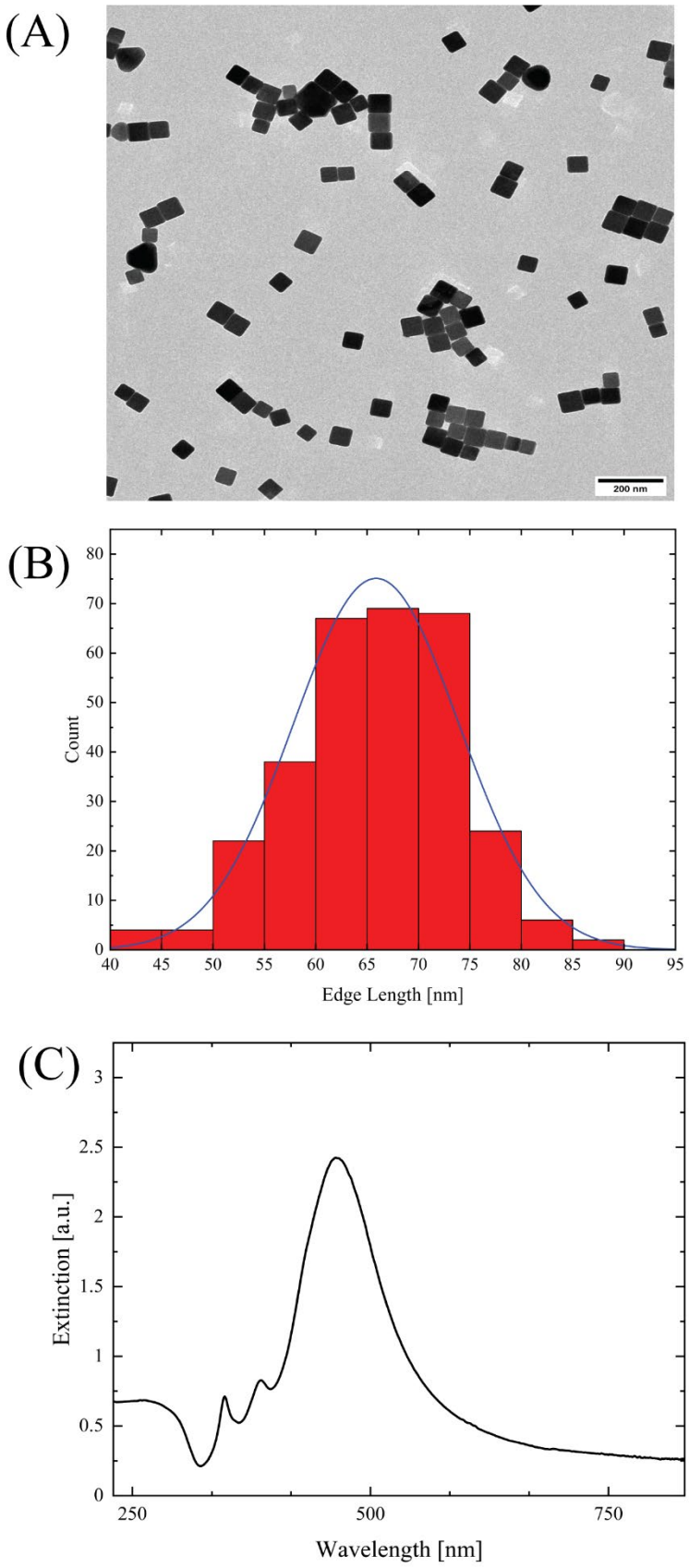

Figure 4.2. Synthesized AgNCs: **(A)** TEM image; **(B)** Edge length with normal distribution; and **(C)** UV/Vis spectra.

The size of the AgNCs was selected based on the reported data in the literature to enhance the sharpness of the absorbance peak at the resonant wavelength (λ_r). For larger NCs, the absorption efficiency of λ_r decreases due to a larger scattering cross-section [123]. It has been also reported that AgNCs with sizes between 70 and 96 nm yielded the lowest reflectance values at the fundamental mode [22], [23], [69], [110], [111]. Normally, NPs with a range size between 70 and 96 nm are considered large for many plasmonic applications. However, it is needed here as large colloidal NPs allow shifting the plasmonic resonance to the infrared region of the spectrum. For colloidal AgNCs, the edge length should not exceed 140 nm, since AgNPs larger than that become less cubic and form extra facets [23]. The average size of the synthesized AgNCs here is slightly smaller than what is suggested, but it showed sufficiently close results to experiments reported in [22], [23], [69], [110], [111]. It should be emphasized that the AgNCs can be optimized further in terms of size and shape to achieve better results, but this is currently out of the scope of this work.

4.2. Characterization of Layer-By-Layer Plasmonic Surfaces

As indicated in the previous chapter the plasmonic surfaces comprising AgNCs, metal gold film with and polyelectrolytes (PEs) spacer layer have been extensively investigated. The studies performed here were used to guide the development of experimental protocols to be utilized for the fabrication of the active plasmonic surfaces with disperse red 1 (DR1). Our results with different number of layers, in general, are consistent with the existing literature [22], [23], [69], [110], [111]. The main findings are presented in this section.

4.2.1. Optical Characteristics

The SEM images in Figure 4.3 show that the distribution of AgNCs after surface deposition is highly uniform. Additionally, samples with one layer of PAH were also prepared with AgNCs of sizes ranging from 54 to 62 nm. It was noted that an increase in the size of AgNCs leads to a redshift in the resonant wavelength as can be seen in Figure 4.4 This is attributed to the rise of the dipolar resonance wavelength for non-coupling NCs [111]. It was also observed that as the size of the AgNCs increases, the

repeatability generally decreases in terms of obtaining the same fundamental resonance values.

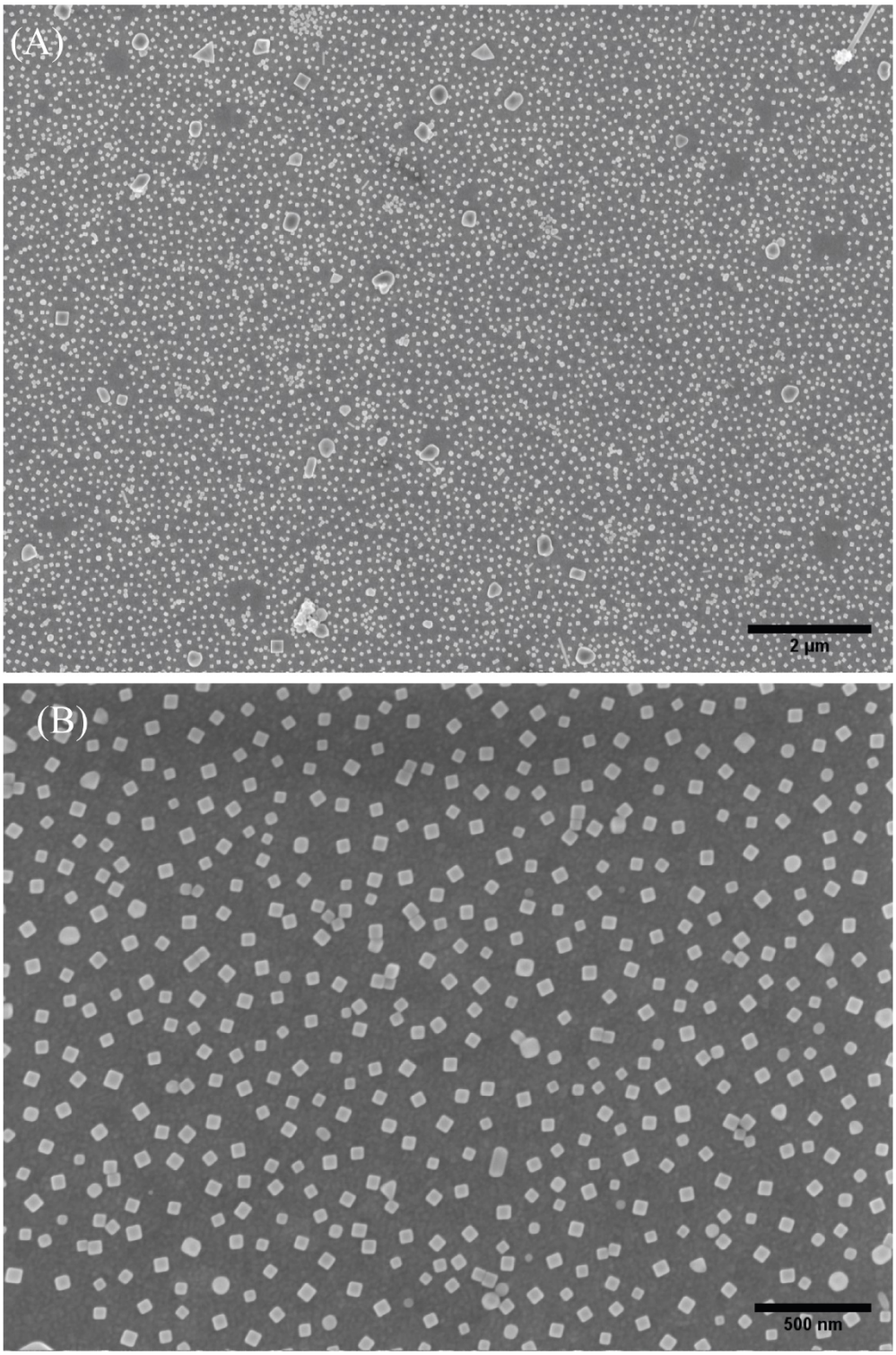

Figure 4.3. SEM images of the surface of a sample of the system of layers with 5 layers of PEs under magnifications of: **(A)** 7.88 kX ; and **(B)** 28.91 kX. Both images were taken at WD ~ 8.3 mm.

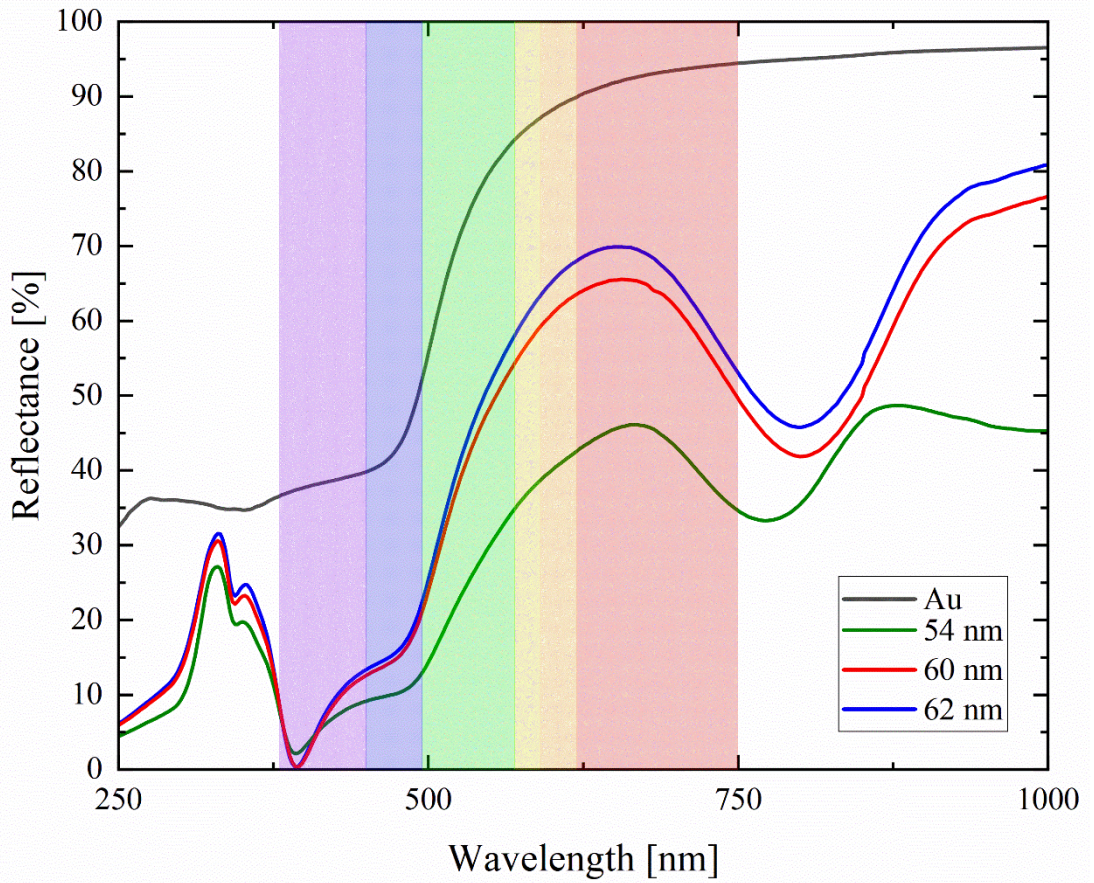

Figure 4.4. Effect of AgNCs size on the resonant wavelength of the plasmonic surfaces. The plasmonic surfaces with larger size of AgNCs exhibit sharper peaks of absorbance at the resonant wavelength. The spectra shown are for one layer of PEs (i.e., PAH).

The oxidation of AgNCs is a critical limitation to their practicality. Here, the oxidation of the AgNCs of the plasmonic surfaces was estimated by measuring the reflectance spectra of the samples. Figure 4.5 shows the reflectance spectra of a sample with 3 layers of spacer stored in a desiccator for 13 weeks. The reflectance spectra show a redshift and an increase in the reflection intensity with time due to oxidization. After full oxidization, the spectra would become similar to that of gold [22]. The samples prepared in this work showed relatively low oxidization as the protection layer of PVP was maintained by avoiding using acetone in the fabrication process of the plasmonic surfaces [22].

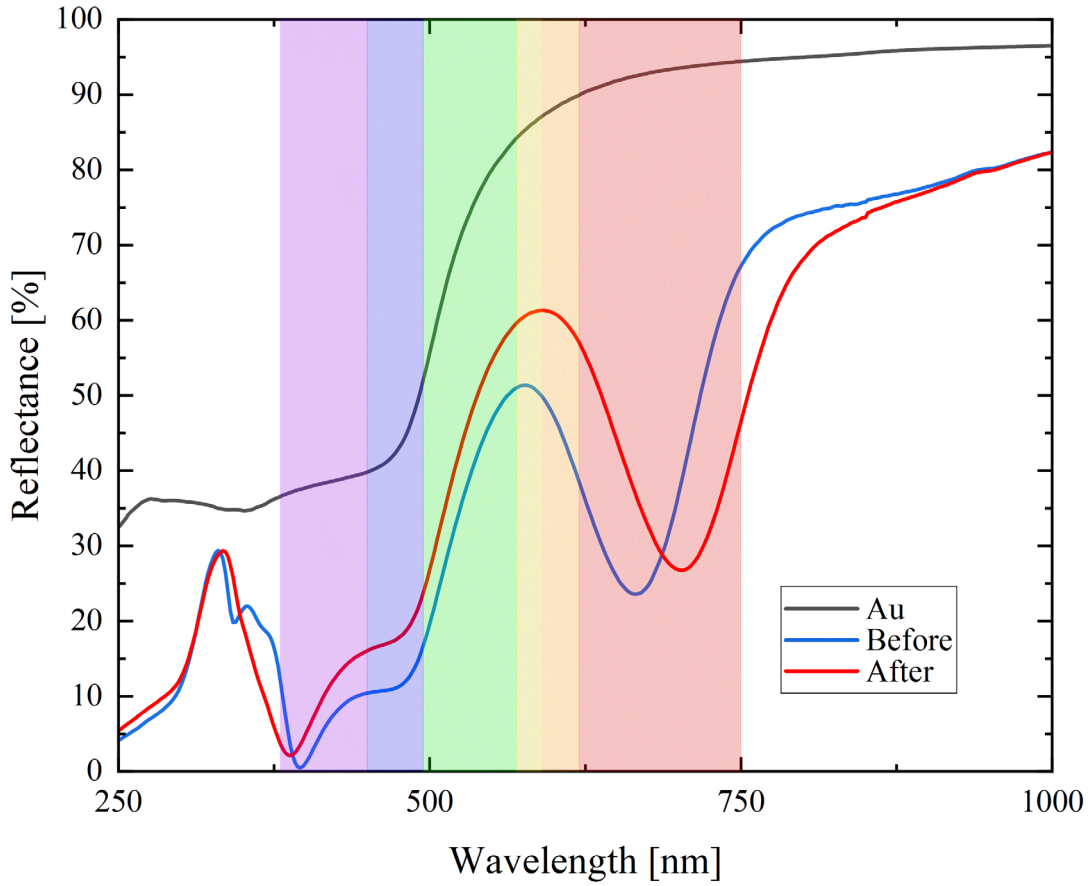

Figure 4.5. Effect of AgNCs oxidization on a sample with 3 layers of a spacer. The absorbance peak at the resonant wavelength redshifts and the intensity of the reflection increases after being stored for 13 weeks in a desiccator.

4.2.2. Colour Modulation

Colour modulation using the LBL deposition has been implemented in earlier works, which was achieved mainly by varying the number of layers of the spacer [22]. In this work, samples of up to 7 layers were prepared, and their spectra are shown in Figure 4.6. The transmittance values of the samples were confirmed to be negligible (i.e., < 0.2%) using the UV-Vis spectrophotometer due to their opaque nature. Thus, the absorption of the samples was calculated using equation (3.1) where the transmittance (T) was assumed to be zero. As the number of layers increases, the resonant wavelength blueshifts and the absorbance becomes stronger. This trend was also observed by Akselrod *et al.* [23] in their work in 2015. The blueshift of the

reflectance spectra is attributed to the decrease of the electromagnetic coupling between the nanocubes and the metal Au film [111], [124].

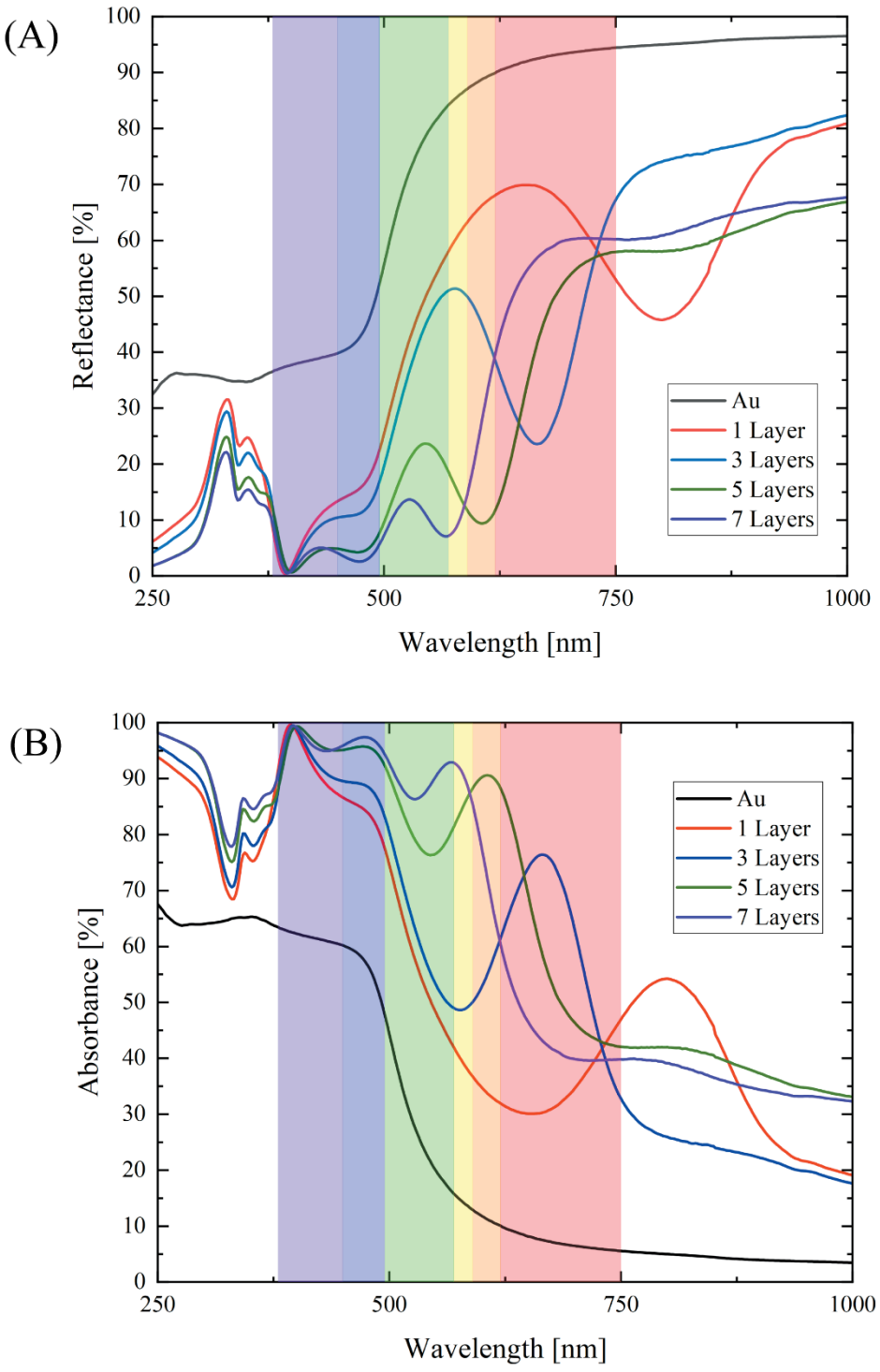

Figure 4.6. Spectra of plasmonic surfaces deposited using LBL technique: **(A)** Reflection spectra; and **(B)** Absorption spectra. The resonant wavelength blueshifts and absorbance peak becomes stronger and sharper as the number of layers increases.

The chromaticity diagram is used to represent the vibrancy of colours with the CIE 1931 diagram being the most commonly used [9], [125]. Colours represented by at least two primary colours are known as secondary colours and every subset spanned of secondary colours is called a gamut. A common gamut is the standard gamut (sRGB) represented by red, green and blue as the primary colours. The borders of the diagram are where the colours with the highest vividity are located, and a wider coverage range on the diagram indicates better chromaticity.

The colours produced corresponding to a different number of layers are shown in Figure 4.7A and their distribution on the CIE 1931 diagram is represented in Figure 4.7B. It can be seen from Figure 4.7B that the colours produced with the samples in this work have moderate to low chromaticity and cover a region limited to the right-hand side of the diagram.

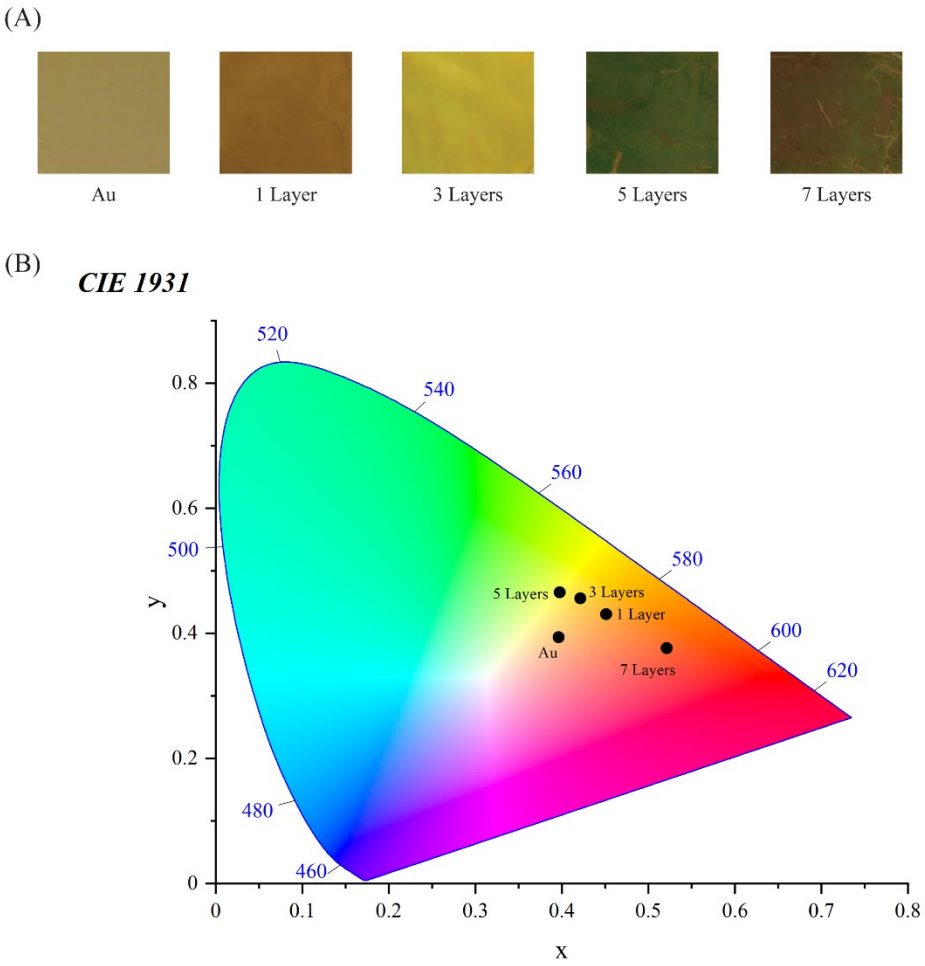

Figure 4.7. (A) Colours produced using samples LBL coated with different numbers of PE layers; and **(B)** The colour distribution of the samples on the CIE 1931 diagram.

Values of important parameters at the resonant wavelength of samples with a different number of layers are found in Table 4.1. It can be noted that with the increase of the number of layers, the quality factor increases significantly due to a decrease in the full width half maximum (*FWHM*) of the absorbance peak. These findings align with previous reports [23]. The observed reduction in *FWHM* here is due to the change in the interactions between the NCs with one another (In-plane interactions) as well as the interactions between the NCs with the gold film (Out-of-plane interactions). As the spacer height increases, the in-plane interactions become stronger, while the out-of-plane interactions get weaker [111]. Thus, the electromagnetic coupling between the nanocubes and the metal Au film becomes weaker [111], [124]. Moreover, samples with 7 layers can be further optimized to produce near-perfect absorbers.

Table 4.1. Summary of optical parameters of plasmonic surfaces coated with a different number of layers using the LBL deposition technique.

Number of Layers	λ_r **[nm]**	**%*R*** (λ_r)	**%*Abs*** (λ_r)	***FWHM*** **[nm]**	***Q***
1	800	45.81	54.19	127	6.3
3	666	23.59	76.41	79	8.4
5	606	9.39	90.61	56	10.8
7	566	7.07	92.93	34	16.7

Multilayer films of PAH/PSS are known to exhibit more swelling with the increase in the humidity [126]-[128]. Both the swelling and deswelling are reversible as well as reproducible. Wong *et al.* [129] reported that at a high level of humidity (i.e., > 99%), the swollen thickness becomes highly dependent on the type of PE on the outermost layer. Thus, the swelling of the PEs starts to show an “odd-even effect”. Multilayer films with an even number of layers of PAH/PSS (i.e., PSS in the outermost layer) shows a higher degree of swelling than those with an odd number of layers (i.e., PAH in the outermost layer). This is attributed to the ability of PSS to attracts more water per volume than PAH [130].

Hence, a change in the colour of the samples with humidity was observed as shown in Figure 4.8. The change in humidity on the surface of the samples by, for example,

temperature variation (i.e., cooling and heating) causes a change in the thickness of the PE layers [131], which results in a change in the nanocavity resonance [23]. Specifically, a temperature increase leads to a decrease in relative humidity. The decrease in humidity results in a reduction in the thickness of the spacer layers, which in turn increases the refractive index [132]. This variation in the thickness (i.e., refractive index) is associated with a change of the plasmon resonance. An increase in the refractive index causes a redshift of the resonant wavelength. In contrast, a decline in the refractive index, with the decrease of the humidity, results in a blueshift. Consequently, the shift in the plasmon resonance leads to dynamic colour tuning [131].

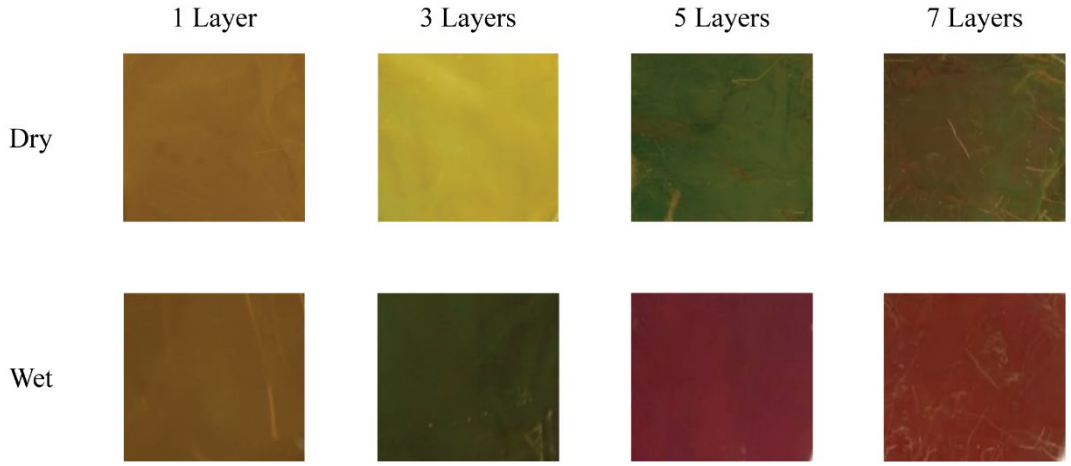

Figure 4.8. Colour change with relative humidity of samples LBL coated with various layers from 1 to 7. The increase in the relative humidity causes the resonant wavelength to redshift.

Furthermore, this work also investigated the effect of changing the concentration of both PEs used (i.e., PAH and PSS) as well as their dip-coating time on the swelling of the PE layers (i.e., change in thickness). Initially, the concentration of the PAH solution was increased by 10 and 100 times, while the concentration of the PSS solution as well as the dip-coating time were kept constant. Figure 4.9A shows that the reflection intensity decreases dramatically with the increase of the PAH concentration. This can be attributed to the increase of the charge of the PAH layers, which in turn leads to more binding between the AgNCs and the outermost PAH layer. Consequently, the absorbance at the resonance wavelength increases due to the decrease in the interparticle distance between the AgNCs [111]. Thus, the change in

colours due to the swelling of the PE layers become unnoticeable because of the high absorbance as illustrated in Figure 4.9B.

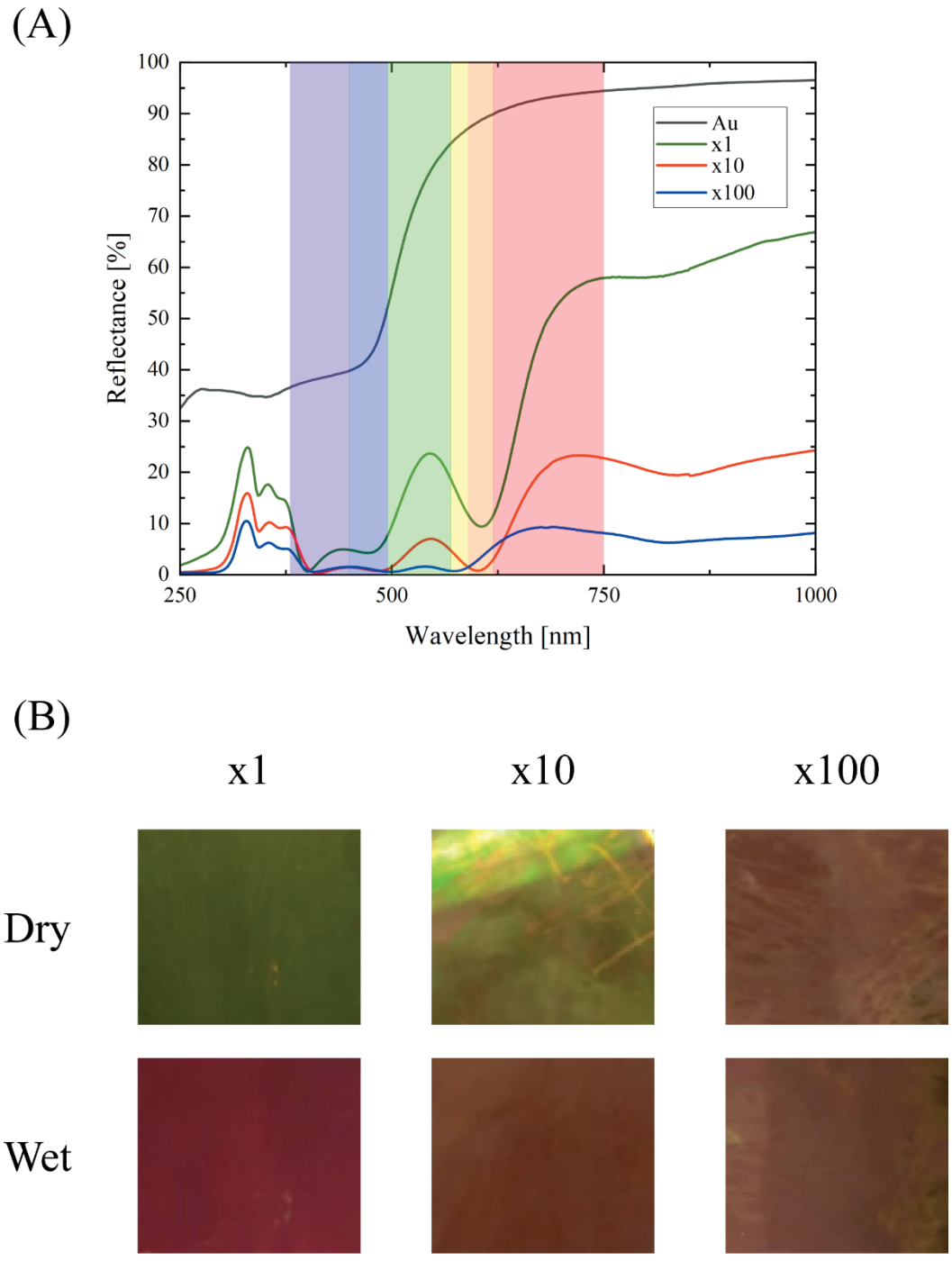

Figure 4.9. (A) Reflectance spectra of 5 layers samples with varying PAH concentration. Dip-coated samples in higher concentration PAH solutions show more binding of AgNCs on the surface. Both the concentration of PSS solution and the dip-coating time were kept constant. **(B)** Swelling of the outermost PE layer with different concentrations of PAH.

Both Figure 4.10A and Figure 4.10B show that increasing either the concentration of PSS or the dip-coating time does not lead to a significant change in the resonant wavelength. This observation further highlights the importance of the binding between the outermost layer of the spacer and the AgNCs.

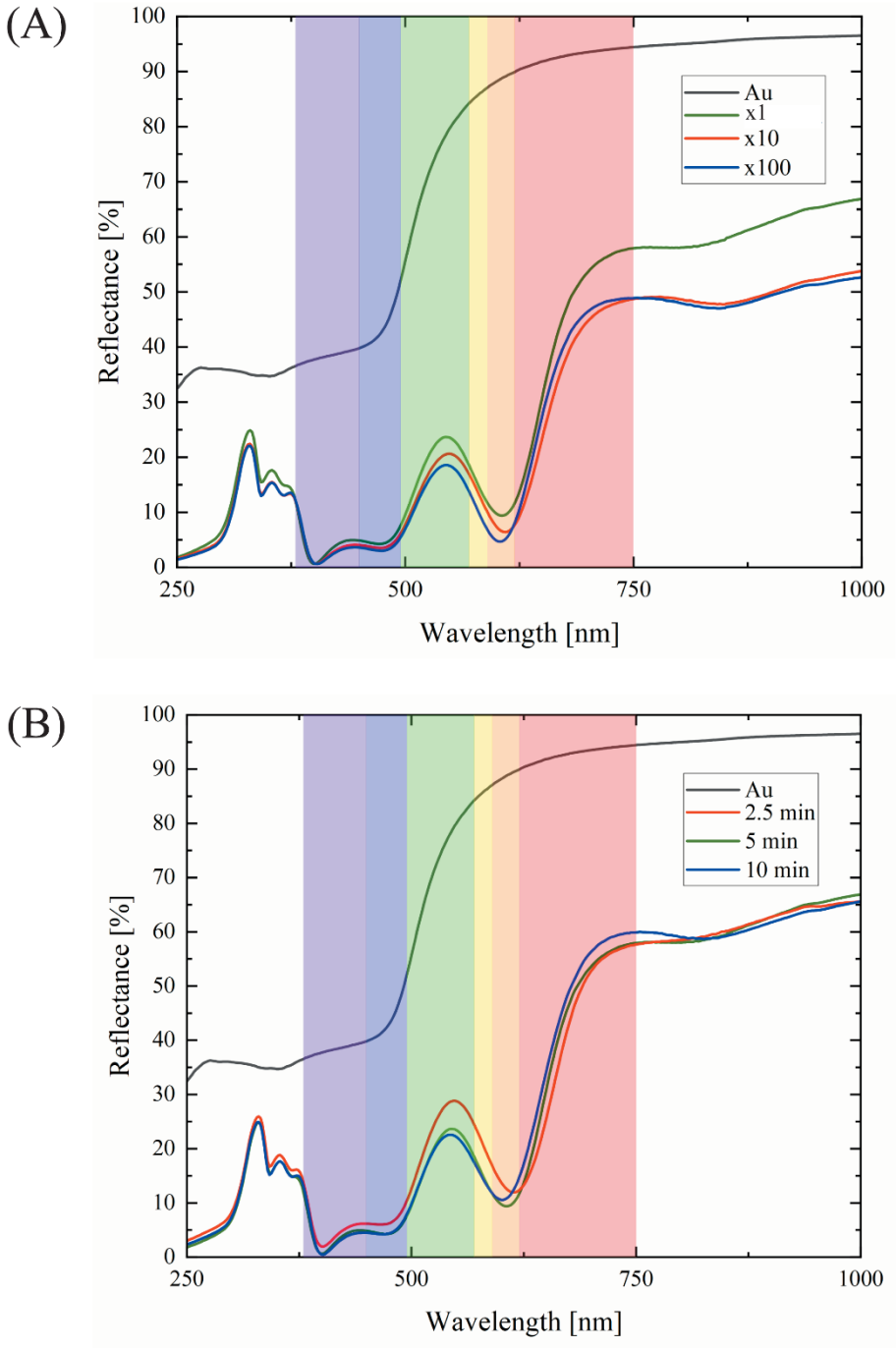

Figure 4.10. (A) Reflectance spectra of 5 layers samples with varying PSS concentration. Both the concentration of PAH solution and the dip-coating time were kept constant. **(B)** Reflectance spectra of 5 layers samples with varying time durations of dip-coating. The concentration of both the PAH and PSS solutions was kept constant. Changing either the concentration of the PSS solution or the duration of dip-coating has no significant effect on the reflectance spectra.

4.3.Dynamic Modulation with Disperse Red 1

In the previous section, active plasmonic surfaces using LBL deposition were successfully fabricated. Here, we incorporated a layer of the photoactive molecule DR1 in the LBL deposition system, as shown in Figure 4.11, to dynamically modulate light for the active plasmonic surfaces.

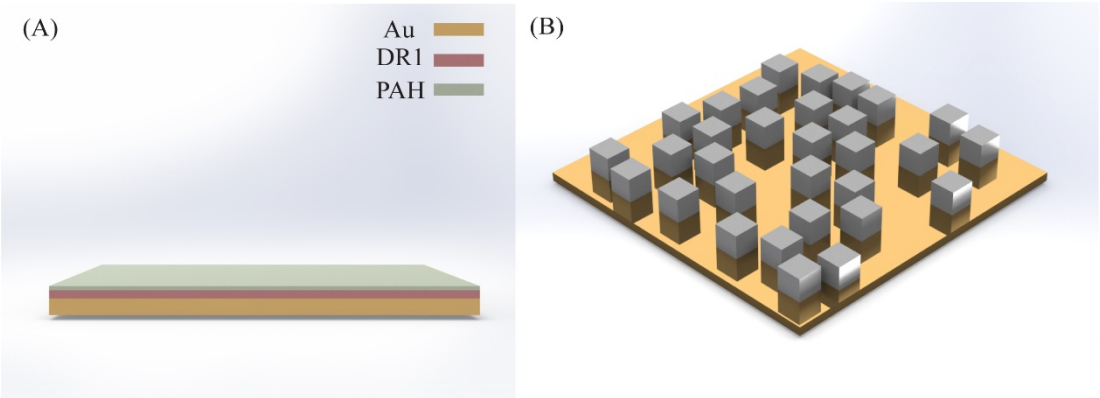

Figure 4.11. (A) A schematic illustrating the different layers of the proposed DR1 system; and **(B)** A 3D illustration of an Au substrates with a spacer layer of PAH and DR1 after AgNCs deposition.

It should be emphasized that DR1 is a highly sensitive molecule towards light. Thus, the samples prepared here were stored in a dark environment to avoid undesired spectral shifts. The experimental tests in this work show that when the samples are kept under ambient light, the spectra redshift significantly with a slight decrease in the absorbance as illustrated in Figure 4.12. The transmittance values for the samples prepared with DR1 were near-zero (i.e., < 0.1%) across the whole measured spectrum, thus they were ignored in this work for simplicity.

The conducted tests with the DR1 samples in this work showed consistent patterns of spectra. However, it was observed that the adhesion of the AgNCs on the surface of the DR1 samples is not consistent, and thus leading to an inconsistency of the intensity of the spectra (i.e., ΔR (λ_r) ~ 37.5%), while the resonant wavelength is almost identical (i.e., λ_r ~ 602 nm) as shown in Figure 4.13. SEM images confirmed that the variation in the intensity is due to the adhesion of AgNCs as illustrated in Figure 4.14. A reason behind that could be that DR1 does not bind well to the Au substrate due to differences in their nature causing a nonuniform coating during the spinning process. Thus, this

can lead to an imbalance of the binding between the Au substrate and the PAH layer, which in turn would impact the adhesion of AgNCs.

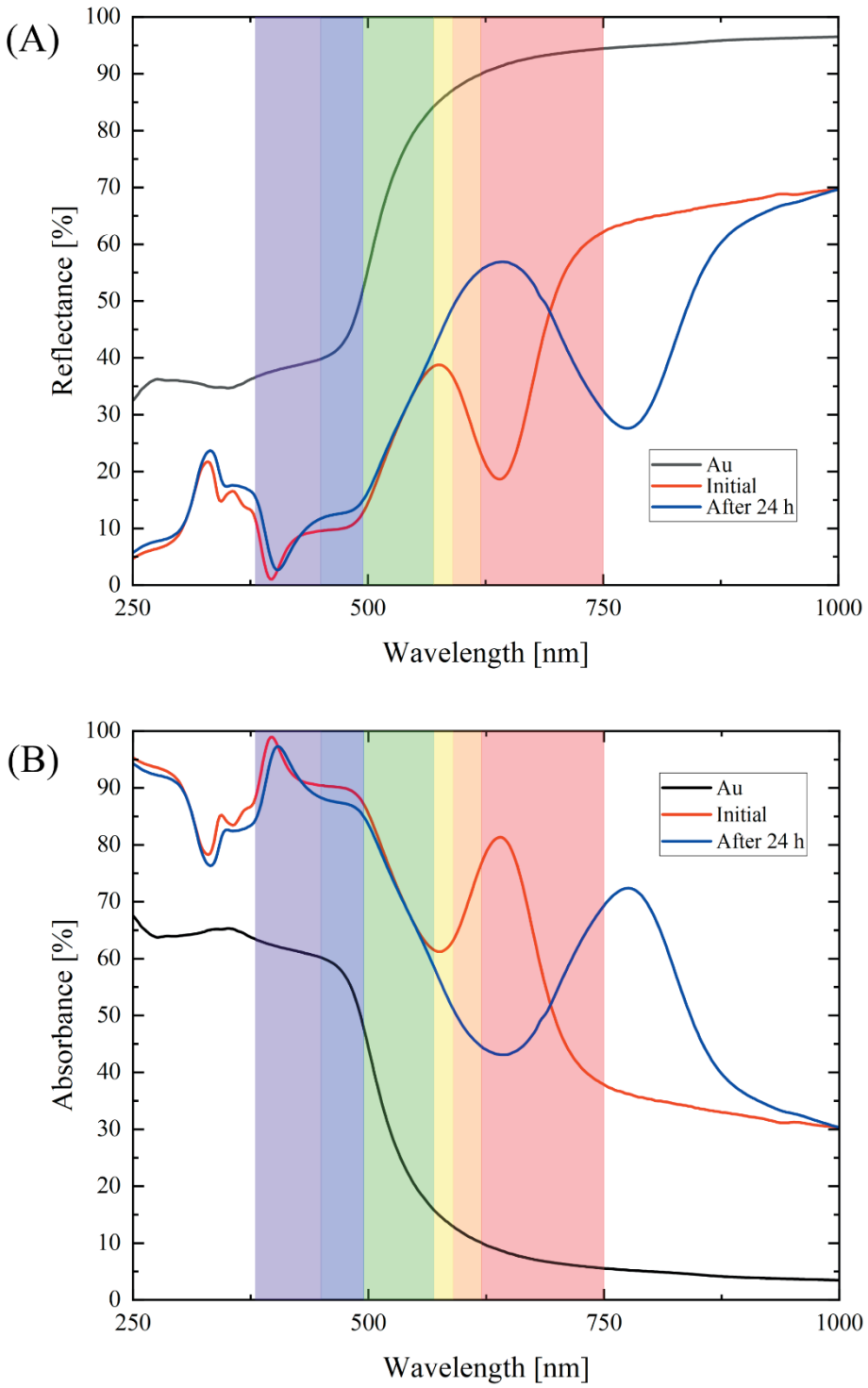

Figure 4.12. Effect of exposure to ambient light for 24 h on DR1 samples: **(A)** Reflectance spectra; and **(B)** Absorbance spectra. The samples redshift significantly and reflection intensity increases with the exposure time to ambient light.

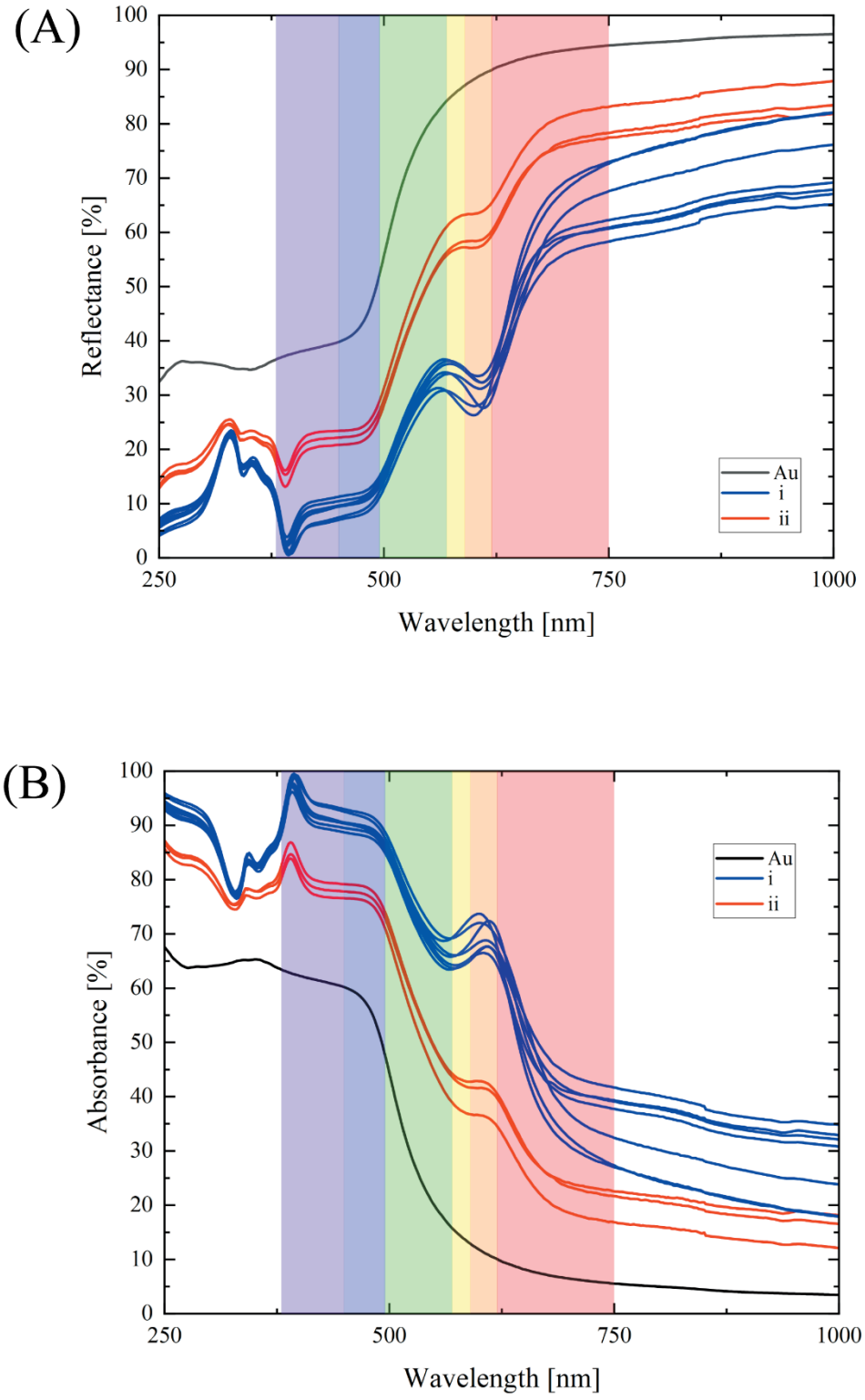

Figure 4.13. Variation in the intensity of ten DR1 samples: **(A)** Reflectance spectra; and **(B)** Absorbance spectra. Spectra (i) represent samples with strong AgNCs adhesion on the surface, while spectra (ii) represent sample with weak AgNCs adhesion.

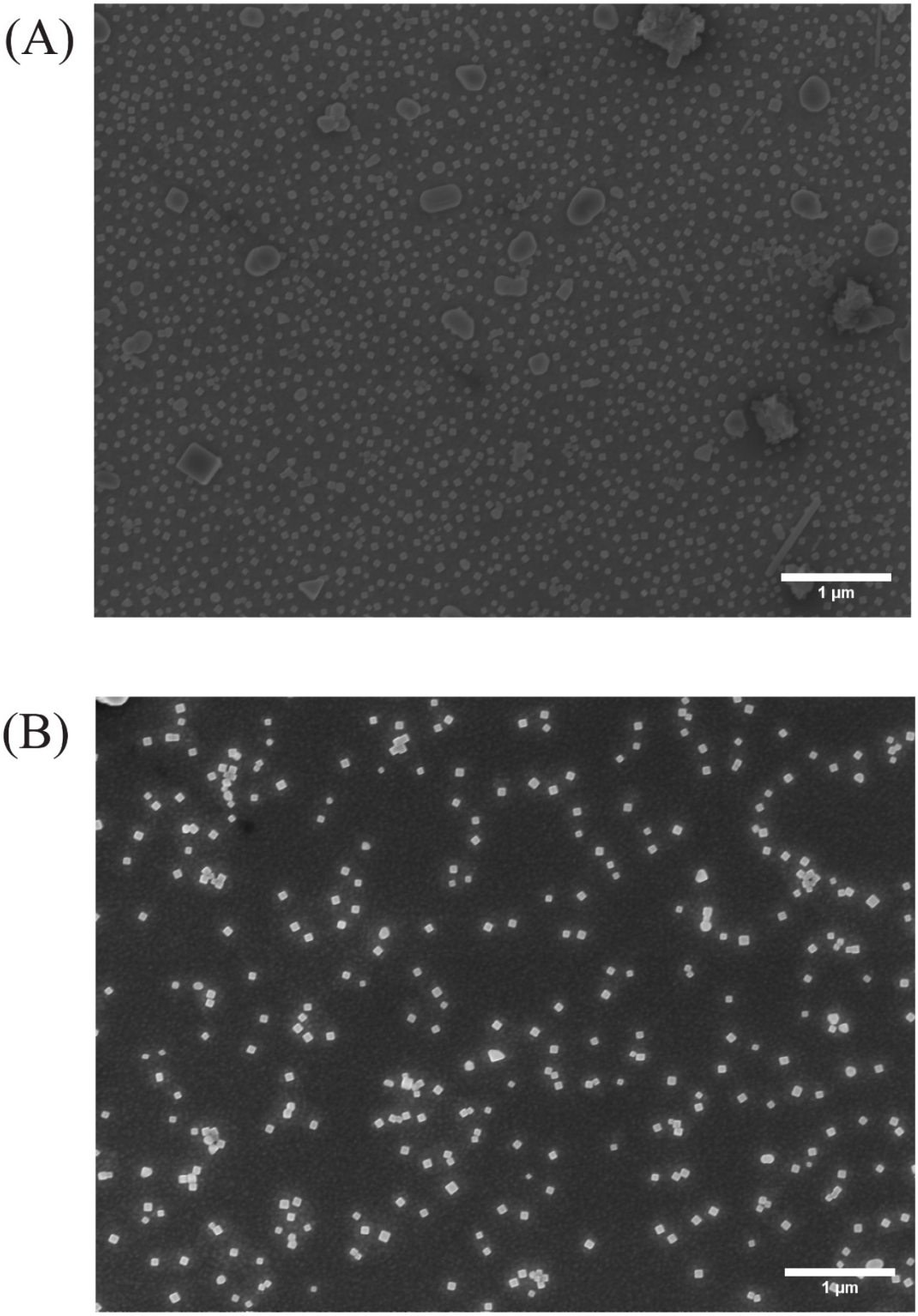

Figure 4.14. Representative SEM images of DR1 samples with: **(A)** Strong AgNCs adhesion to the surface; and **(B)** Weak AgNCs adhesion to the surface. Both images were taken with WD ~ 8.5 mm.

The samples prepared in this work exhibited some variations in the spectra intensity as shown in Figure 4.13. Thus, the results presented from this point forward should not be taken as absolute rather as close estimations since further investigations are needed. The results shown in the following subsections are representative of samples with (i) spectra from Figure 4.13, where AgNCs adhered well on the surface.

4.3.1. Dynamic Colour Modulation

The samples were examined under light exposure with linear and circular polarizers. When the DR1 samples were exposed to either linearly or circularly polarized light, the resonant wavelength redshifted significantly ($\Delta\lambda_r \sim 112$ nm) as the exposure time increases from 1 to 60 min. However, the intensity of the spectra only changed slightly ($\Delta R \sim 2\%$) with the increase of the irradiation time as shown in Figure 4.15 and Figure 4.16. The resulted spectra using either the linear polarizer or the circular polarizer were almost identical.

Similarly, the DR1 samples continued to redshift after exposure to polarized light with the other polarizer as illustrated in Figure 4.17 and Figure 4.18. It was noticed from the results shown in Figure 4.17 and Figure 4.18 as well as other tests performed (not shown here) that the exposure to circularly polarized light after linearly polarized light leads to a very slight increase in the reflection intensity (i.e., ~ 1 to 2%) and *vice versa*. However, this shift is generally small to introduce any meaningful impact for most of the potential applications, and further testing is needed for confirmation.

Figure 4.15 and Figure 4.16 show that the proposed system using DR1 can be used to dynamically tune colours in the visible spectra region. Thus, patterning with colours using the DR1 samples is possible as shown in Figure 4.19A. Figure 4.17 and Figure 4.18 indicate that, by utilizing linear and circular polarizers, only irreversible colour tuning is achievable with the DR1 samples. Furthermore, due to time limitations, the current colouration range produced here is not broad or highly vivid as shown in Figure 4.19B and Figure 4.19C. To help to understand the nature of the shift observed with the DR1 samples, estimations of the refractive index were performed.

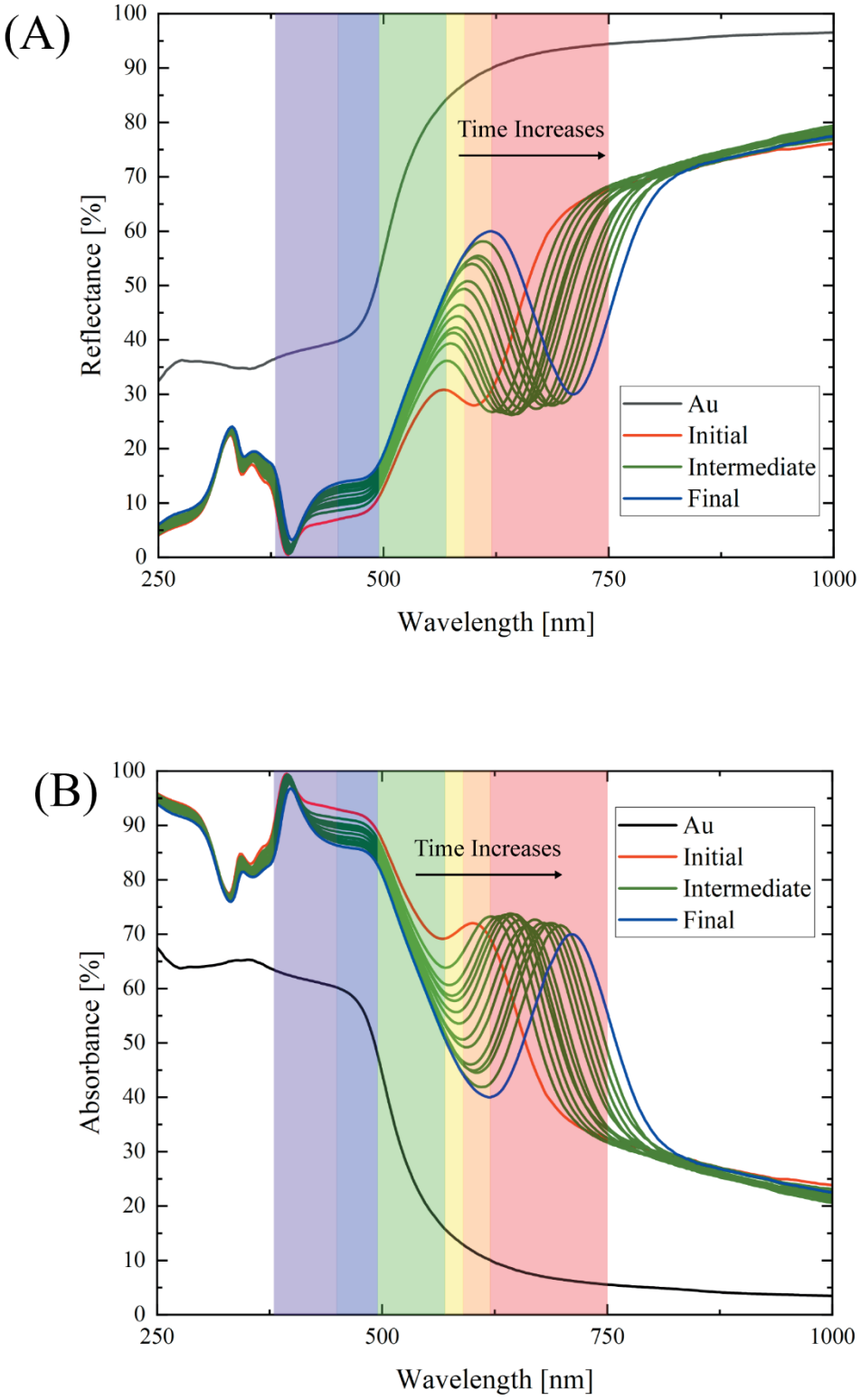

Figure 4.15. Effect of light exposure under different periods of time varying from 0 to 60 min on the DR1 samples. The initial stage (red lines) indicates the spectra before light exposure (0 min), while the final stage is indicated (blue lines) represents the samples after exposure for 60 min. The intermediate stages (green lines) show the spectra of the sample at time intervals of (2, 3, 4, 5, 7, 10, 15, 20, 25, 30 and 40) min. Exposure to linearly polarized light: **(A)** Reflection spectra; and **(B)** Absorbance spectra.

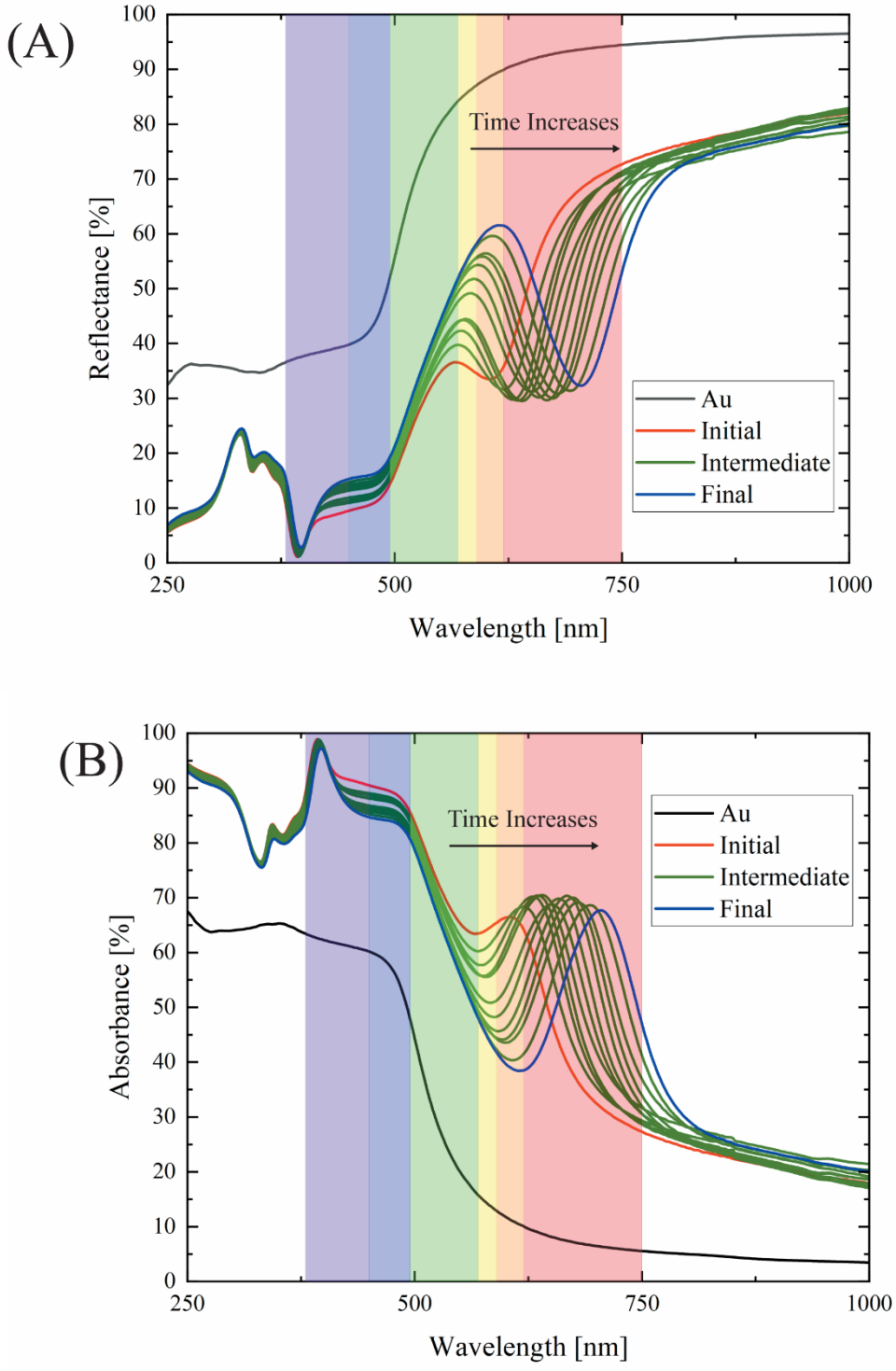

Figure 4.16. Effect of light exposure under different periods of time varying from 0 to 60 min on the DR1 samples. The initial stage (red lines) indicates the spectra before light exposure (0 min), while the final stage is indicated (blue lines) represents the samples after exposure for 60 min. The intermediate stages (green lines) show the spectra of the sample at time intervals of (2, 3, 4, 7, 10, 15, 20, 25 and 40) min. Exposure to circularly polarized light: **(A)** Reflection spectra; and **(B)** Absorbance spectra.

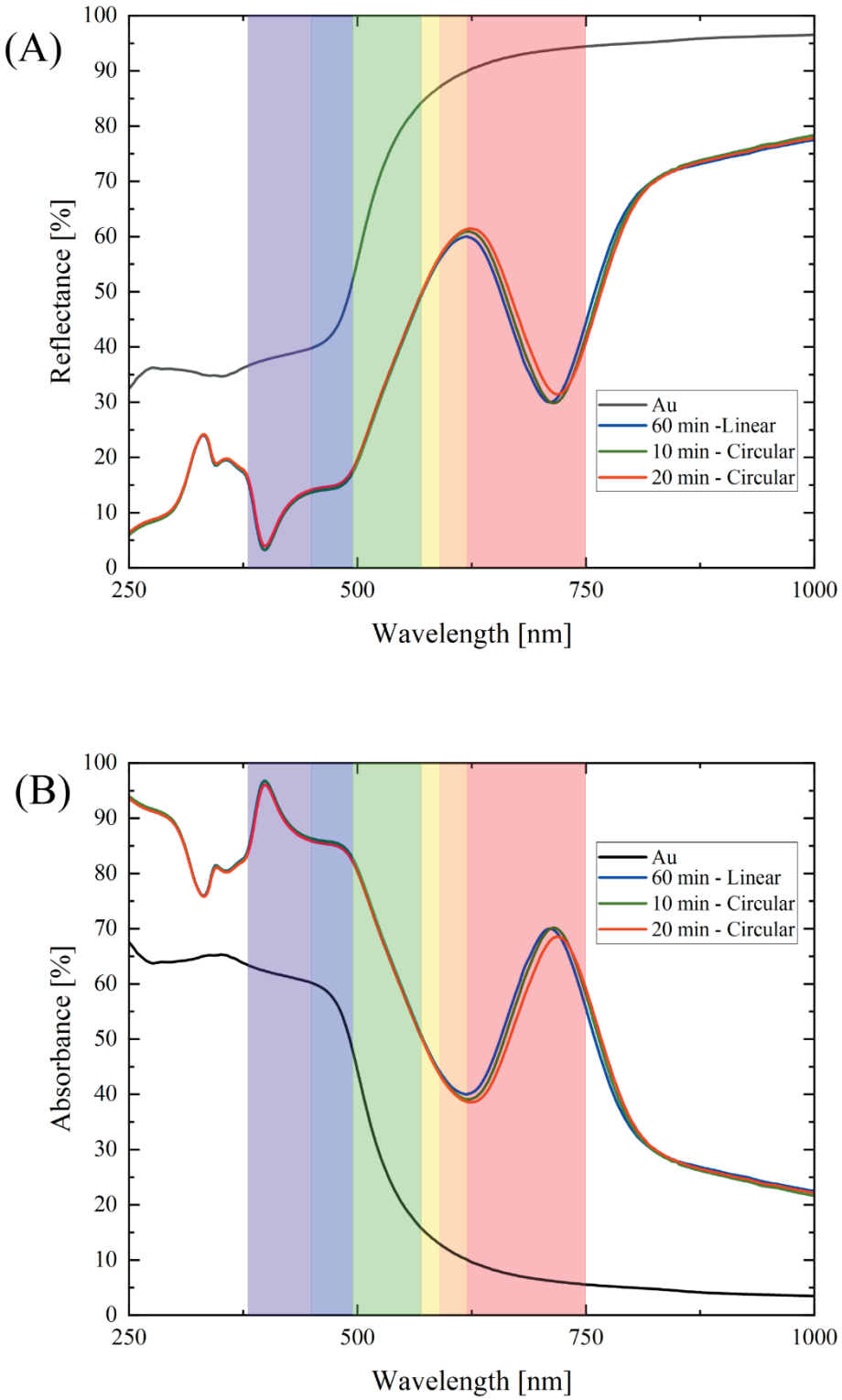

Figure 4.17. Effect of switching the type of polarized light on the DR1 samples from linearly polarized light to circularly polarized light. Spectra of the DR1 samples after an initial exposure of 60 min with linearly polarized light followed by circularly polarized light for 10 and 20 minutes: **(A)** Reflection spectra; and **(B)** Absorbance spectra.

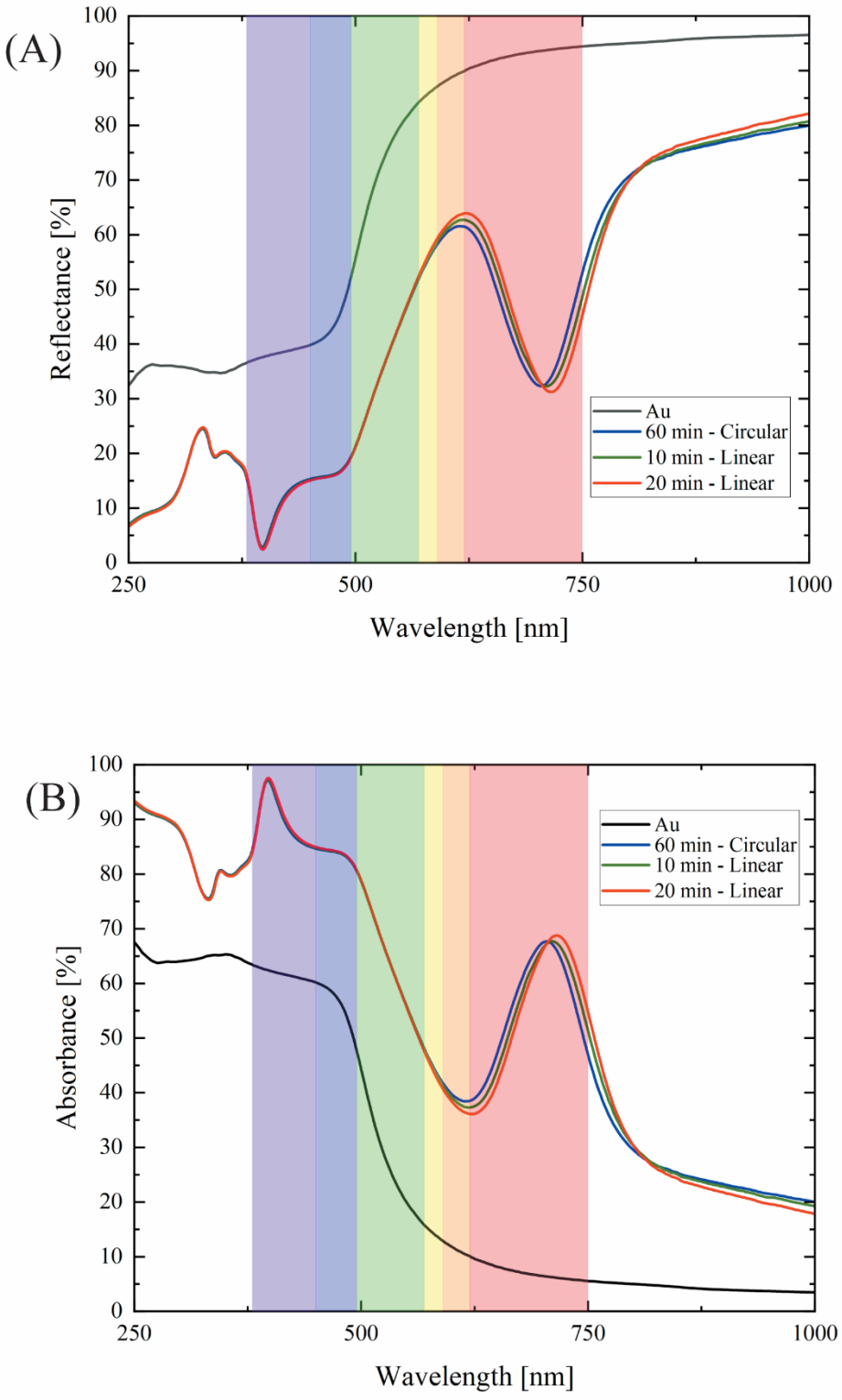

Figure 4.18. Effect of switching the type of polarized light on the DR1 samples from circularly polarized light to linearly polarized light. Spectra of the DR1 samples after an initial exposure of 60 min with circularly polarized light followed by linearly polarized light for 10 and 20 minutes: **(A)** Reflection spectra; and **(B)** Absorbance spectra.

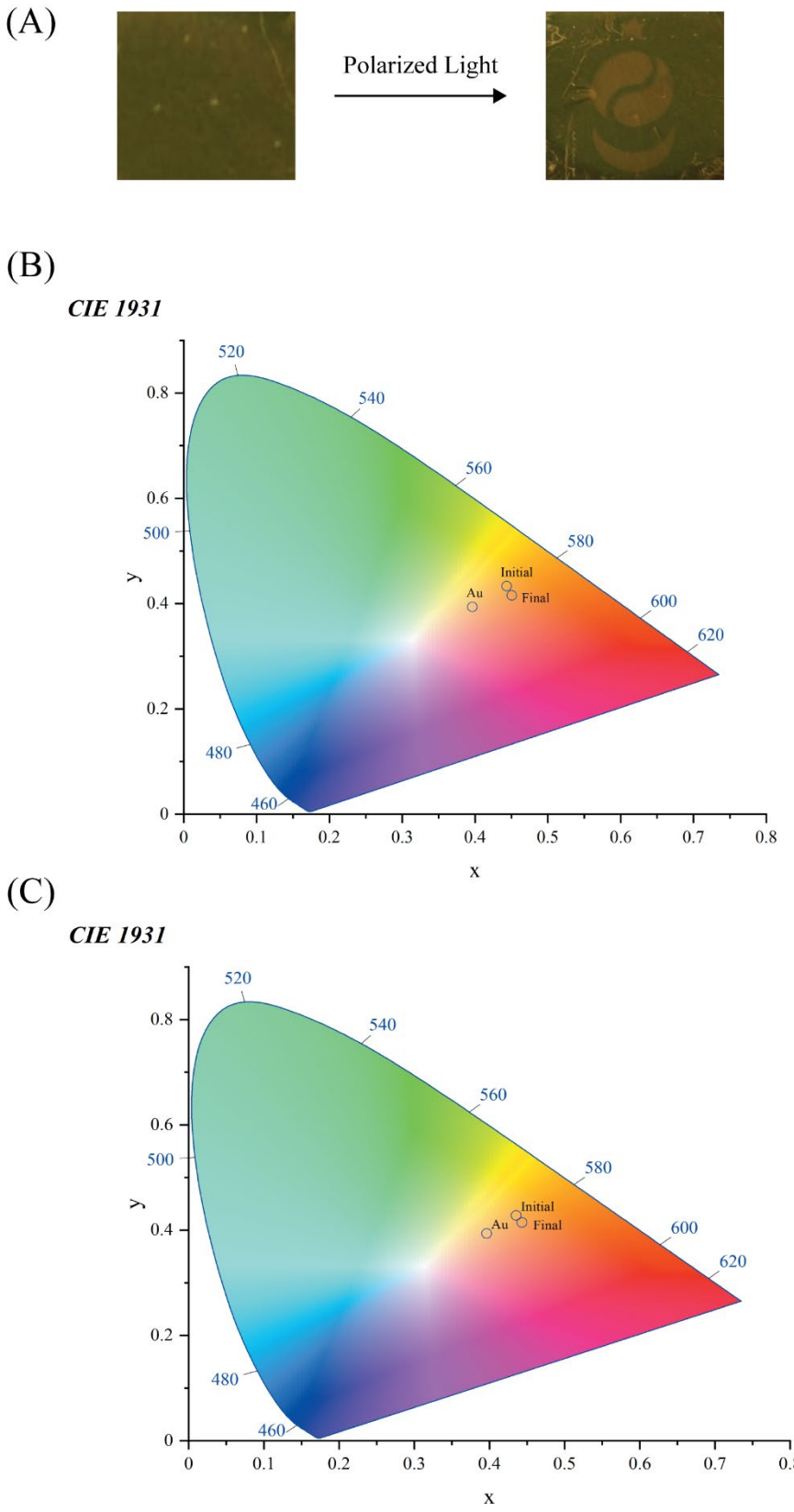

Figure 4.19. Colouration with DR1 samples. **(A)** Patterning with light exposure of a star (above), the yin and yang symbol (middle) and a crescent (below). Chromaticity diagrams of samples before exposure (Initial) and after 60 min of exposure (Final) to: **(B)** Linearly polarized light; and **(C)** Circularly polarized light.

4.3.2. Refractive Index Estimations

The modulation of the refractive index of materials allows for tuning of the optical properties. This modulation is performed by applying an external trigger, such as light. The probability of photon absorption by the photoactive molecule DR1 depends on the angle between the azo dipole axis and the light polarization (φ) [88]. The probability can be calculated as $\cos^2 \varphi$. Thus, φ can be set to 0^o as this leads to maximum absorption of light, thus a faster trans-to-cis isomerization, stronger birefringence and larger Δn [88], [133], [134].

In this work, the refractive index (n) and the extinction coefficient (k) of the DR1 samples were estimated based using the K-K Conversion method as presented in equation (3.3). The accuracy of the method was determined by comparing the estimations obtained for a thin film of 50 nm of Au on a silicon wafer with similar experimental data from the literature. The estimated n and k of the thin films of Au were compared with thin films of Au with thicknesses of 44 nm from Yakubovsky *et al.* [135] and 53 nm from Rosenblatt *et al.* [136] as presented in Figure 4.20. The figure shows that the estimations are close to the experimental data. Thus, the estimations of n and k for DR1 samples are assumed to be close to the experimental measurements.

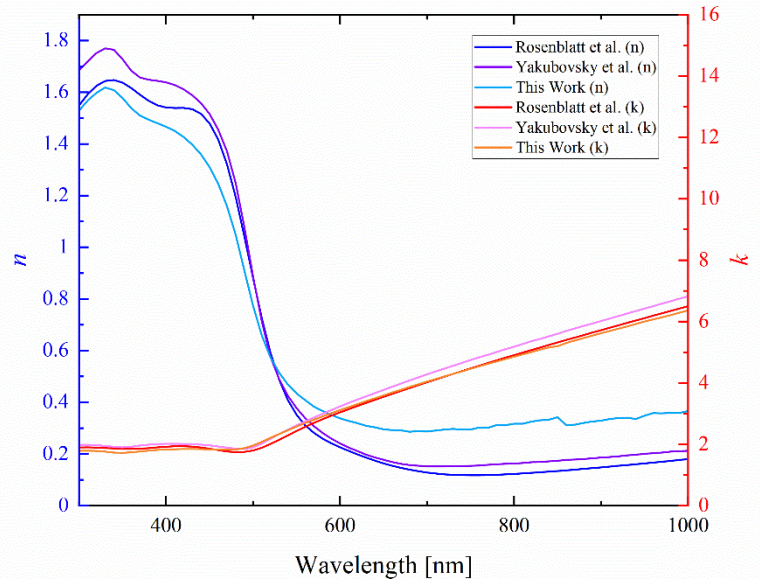

Figure 4.20. A comparison between the estimated data of the refractive index (n) and the extinction coefficient (k) in this work using the K-K conversion method with reported experimental measurements from the literature of thin films of gold. The thicknesses of Au films are: 44 nm (Yakubovsky *et al.*), 50 nm (this work) and 53 nm (Rosenblatt *et al.*).

The estimation results for the DR1 samples show an increase in both *n* and *k* as the time of the exposure increases regardless of the type of polarizer used as shown in Figure 4.21. Both components of the refractive index increased by at least ~ 35% after 60 min of exposure (Linear: $\Delta\eta \sim 58\%$, $\Delta k \sim 49\%$; Circular: $\Delta\eta \sim 60\%$, $\Delta k \sim 35\%$). Generally, increasing the light intensity leads to an increase in the refractive index. However, the refractive index could change even though the change in the spectra intensity might be very small (i.e., 0.03%) [88]. In this work, the refractive index changed drastically, but the change in the spectra intensity is insignificant, as shown in Figure 4.15 and Figure 4.16. Hence, it is assumed that the change in the refractive index here is mainly attributed to the isomerization of DR1 [88].

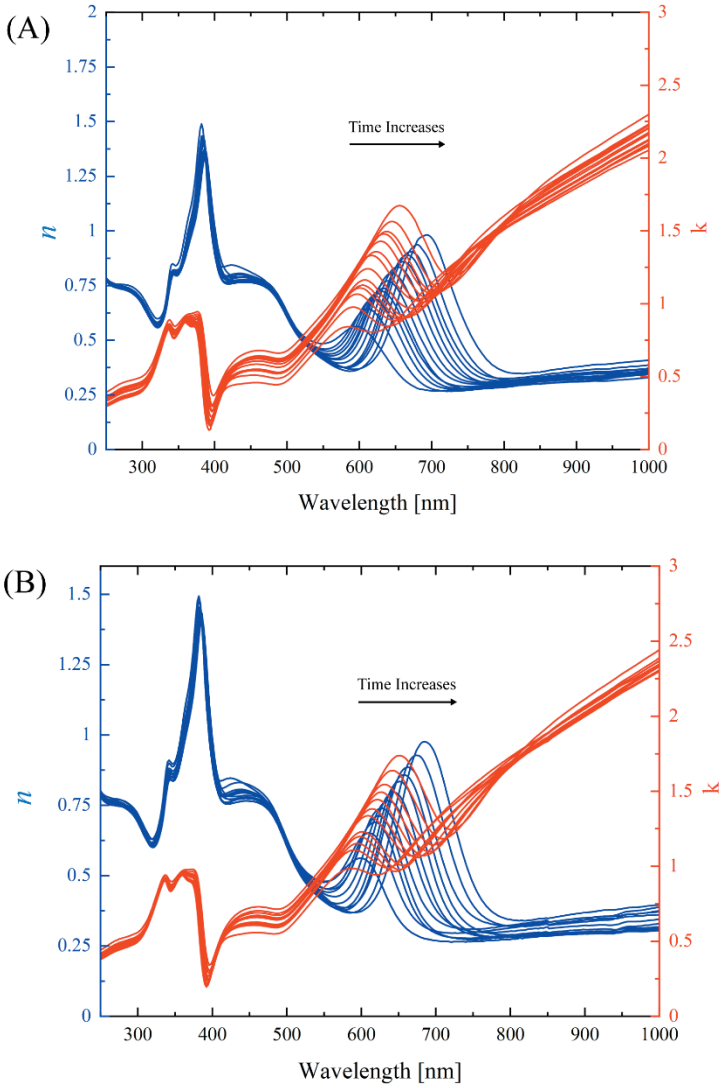

Figure 4.21. Effect of the irradiation on the refractive index of DR1 samples. *n* and *k* variation with increasing the exposure time under: **(A)** Linearly polarized light; and **(B)** Circularly polarized light

Figure 4.22 shows that both parts of the refractive index (i.e., n and k) at different resonant wavelengths can be estimated with linear equations. The equations corresponding to the fit for the refractive index are shown below for both types of polarizers and were found to exhibit high goodness of fit (n: R^2 ~ 99% and k: R^2 ~ 96%).

Linear

$$n = (0.00285)\lambda_r - 1.13661$$
$$k = (0.00354)\lambda_r - 1.31169 \quad (4.2)$$

Circular

$$n = (0.00311)\lambda_r - 1.29992$$
$$k = (0.00324)\lambda_r - 1.01389 \quad (4.3)$$

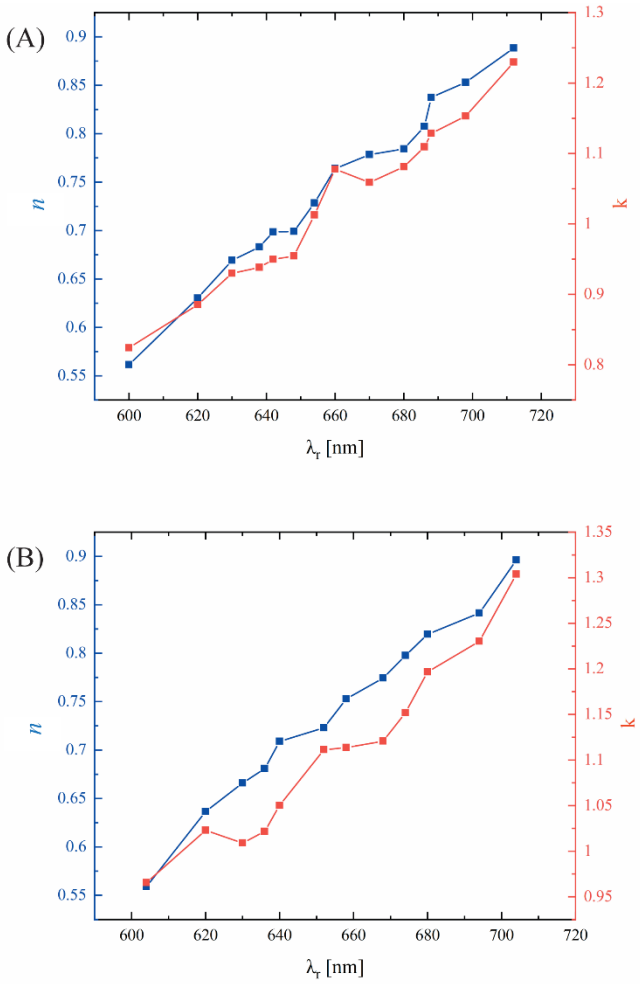

Figure 4.22. Refractive index (n) and extinction coefficient (k) values at the resonant wavelength for different duration of times from 0 (Before exposure) to 60 min under exposure to: **(A)** Linearly polarized light; and **(B)** Circularly polarized light.

The change in the refractive index of the DR1 samples is also assumed to be influenced to some degree by the surface mass patterning of the surface topography resulting from light irradiation [89]. DR1 is reported to exhibit photophysical motion when irradiated with light [137], [138]. These photophysical motions respond differently to varying light intensities and/or polarizations [89].

In this work, a DR1 layer sandwiched between two layers of PAH, as shown in Figure 4.23A, was used to examine the surface mass patterning of the DR1 samples. The extra layer of PAH was added as these surface mass patterns are generally observed at relatively thicker layers on micron and nanoscale [89]. Indefinite surface mass patterns were noticeable with the prepared samples as shown in Figure 4.23B. The SEM image shows two regions (light) and (dark) of a sample that was unexposed to any type of light.

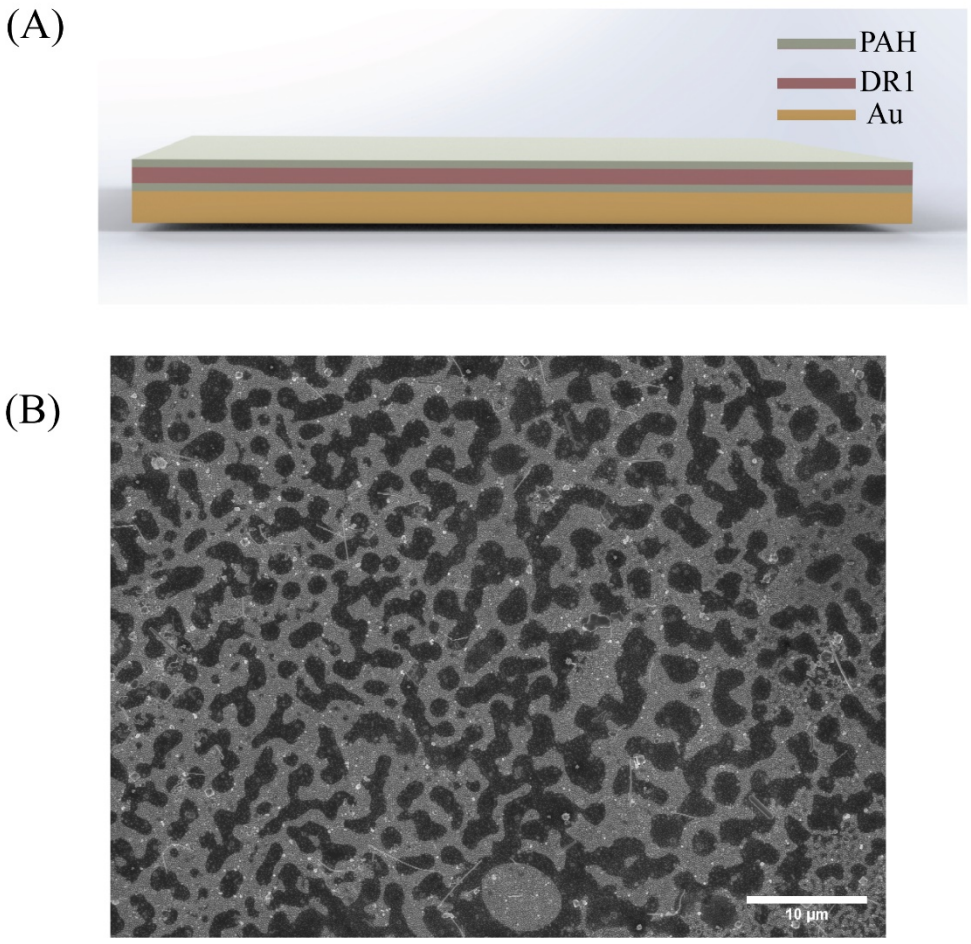

Figure 4.23. (A) Schematic of the structure of the DR1 samples prepared with two layers of PAH; and **(B)** SEM image of a DR1 sample with two layers of PAH before exposure to light. The image was taken with WD ~ 8.8 mm.

Then, two samples exposed to linearly and circularly polarized light were examined. The first sample was exposed to linearly polarized light for 60 min followed by circularly polarized light for 20 min. The SEM image of the sample showed more domination of the lighter region as illustrated in Figure 4.24A. In contrast, the second sample was irradiated for 60 min with circularly polarized light followed by 20 min of linearly polarized light. The surface analysis of the sample showed more domination of the darker region as illustrated in Figure 4.24B.

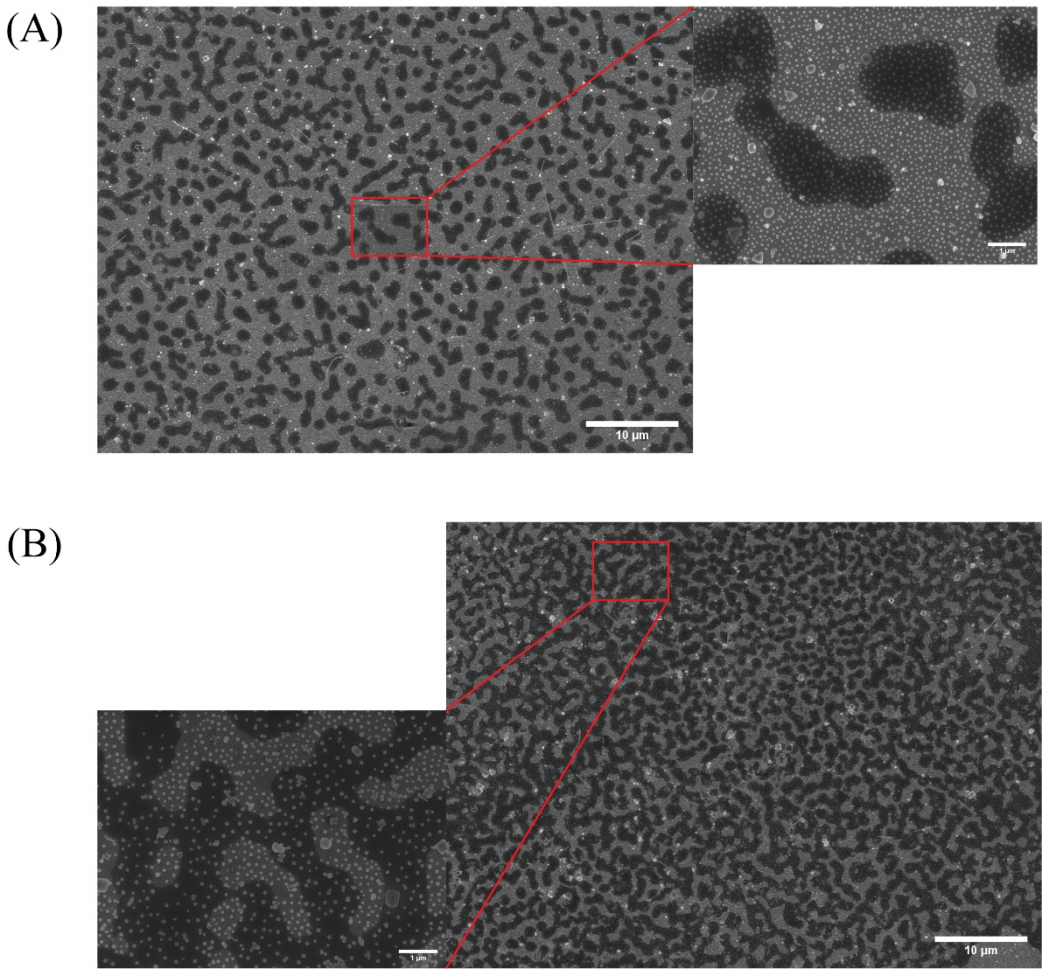

Figure 4.24. (A) SEM image of a DR1 sample with two layers of PAH after exposure linearly polarized light for 60 min followed by circularly polarized light for 20 min. **(B)** SEM image of a DR1 sample with two layers of PAH after exposure circularly polarized light for 60 min followed by linearly polarized light for 20 min. Both images were taken with WD ~ 8.7 mm.

The change observed in the two regions (i.e., light and dark) might indicate a change in the surface height of the samples with irradiation. However, experimental tests have

not been conducted to verify this suggestion as the surface mass patterning of DR1 is out of the scope of this work. It is reported, however, that regions on samples exposed to higher light intensities had smaller heights on the surface, while higher regions corresponded to lower exposure [89]. Furthermore, studies show that the azo chromophores align against the direction of polarization [139], [140]. Linear polarizers lead to high mass transport of DR1 (i.e., accumulations in specific regions), and circular polarizers provide the best quality of patterning [141], [142]. Thus, a combination of both is usually used.

Even though the photophysical motion of photoactive molecules was discovered in 1995 and has been investigated extensively, many fundamental questions are still not well answered, such as the nature of the driving force behind it [143]-[146]. For example, some researchers have suggested that the material mobility increases noticeably during irradiation due to photo-plasticising or photo-softening [147]-[149]. Unfortunately, this explanation has not been proved experimentally. Others have suggested that it is related to local thermal gradient, but this argument can neither explain why the surface patterning still occurs at low insanities nor the dependency on polarization [150]-[152]. A mean-field theory attributing this behaviour to the attraction between the oriented chromophores has been proposed, but it suggests that the accumulation of the material would be in the brighter regions [153], [154]. This contradicts the reported experimental results as explained earlier. The mass transport has also been suggested to be due to pressure gradient as a response to the induced light gradient [155], [156]. Although this suggestion explains well the photochemical effects, it does not fully account for the dependency on polarization.

Overall, it can be said the tuning of the resonant wavelength observed with the DR1 samples is associated with the modulation of the refractive index. The change in the refractive index, here, is assumed to be mainly governed by the isomerisation of DR1 upon irradiation. However, it can also be suggested that the change in the refractive index is affected, at least to some degree, by the photophysical motion o the DR1 samples. The refractive index is vital to examine the optical behaviour but to assess the plasmonic nature determining the quality factor is more crucial.

4.3.3. Quality Factor Calculations

The quality factor (Q) is a measure of the efficiency of energy storage of a plasmonic cavity as well as the strength and the width of the resonance. It generally becomes smaller by the loss in plasmon channels (e.g., surface roughness and geometry of the nanostructures) [157]-[159]. Plasmonic surfaces require high-quality factors (i.e., ≥ 8) to be exploited effectively in real-life applications [159], [160]. However, the realization of plasmonic surfaces with high Q values has been limited due to several factors including disorder, heterogeneities of the components and realistic losses [161]-[163]. Nanocubes allow for relatively high-quality factors that are generally ~ 2.3x higher than that of spheroids due to their smooth facets that allow for a better parallel-plate cavity with the thin film [111]. These cavities allow for high resonances because of the low confinement thin-film and the nanocrystals [111].

In this work, the quality factor decreases by ~ 57% for DR1 samples after 60 min of irradiation using both types of polarizers as shown in Figure 4.25. As the separation distance between the NCs decreases and their density increases due to photophysical motion of DR1 resulting from irradiation, the coupled LSPRs of adjacent NCs are assumed to form a quasi-continuous resonance [111]. This resonance and the out-of-plane interactions (i.e, the interaction between the nanocubes and the thin film) lead to redshifting the fundamental mode of the system and broadening it significantly (i.e., *FWHM* increases by ~ 175%) because of the increase in the radiation damping [111] as shown in Figure 4.26. The increase in the radiation damping could be attributed to the high radiation power along the surface, which leads to a stronger scattering of plasmons [164]. The *FWHM* as well as the Q at different values of λ_r can be estimated using second-degree polynomial equations (*FWHM*: $R^2 > 99\%$ and Q: $R^2 \sim 96\%$). The results plotted against time scale for Q and *FWHM* are provided in the appendix in Figure A.1.

Linear

$$FWHM = (-0.00276)\lambda_r{}^2 + (4.10831)\lambda_r - 1441.55$$
$$Q = (0.00136)\lambda_r{}^2 - (1.86945)\lambda_r + 650.79 \quad (4.4)$$

Circular

$$FWHM = (-0.00257)\lambda_r{}^2 + (3.83561)\lambda_r - 1348.28$$
$$Q = (0.00143)\lambda_r{}^2 - (1.95495)\lambda_r + 679.12 \quad (4.5)$$

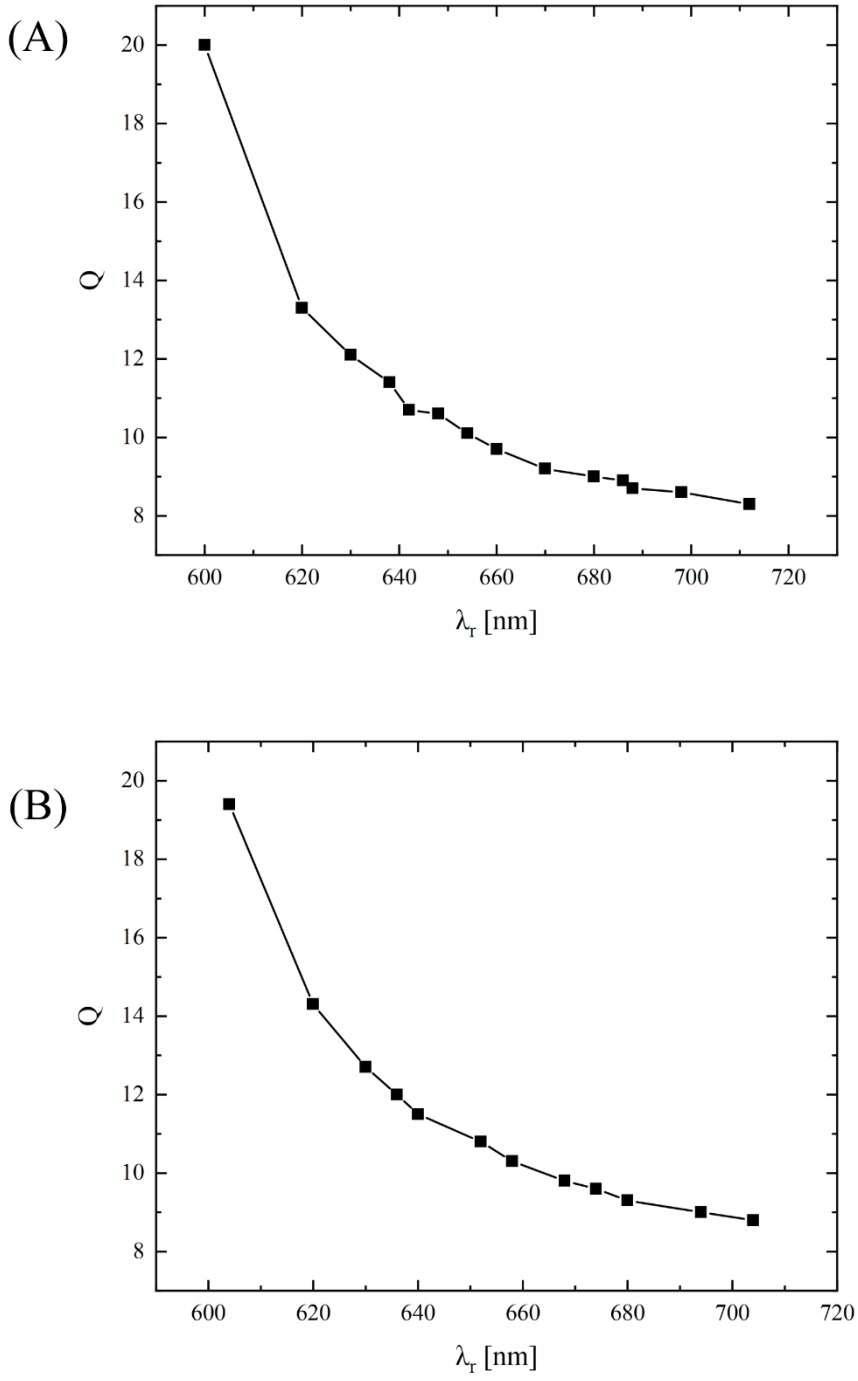

Figure 4.25. Effect of the irradiation on the quality factor (Q) of the DR1 samples under: **(A)** Linearly polarized light; and **(B)** Circularly polarized light. The quality factor decreases with the increase of the irradiation time. λ_r indicates the corresponding values of the resonant wavelength. The time intervals vary from 0 min (Before exposure) to 60 min of exposure to polarized light.

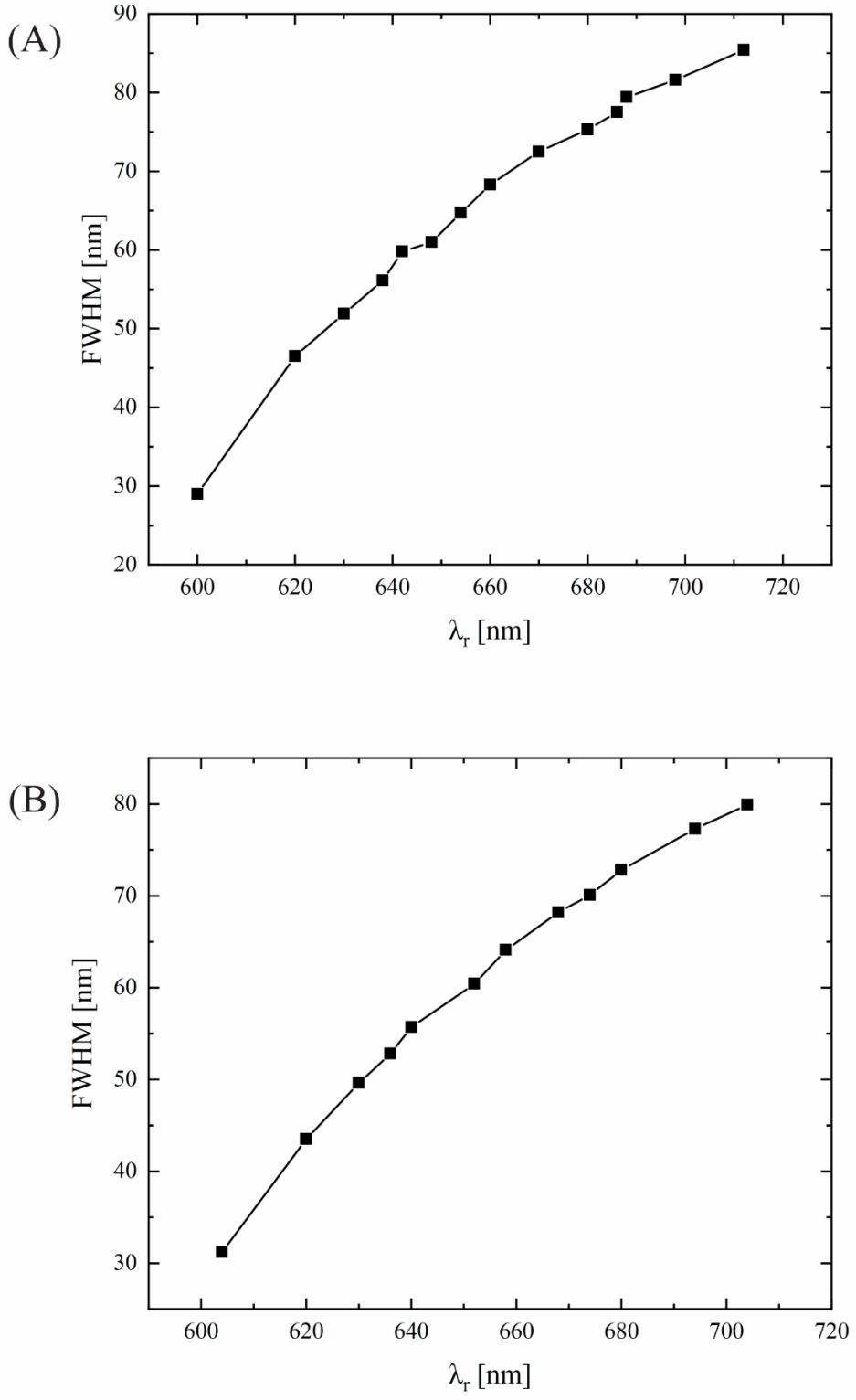

Figure 4.26. Effect of the irradiation on the full width at half maximum (*FWHM*) of the DR1 samples under: **(A)** Linearly polarized light; and **(B)** Circularly polarized light. The *FWHM* increases with the increase of the irradiation time. λ_r indicates the corresponding values of the resonant wavelength. The time intervals vary from 0 min (Before exposure) to 60 min of exposure to polarized light.

4.3.4. Surface Plasmon Sensing

Finally, we estimated the surface plasmon sensing of the DR1 samples to examine their suitability for sensing applications. Surface plasmon sensors determine the shift of an SPR by detecting the change in the refractive index at the vicinity of the surface [165]. Ideally, perfect absorption with a narrow bandwidth and a strong electromagnetic field is highly desirable for refractive index sensors as it enables detecting small changes in the refractive index due to the significant change in the spectral intensity and position [67]. Two main parameters are used to define the performance of the material for sensing applications: i) sensitivity (*S*); and ii) figure of merit (*FOM*) [116]. The sensitivity is a measure of the change in the resonant wavelength associated with the change in the refractive index. However, S alone is not sufficient to well determine the overall sensitivity of a material as it does not consider the sharpness of the resonance. Thus, the figure of merit is utilized, which takes the resonant bandwidth into account. Higher values of both *S* and *FOM* are generally more desirable for most of the applications, which indicates a higher sensitivity.

In this work, even though the sensitivity can be said to be increasing with exposure time as shown in Figure 4.27, the figure of merit is mainly declining as illustrated in Figure 4.28. The decline in the *FOM* is because of the broadening of the resonant wavelength (i.e., an increase of *FWHM*) with irradiation time due to the formation of quasi-continuous resonance and out-of-plane interactions. The values obtained here as per the author knowledge are comparable to other works in the literature with similar values of *S* and *FOM*, such as Madadi *et al.* [166]. Best values for the sensitivity estimations were obtained with an exposure time of 5 min ($\lambda_r \sim$ 648 nm, $S \sim$ 349 nm/RIU and $FOM \sim 5.72$) using the linear polarizer and 7 min ($\lambda_r \sim$ 652 nm, $S \sim$ 293 nm/RIU and $FOM \sim 4.84$) using the circular polarizer. The higher values of *S* and *FOM* for the DR1 sample exposed to linearly polarized light could be due to a higher mass transport of DR1 resulting from using the linear polarizer or could be simply due to the variation in the samples because of artefacts.

The results plotted against time scale for S and FOM are provided in the appendix in Figure A.2. The exact values of the different parameters (i.e., *n*, *k*, *Q*, *FWHM*, *S* and

FOM) of the two samples represented in Figure 4.22 and Figure 4.25 to Figure 4.28 are shown in Table A.1 and Table A.2.

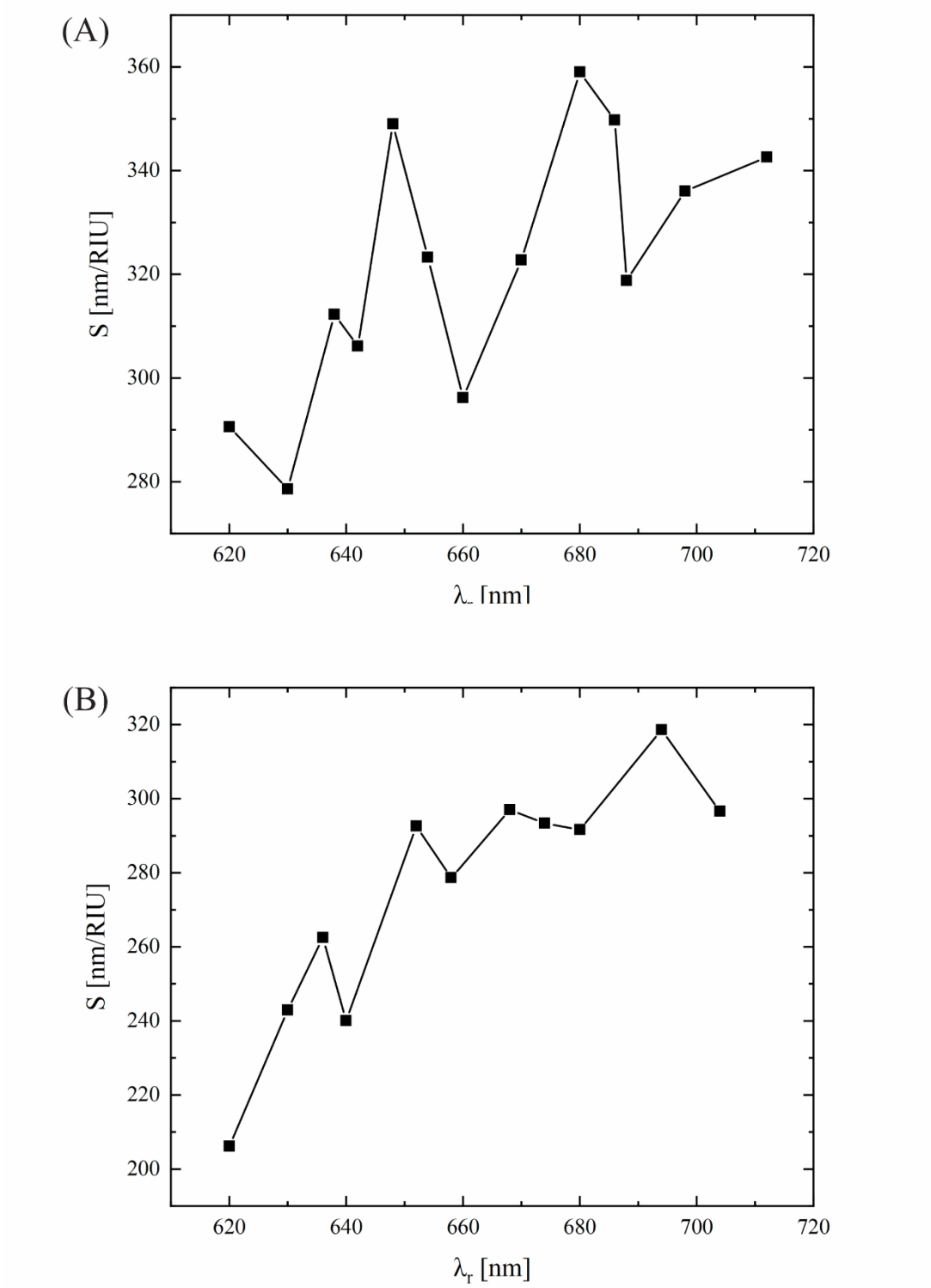

Figure 4.27. Effect of the irradiation on the sensitivity (*S*) of the DR1 samples under: **(A)** Linearly polarized light; and **(B)** Circularly polarized light. *S* generally increases with the increase of the irradiation time. λ_r indicates the corresponding values of the resonant wavelength. The time intervals vary from 0 min (Before exposure) to 60 min of exposure to polarized light.

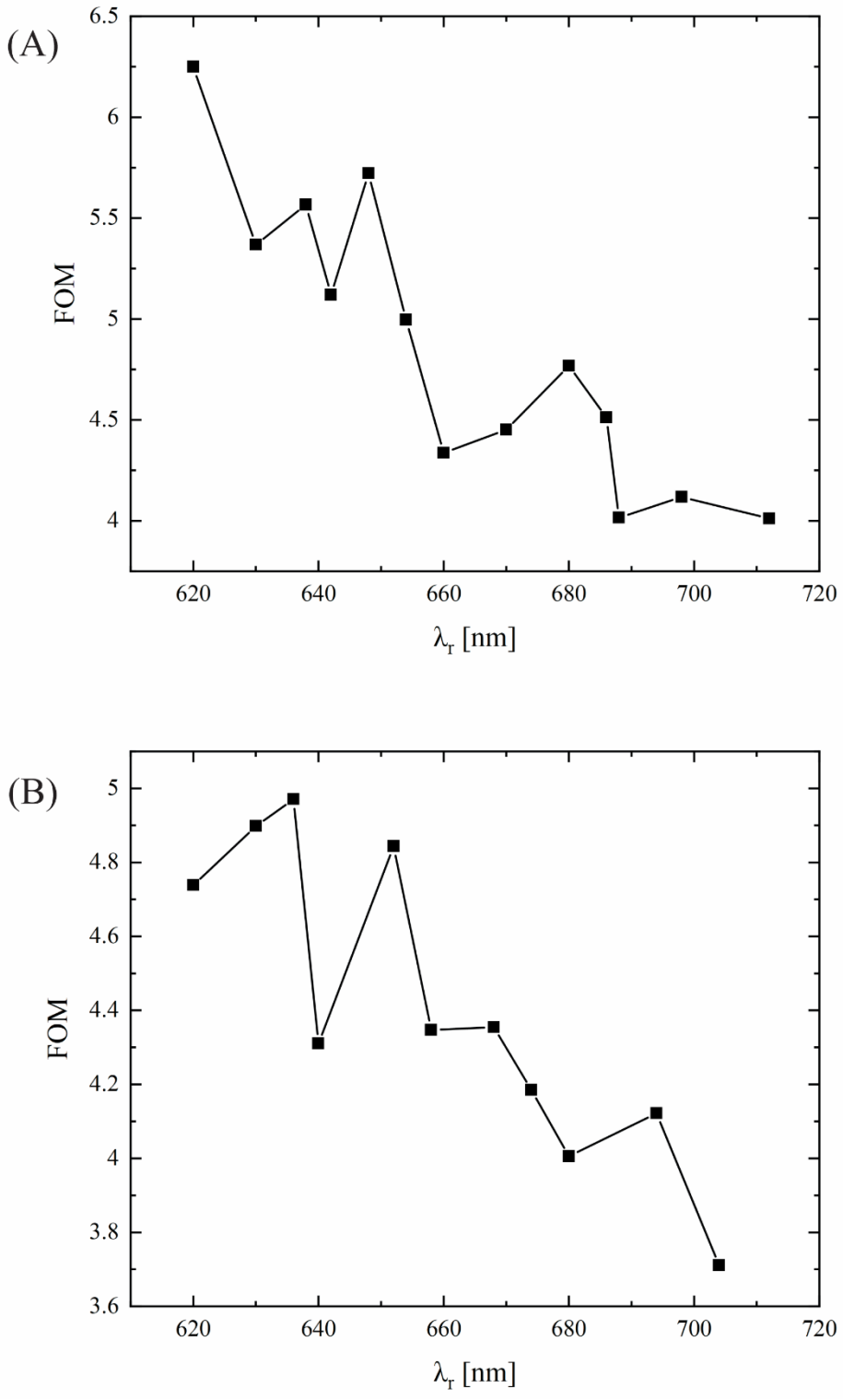

Figure 4.28. Effect of the irradiation on the figure of merit (*FOM*) of the DR1 samples under: **(A)** Linearly polarized light; and **(B)** Circularly polarized light. *FOM* generally decreases with the increase of the irradiation time. λ_r indicates the corresponding values of the resonant wavelength. The time intervals vary from 0 min (Before exposure) to 60 min of exposure to polarized light.

Chapter 5: Conclusions

In this work, we were able to fabricate photoactive plasmonic surfaces utilizing a layer-by-layer (LBL) deposition to tune colours dynamically. The system used AgNCs ($l \sim 66 \pm 8$ nm) as the nanoantennas to modulate the plasmonic behaviour. The TEM and SEM images showed high monodispersity and good distribution on the surface of the samples.

Initially, preliminary studies were conducted for a LBL plasmonic system to examine its suitability for the proposed photoactive plasmonic surfaces. The LBL plasmonic system utilized two opposingly charged PEs (i.e., PAH and PSS) that are deposited on a thin film of Au. Samples with one to seven PEs layers were prepared. The samples showed high absorption (up to ~ 93%) at the resonant peak and an increasing quality factor from 6.3 to 16.7 with the increase of the number of layers. The absorbance can be increased further to a near-perfect absorption with further optimization of the AgNCs (e.g., increasing the edge size or the sharpness of the corners). Colouration by tuning the resonant wavelength was achieved in the visible region with a tuning range of 234 nm by controlling the thickness of the spacer. Furthermore, samples of multiple layers of PEs showed reversible colour switching with humidity due to the swelling of the outermost layer of the spacer. Oxidization of the samples was observed with time leading to a redshift of ~ 50 nm in the resonant wavelength and a reduction in the absorption after about three months. This could be solved by replacing Ag with another material (e.g., Au) but the high-quality factor and affordable price of Ag still make it attractive as the shift is not fast and/or dramatic.

After that, a LBL system utilizing disperse red 1 (DR1) was proposed to fabricate light-responsive active plasmonic surfaces. The prepared DR1 samples exhibited some inconsistency in the intensity of spectra due to the inability of the DR1 solution to adhere properly to the Au substrate and thus affecting the adhesion of both PAH and AgNCs. This could be solved by functionalizing the Au substrate with hydrophobic thiol. Alternatively, the samples could be exposed to plasma after spin coating and

before dip coating with PAH to improve the surface charge. Results showed that increasing the exposure time to linearly and/or circularly polarized light leads to a redshift of the resonant spectra, while a negligible change in the intensity. A redshift, as large as ~ 112 nm, was obtained after 60 min of irradiation. In terms of colour modulation, the DR1 samples exhibited excellent dynamic colour modulation, but relatively low vividness. Nevertheless, the patterning on the samples was achievable. Additionally, the DR1 samples showed high-quality factors (Q) even after exposure to light for a long period of time (i.e., $Q > 8$) making them attractive to different applications in plasmonics (e.g., sensing). Furthermore, the refractive index (n and k) of the DR1 samples as well as their sensitivity (S) and figure of merit (FOM) were estimated. The samples showed an increase of both components of the refractive index with time. The change in the refractive index, and hence the shift in the resonant wavelength, was attributed to the isomerisation of DR1 and probably to the surface mass transport exhibited by DR1. The estimated values of S and FOM here indicated a potential for the system to be utilized as a surface plasmon sensor. The bandwidth of the resonant wavelength can be narrowed by several possible designs, such as subgroup decomposition, hybridization or transforming optics (i.e., to increase the FOM and Q by decreasing $FWHM$). Moreover, the shape of the nanostructures can be optimized further to increase the sensitivity, and thus the FOM.

The results obtained in this thesis indicates a high potential to utilize the LBL deposition to fabricate dynamically tuned active plasmonic surfaces due to its simplicity, relatively low cost and overall high performance. Future research could optimize the proposed system to cover a wider range of the spectrum. Furthermore, other photoactive molecules could be tested to fabricate photoactive plasmonic surfaces with dynamically reversible colour modulation. Such plasmonic surfaces/materials could dramatically shift different current markets (e.g., displays, fashion and architecture) due to the potential of large-scale production.

References

[1] M. Zubairy, M. El-Gomati and M. Al-Amri, *Optics in our Time.* Cham, Switzerland: Springer International Publishing, 2016.

[2] K. Xiong, D. Tordera, M. Jonsson, A. Dahlin, Active control of plasmonic colors: Emerging display technologies, RoPP 82 (2019) 024501.

[3] L. Shao, X. Zhuo, J. Wang, Advanced plasmonic materials for dynamic color display, Advanced Materials 30 (2018) e1704338.

[4] D. Graham-Rowe, Electronic paper rewrites the rulebook for displays, Nature Photonics 1 (2007) 248-251.

[5] X. Duan, N. Liu, Scanning plasmonic color display, ACS Nano 12 (2018) 8817-8823.

[6] L. Lubos, The role of colors in stress reduction, Liceo Journal of Higher Education Research 5 (2008) 95.

[7] C. Magoulas, "How Color Affects Food Choices." , University of Nevada, Las Vegas, 2009.

[8] M. Dzulkifli, M. Mustafar, The influence of colour on memory performance: A review, The Malaysian Journal of Medical Sciences 20 (2013) 3-9.

[9] F. Neubrech, X. Duan, N. Liu, Dynamic plasmonic color generation enabled by functional materials, Science Advances 6 (2020) eabc2709.

[10] Y. Gu, L. Zhang, J. Yang, S. P. Yeo, C. Qiu, Color generation via subwavelength plasmonic nanostructures, Nanoscale 7 (2015) 649-6419.

[11] Y. Liu, G. Si, E. Leong, N. Xiang, A. Danner, J. Teng, Light-driven plasmonic color filters by overlaying photoresponsive liquid crystals on gold annular aperture arrays, Advanced Materials 24 (2012) OP131-OP135.

[12] T. Lee, J. Jang, H. Jeong, J. Rho, Plasmonic- and dielectric-based structural coloring: From fundamentals to practical applications, Nano Convergence 5 (2018) 1-21.

[13] Y. Sun, Y. Xia, Gold and silver nanoparticles: A class of chromophores with colors tunable in the range from 400 to 750 nm, Analyst 128 (2003) 686-691.

[14] L. Liz-Marzán, Nanometals: Formation and color, Materials Today 7 (2004) 26-31.

[15] C. Koechlin, P. Bouchon, F. Pardo, J. Jaeck, X. Lafosse, J. Pelouard, R. Haïdar, Total routing and absorption of photons in dual color plasmonic antennas, Applied Physics Letters 99 (2011) 241104.

[16] R. Yu, P. Mazumder, N. Borrelli, A. Carrilero, D. Ghosh, R. Maniyara, D. Baker, F. García de Abajo, V. Pruneri, Structural coloring of glass using dewetted nanoparticles and ultrathin films of metals, ACS Photonics 3 (2016) 1194−1201.

[17] T. James, P. Mulvaney, A. Roberts, The plasmonic pixel: Large area, wide gamut color reproduction using aluminum nanostructures, Nano Letters 16 (2016) 3817-3823.

[18] Y. Shen, V. Rinnerbauer, I. Wang, V. Stelmakh, J. Joannopoulos, M. Soljačić, Structural colors from fano resonances, ACS Photonics 2 (2015) 27-32.

[19] Y. Liu, G. Si, E. Leong, B. Wang, A. Danner, X. Yuan, J. Teng, Optically tunable plasmonic color filters, Appl. Phys. A 107 (2012) 49-54.

[20] Y. Chou Chau, K. Chen, H. Chiang, C. Lim, H. Huang, C. Lai, N. Kumara, Fabrication and characterization of a metallic-dielectric nanorod array by nanosphere lithography for plasmonic sensing application, Nanomaterials 9 (2019) 1691.

[21] A. Kristensen, J. Yang, S. I. Bozhevolnyi, S. Link, P. Nordlander, N. Halas, N. Mortensen, Plasmonic colour generation, Nature Reviews. Materials 2 (2016) 16088.

[22] J. Stewart, G. Akselrod, D. Smith, M. Mikkelsen, Toward multispectral imaging with colloidal metasurface pixels, Advanced Materials 29 (2017) 1602971.

[23] G. Akselrod, J. Huang, T. Hoang, P. Bowen, L. Su, D. Smith, M. Mikkelsen, Large-area metasurface perfect absorbers from visible to near-infrared, Advanced Materials 27 (2015) 8028-8034.

[24] H. Koerner, T. White, N. Tabiryan, T. Bunning, R. Vaia, Photogenerating work from polymers, Materials Today 11 (2008) 34-42.

[25] Yager, K.,Barrett, C. "Azobenzene polymers for photonic applications," in *Smart Light-Responsive Materials*, Y. Zhao and T. Ikeda, Eds. Hoboken, NJ, USA: John Wiley & Sons, Inc, 2009, pp. 1-46.

[26] Z. Mahimwalla, K. Yager, J. Mamiya, A. Shishido, A. Priimagi, C. Barrett, Azobenzene photomechanics: Prospects and potential applications, Polym. Bull 69 (2012) 967-1006.

[27] L. Lu-Ying, Z. You-Yuan, L. Fu-Ming, Y. Jian, C. Guo-Rong, W. Chang-Chun, Orientation-enhanced photorefractive effect in PVK-PBA:DR1:TNF polymer, Chinese Physics Letters 21 (2004) 1535-1538.

[28] Y. Wang, G. Carlisle, Optical properties of disperse-red-1-doped nematic liquid crystal, Journal of Materials Science: Materials in Electronics 13 (2002) 173-178.

[29] D. Nesterov, M. Fedorova, Colour perception in ancient world, IOP Conference Series. Materials Science and Engineering 262 (2017) 12139.

[30] A. Elliot, Color and psychological functioning: A review of theoretical and empirical work, Frontiers in Psychology 6 (2015) 368.

[31] M. Assad, S. Homaeigohar, M. Elbahri, Reflective coloration from structural plasmonic to disordered polarizonic, Advanced Photonics Research (2021) 2100009.

[32] A. Shrivastava, *Introduction to Plastics Engineering.* Saint Louis: Elsevier Science & Technology Books, 2018.

[33] M. Aminof and R. Daroff, *Encyclopedia of the Neurological Sciences.* (2nd ed.) Amsterdam: Academic Press/Elsevier, 2014.

[34] K. Buschow *et al*, *Encyclopedia of Materials Science and Technology.* Oxford: Pergamon Press, 2001.

[35] L. McManus and R. Mitchell, *Pathobiology of Human Disease.* Saint Louis: Elsevier Science & Technology, 2014.

[36] M. Brongersma, Introductory lecture: Nanoplasmonics, Faraday Discussions 178 (2015) 9-36.

[37] V. Giannini, A. Fernández-Domínguez, S. C. Heck, S. Maier, Plasmonic nanoantennas: Fundamentals and their use in controlling the radiative properties of nanoemitters, Chemical Reviews 111 (2011) 3888-3912.

[38] D. Gramotnev, S. Bozhevolnyi, Plasmonics beyond the diffraction limit, Nature Photonics 4 (2010) 83-91.

[39] W. Cai, M. Brongersma, J. White, E. Barnard, Y. C. Jun, J. Schuller, Plasmonics for extreme light concentration and manipulation, Nature Materials 9 (2010) 193-204.

[40] S. Lal, N. Halas, S. Link, Nano-optics from sensing to waveguiding, Nature Photonics 1 (2007) 641-648.

[41] E. Hutter, J. Fendler, Exploitation of localized surface plasmon resonance, Advanced Materials 16 (2004) 1685-1706.

[42] M. Rycenga, C. Cobley, J. Zeng, W. Li, C. Moran, Q. Zhang, D. Qin, Y. Xia, Controlling the synthesis and assembly of silver nanostructures for plasmonic applications, Chemical Reviews 111 (2011) 3669-3712.

[43] C. Girard, E. Dujardin, G. Baffou, R. Quidant, Shaping and manipulation of light fields with bottom-up plasmonic structures, New Journal of Physics 10 (2008) 105016.

[44] A. Petukhova, Z. Nie, E. Kumacheva, Properties and emerging applications of self-assembled structures made from inorganic nanoparticles, Nature Nanotechnology 5 (2010) 15-25.

[45] D. Talapin, J. Lee, M. Kovalenko, E. Shevchenko, Prospects of colloidal nanocrystals for electronic and optoelectronic applications, Chemical Reviews 110 (2010) 389-458.

[46] Y. Xia, Y. Xiong, B. Lim, S. Skrabalak, Shape-Controlled synthesis of metal nanocrystals: Simple chemistry meets complex physics? Angewandte Chemie (International Ed.) 48 (2008) 60-103.

[47] L. Dalton, A. Chen, A. Pyayt, B. Wiley, Y. Xia, Integration of photonic and silver nanowire plasmonic waveguides, Nature Nanotechnology 3 (2008) 660-665.

[48] M. Rang, A. Jones, F. Zhou, Z. Li, B. Wiley, Y. Xia, M. Raschke, Optical near-field mapping of plasmonic nanoprisms, Nano Letters 8 (2008) 3357-3363.

[49] X. Xia, J. Zeng, B. McDearmon, Y. Zheng, Q. Li, Y. Xia, Silver nanocrystals with concave surfaces and their optical and surface-enhanced raman scattering properties, Angewandte Chemie 123 (2011) 12750-12754.

[50] P. Christopher, S. Linic, Shape- and size-specific chemistry of ag nanostructures in catalytic ethylene epoxidation, ChemCatChem 2 (2010) 78-83.

[51] Y. Wang, Y. Zheng, C. Z. Huang, Y. Xia, Synthesis of ag nanocubes 18–32 nm in edge length: The effects of polyol on reduction kinetics, size control, and reproducibility, Journal of the American Chemical Society 135 (2013) 1941-1951.

[52] A. Tao, S. Habas, P. Yang, Shape control of colloidal metal nanocrystals, Small 4 (2008) 310-325.

[53] B. Wiley, S. H. Im, Z. Li, J. McLellan, A. Siekkinen, Y. Xia, Maneuvering the surface plasmon resonance of silver nanostructures through shape-controlled synthesis, The Journal of Physical Chemistry. B 110 (2006) 15666-15675.

[54] B. Wiley, Y. Sun, Y. Xia, Synthesis of silver nanostructures with controlled shapes and properties, Accounts of Chemical Research 40 (2007) 1067-1076.

[55] E. C. Le Ru and P. G. Etchegoin, *Principles of Surface-Enhanced Raman Spectroscopy.* (1st ed.) Amsterdam: Elsevier, 2009.

[56] S. Link, M. El-Sayed, Spectral properties and relaxation dynamics of surface plasmon electronic oscillations in gold and silver nanodots and nanorods, The Journal of Physical Chemistry. B 103 (1999) 8410-8426.

[57] Y. Xia, N. Halas, Shape-controlled synthesis and surface plasmonic properties of metallic nanostructures, MRS Bulletin 30 (2005) 338-348.

[58] M. Hu, C. Novo, A. Funston, H. Wang, H. Staleva, S. Zou, P. Mulvaney, Y. Xia, G. Hartland, Dark-field microscopy studies of single metal nanoparticles: Understanding the factors that influence the linewidth of the localized surface plasmon resonance, Journal of Materials Chemistry 18 (2008) 1949-196.

[59] J. Yguerabide, E. Yguerabide, Light-scattering submicroscopic particles as highly fluorescent analogs and their use as tracer labels in clinical and biological applications: I. theory, Analytical Biochemistry 262 (1998) 137-156.

[60] C. Cobley, M. Rycenga, F. Zhou, Z. Li, Y. Xia, Controlled etching as a route to high quality silver nanospheres for optical studies, Journal of Physical Chemistry. C 113 (2009) 16975-16982.

[61] Q. Zhang, W. Li, C. Moran, J. Zeng, J. Chen, L. Wen, Y. Xia, Seed-mediated synthesis of ag nanocubes with controllable edge lengths in the range of 30−200 nm and comparison of their optical properties, Journal of the American Chemical Society 132 (2010) 11372-11378.

[62] Y. Xia, S. Skrabalak, X. Li, L. Au, Facile synthesis of ag nanocubes and au nanocages, Nature Protocols 2 (2007) 2182-2190.

[63] A. Haes, C. Haynes, A. McFarland, G. Schatz, R. Van Duyne, S. Zou, Plasmonic materials for surface-enhanced sensing and spectroscopy, MRS Bulletin 30 (2005) 368-375.

[64] J. Aizpurua, G. Bryant, L. Richter, F. Garcia de Abajo, B. Kelley, T. Mallouk, Optical properties of coupled metallic nanorods for field-enhanced spectroscopy, Physical Review. B, Condensed Matter and Materials Physics 71 (2005) 235420.1-235420.13.

[65] S. Nie, S. Emory, Probing single molecules and single nanoparticles by surface-enhanced raman scattering, Science 275 (1997) 1102-1106.

[66] K. Kneipp, Y. Wang, H. Kneipp, L. Perelman, I. Itzkan, R. Dasari, M. Feld, Single molecule detection using surface-enhanced raman scattering (SERS), Physical Review Letters 78 (1997) 1667-1670.

[67] N. Liu, M. Mesch, T. Weiss, M. Hentschel, H. Giessen, Infrared perfect absorber and its application as plasmonic sensor, Nano Letters 10 (2010) 2342-2348.

[68] L. Sherry, S. Chang, G. Schatz, R. Van Duyne, B. Wiley, Y. Xia, Localized surface plasmon resonance spectroscopy of single silver nanocubes, Nano Letters 5 (2005) 2034-2038.

[69] J. Lassiter, F. McGuire, J. Mock, C. Ciracì, R. Hill, B. Wiley, A. Chilkoti, D. Smith, Plasmonic waveguide modes of film-coupled metallic nanocubes, Nano Letters 13 (2013) 5866-5872.

[70] J. Fan, C. Wu, K. Bao, J. Bao, R. Bardhan, N. Halas, V. Manoharan, P. Nordlander, G. Shvets, F. Capasso, Self-assembled plasmonic nanoparticle clusters, Science 328 (2010) 1135-1138.

[71] I. Romero, J. Aizpurua, G. Bryant, F. García De Abajo, Plasmons in nearly touching metallic nanoparticles: Singular response in the limit of touching dimers, Optics Express 14 (2006) 9988-9999.

[72] D. Kim, J. Heo, S. Ahn, S. W. Han, W. S. Yun, Z. H. Kim, Real-space mapping of the strongly coupled plasmons of nanoparticle dimers, Nano Letters 9 (2009) 3619-3625.

[73] L. Gunnarsson, T. Rindzevicius, J. Prikulis, B. Kasemo, M. Käll, S. Zou, G. Schatz, Confined plasmons in nanofabricated single silver particle pairs: Experimental observations of strong interparticle interactions, The Journal of Physical Chemistry. B 109 (2005) 1079-1087.

[74] X. Qian, J. Li, S. Nie, Stimuli-responsive SERS nanoparticles: Conformational control of plasmonic coupling and surface raman enhancement, Journal of the American Chemical Society 131 (2009) 7540-7541.

[75] X. Zhu, L. Shi, X. Liu, J. Zi, Z. Wang, A mechanically tunable plasmonic structure composed of a monolayer array of metal-capped colloidal spheres on an elastomeric substrate, Nano Res 3 (2010) 807-812.

[76] C. Mochizuki, H. Shinmori, Light-triggered assembly of gold nanorods based on photoisomerization of spiropyrans, Chemistry Letters 46 (2017) 469-472.

[77] S. Lim, J. Song, J. La, E. Cho, Gold nanospheres assembled on hydrogel colloids display a wide range of thermoreversible changes in optical bandwidth for various plasmonic-based color switches, Chemistry of Materials 26 (2014) 3272-3279.

[78] Y. Zhang, Q. Liu, H. Mundoor, Y. Yuan, I. Smalyukh, Metal nanoparticle dispersion, alignment, and assembly in nematic liquid crystals for applications in switchable plasmonic color filters and E-Polarizers, ACS Nano 9 (2015) 3097-3108.

[79] Q. Guo, C. Zhang, C. Wei, M. Xu, Y. Yuan, R. Gu, J. Yao, Controlling dynamic SERS hot spots on a monolayer film of Fe3O4@Au nanoparticles by a magnetic field, Spectrochimica Acta. Part A, Molecular and Biomolecular Spectroscopy 152 (2016) 336-342.

[80] Q. Fu, Z. Li, F. Fu, X. Chen, J. Song, H. Yang, Stimuli-responsive plasmonic assemblies and their biomedical applications, Nano Today 36 (2021) 101014.

[81] C. Li, M. Li, Z. Ni, Q. Guan, B. Blackman, E. Saiz, Stimuli-responsive surfaces for switchable wettability and adhesion, Journal of the Royal Society Interface 18 (2021) 20210162.

[82] G. Joshi, K. Blodgett, B. Muhoberac, M. Johnson, K. Smith, R. Sardar, Ultrasensitive photoreversible molecular sensors of azobenzene-functionalized plasmonic nanoantennas, Nano Letters 14 (2014) 532-540.

[83] Y. Zheng, J. Payton, C. Chung, R. Liu, S. Cheunkar, B. Pathem, Y. Yang, L. Jensen, P. Weiss, Surface-enhanced raman spectroscopy to probe reversibly photoswitchable azobenzene in controlled nanoscale environments, Nano Letters 11 (2011) 3447-3452.

[84] R. Klajn, P. Wesson, K. Bishop, B. Grzybowski, Writing Self-Erasing images using metastable nanoparticle “Inks”, Angewandte Chemie 48 (2009) 7035-7039.

[85] M. Suda, N. Kameyama, M. Suzuki, N. Kawamura, Y. Einaga, Reversible phototuning of ferromagnetism at au-S interfaces at room temperature, Angewandte Chemie (International Ed.) 47 (2008) 160-163.

[86] D. Sidhaye, S. Kashyap, M. Sastry, S. Hotha, B. Prasad, Gold nanoparticle networks with photoresponsive interparticle spacings, Langmuir 21 (2005) 7979-7984.

[87] C. Barrett, A. Natansohn, P. Rochon, Cis-trans thermal isomerization rates of bound and doped azobenzenes in a series of polymers, Chemistry of Materials 7 (1995) 899-903.

[88] S. Randhawa, "Active Control of Surface Plasmons in Hybrid Nanostructures." , Universitat Politècnica de Catalunya, Spain, 2012.

[89] K. Yager, C. Barrett, Novel photo-switching using azobenzene functional materials, Journal of Photochemistry and Photobiology. A, Chemistry. 182 (2006) 250-261.

[90] A. Priimägi, "Polymer-Azobenzene Complexes: From Supramolecular Concepts to Efficient Photoresponsive Polymers." , Helsinki University of Technology, Finland, 2009.

[91] P. Colomban, The use of metal nanoparticles to produce yellow, red and iridescent colour, from bronze age to present times in lustre pottery and glass: Solid state chemistry, spectroscopy and nanostructure, Journal of Nano Research 8 (2009) 109-132.

[92] H. Lochbihler, Polarizing and angle-sensitive color filter in transmittance for security feature applications, Advanced Optical Technologies 4 (2015) 71-77.

[93] T. Ming, H. Chen, R. Jiang, Q. Li, J. Wang, Plasmon-controlled fluorescence: Beyond the intensity enhancement, The Journal of Physical Chemistry Letters 3 (2012) 191-202.

[94] W. Lu, T. H. Chow, S. N. Lai, B. Zheng, J. Wang, Electrochemical switching of plasmonic colors based on polyaniline-coated plasmonic nanocrystals, ACS Applied Materials & Interfaces 12 (2020) 17733-17744.

[95] X. Zhuo, H. K. Yip, X. Cui, J. Wang, H. Lin, Colour routing with single silver nanorods, Light, Science & Applications 8 (2019) 39.

[96] N. Halas, S. Lal, W. Chang, S. Link, P. Nordlander, Plasmons in strongly coupled metallic nanostructures, Chemical Reviews 111 (2011) 3913-3961.

[97] M. Paunovic and M. Schlesinger, *Fundamentals of Electrochemical Deposition, Second Edition.* (2nd ed.) Wiley, 2006.

[98] S. Araki, K. Nakamura, K. Kobayashi, A. Tsuboi, N. Kobayashi, Electrochemical optical-modulation device with reversible transformation between transparent, mirror, and black, Advanced Materials 24 (2012) OP122-OP126.

[99] A. Tsuboi, K. Nakamura, N. Kobayashi, A localized surface plasmon resonance-based multicolor electrochromic device with electrochemically Size-Controlled silver nanoparticles, Advanced Materials 25 (2013) 3197-3201.

[100] G. Wang, X. Chen, S. Liu, C. Wong, S. Chu, Mechanical chameleon through dynamic real-time plasmonic tuning, ACS Nano 10 (2016) 1788-1794.

[101] A. Böhme, F. Sterl, E. Kath, M. Ubl, V. Manninen, H. Giessen, Electrochemistry on inverse copper nanoantennas: Active plasmonic devices with extraordinarily large resonance shift, ACS Photonics 6 (2019) 1863-1868.

[102] J. Lagerwall, G. Scalia, A new era for liquid crystal research: Applications of liquid crystals in soft matter nano-, bio- and microtechnology, Current Applied Physics 12 (2012) 1387-1412.

[103] G. Si, Y. Zhao, E. S. P. Leong, Y. J. Liu, Liquid-crystal-enabled active plasmonics: A review, Materials 7 (2014) 1296-1317.

[104] R. Mortimer, Electrochromic materials, Annual Review of Materials Research 41 (2011) 241-268.

[105] R. Mortimer, A. Dyer, J. Reynolds, Electrochromic organic and polymeric materials for display applications, Displays 27 (2006) 2-18.

[106] M. Miyata, H. Hatada, J. Takahara, Full-color subwavelength printing with gap-plasmonic optical antennas, Nano Letters 16 (2016) 3166-3172.

[107] N. Yu, F. Capasso, Flat optics with designer metasurfaces, Nature Materials 13 (2014) 139-150.

[108] K. Kumar, H. Duan, R. Hegde, S. Koh, J. Wei, J. Yang, Printing colour at the optical diffraction limit, Nature Nanotechnology 7 (2012) 557-561.

[109] X. Zhu, C. Vannahme, E. Højlund-Nielsen, N. Mortensen, A. Kristensen, Plasmonic colour laser printing, Nature Nanotechnology 11 (2016) 325-329.

[110] A. Moreau, C. Ciraci, J. Mock, R. Hill, Q. Wang, B. Wiley, A. Chilkoti, D. Smith, Controlled-reflectance surfaces with film-coupled colloidal nanoantennas, Nature 492 (2012) 86-89.

[111] M. Rozin, D. Rosen, T. Dill, A. Tao, Colloidal metasurfaces displaying near-ideal and tunable light absorbance in the infrared, Nature Communications 6 (2015) 7325.

[112] T. Ermatov, R. Noskov, A. Machnev, I. Gnusov, V. Atkin, E. Lazareva, S. German, S. Kosolobov, T. Zatsepin, O. Sergeeva, J. Skibina, P. Ginzburg, V. Tuchin, P. Lagoudakis, D. Gorin, Multispectral sensing of biological liquids with hollow-core microstructured optical fibres, Light, Science & Applications 9 (2020) 173.

[113] X. Wang, J. Zhu, H. Tong, X. Yang, X. Wu, Z. Pang, H. Yang, Y. Qi, A theoretical study of a plasmonic sensor comprising a gold nano-disk array on gold film with a SiO 2 spacer, Chinese Physics B 28 (2019) 44201.

[114] J. Zhu, X. Wang, Y. Wu, Y. Su, T. Jia, H. Yang, L. Zhang, Y. Qi, X. Wen, Plasmonic refractive index sensors based on one- and two-dimensional gold grating on a gold film, Photonic Sensors 10 (2020) 375-386.

[115] C. Farcau, D. Marconi, A. Colniță, I. Brezeștean, L. Barbu-Tudoran, Gold nanopost-shell arrays fabricated by nanoimprint lithography as a flexible plasmonic sensing platform, Nanomaterials 9 (2019) 1519.

[116] Z. Yan, C. Tang, G. Wu, Y. Tang, P. Gu, J. Chen, Z. Liu, Z. Huang, Perfect absorption and refractive-index sensing by metasurfaces composed of cross-shaped hole arrays in metal substrate, Nanomaterials 11 (2020) 63.

[117] P. Mandal, H-shape plasmonic metasurface as refractive index sensor, Plasmonics 10 (2015) 439-445.

[118] Q. Zhang, W. Li, L. Wen, J. Chen, Y. Xia, Facile synthesis of ag nanocubes of 30 to 70 nm in edge length with CF3COOAg as a precursor, Chemistry : A European Journal 16 (2010) 10234-10239.

[119] W. Li, P. Camargo, X. Lu, Y. Xia, Dimers of silver nanospheres: Facile synthesis and their use as hot spots for surface-enhanced raman scattering, Nano Letters 9 (2009) 485-490.

[120] Y. Yang, S. Matsubara, L. Xiong, T. Hayakawa, M. Nogami, Solvothermal synthesis of multiple shapes of silver nanoparticles and their SERS properties, Journal of Physical Chemistry. C 111 (2007) 9095-9104.

[121] M. Tran, S. Centeno, J. Hutchison, H. Engelkamp, D. Liang, G. Van Tendeloo, B. Sels, J. Hofkens, H. Uji-i, Control of surface plasmon localization via self-assembly of silver nanoparticles along silver nanowires, Journal of the American Chemical Society 130 (2008) 17240-17241.

[122] M. Mahmoud, C. Tabor, M. El-Sayed, Surface-enhanced raman scattering enhancement by aggregated silver nanocube monolayers assembled by the Langmuir−Blodgett technique at different surface pressures, Journal of Physical Chemistry. C 113 (2009) 5493-5501.

[123] R. Near, S. Hayden, M. El-Sayed, Extinction vs absorption: Which is the indicator of plasmonic field strength for silver nanocubes? Journal of Physical Chemistry. C 116 (2012) 23019-23026.

[124] R. Alaee, C. Menzel, U. Huebner, E. Pshenay-Severin, S. Bin Hasan, T. Pertsch, C. Rockstuhl, F. Lederer, Deep-subwavelength plasmonic nanoresonators exploiting extreme coupling, Nano Letters 13 (2013) 3482-3486.

[125] T. Smith, J. Guild, The C.I.E. colorimetric standards and their use, Transactions of the Optical Society 33 (1931) 73-134.

[126] O. Tanchak, C. Barrett, Swelling dynamics of multilayer films of weak polyelectrolytes, Chemistry of Materials 16 (2004) 2734-2739.

[127] Y. Lvov, G. Decher, H. Moehwald, Assembly, structural characterization, and thermal behavior of layer-by-layer deposited ultrathin films of poly(vinyl sulfate) and poly(allylamine), Langmuir 9 (1993) 481-486.

[128] Z. Adamczyk, M. Zembala, P. Warszyński, B. Jachimska, Characterization of polyelectrolyte multilayers by the streaming potential method, Langmuir 20 (2004) 10517-10525.

[129] J. Wong, F. Rehfeldt, P. Hänni, M. Tanaka, R. Klitzing, Swelling behavior of polyelectrolyte multilayers in saturated water vapor, Macromolecules 37 (2004) 7285-7289.

[130] M. Lösche, J. Schmitt, G. Decher, W. Bouwman, K. Kjaer, Detailed structure of molecularly thin polyelectrolyte multilayer films on solid substrates as revealed by neutron reflectometry, Macromolecules 31 (1998) 8893-8906.

[131] Y. Lvov, G. Decher, H. Moehwald, Assembly, structural characterization, and thermal behavior of layer-by-layer deposited ultrathin films of poly(vinyl sulfate) and poly(allylamine), Langmuir 9 (1993) 481-486.

[132] J. Wong, F. Rehfeldt, P. Hänni, M. Tanaka, R. Klitzing, Swelling behavior of polyelectrolyte multilayers in saturated water vapor, Macromolecules 37 (2004) 7285-7289.

[133] A. Natansohn, P. Rochon, M. Pezolet, P. Audet, D. Brown, S. To, Azo polymers for reversible optical storage. 4. cooperative motion of rigid groups in semicrystalline polymers, Macromolecules 27 (1994) 2580-2585.

[134] R. Hagen, T. Bieringer, Photoaddressable polymers for optical data storage, Advanced Materials 13 (2001) 1805-1810.

[135] D. Yakubovsky, A. Arsenin, Y. Stebunov, D. Fedyanin, V. Volkov, Optical constants and structural properties of thin gold films, Optics Express 25 (2017) 25574-25587.

[136] G. Rosenblatt, B. Simkhovich, G. Bartal, M. Orenstein, Nonmodal plasmonics: Controlling the forced optical response of nanostructures, Physical Review. X 10 (2020) 011071.

[137] D. Y. Kim, S. K. Tripathy, L. Li, J. Kumar, Laser-induced holographic surface relief gratings on nonlinear optical polymer films, Applied Physics Letters 66 (1995) 1166-1168.

[138] P. Rochon, E. Batalla, A. Natansohn, Optically induced surface gratings on azoaromatic polymer films, Applied Physics Letters 66 (1995) 136-138.

[139] F. Lagugné-Labarthet, J. Bruneel, T. Buffeteau, C. Sourisseau, Chromophore orientations upon irradiation in gratings inscribed on azo-dye polymer films: A combined AFM and confocal raman microscopic study, The Journal of Physical Chemistry. B 108 (2004) 6949-6960.

[140] F. Lagugné-Labarthet, J. Bruneel, V. Rodriguez, C. Sourisseau, Chromophore orientations in surface relief gratings with second-order nonlinearity as studied by confocal polarized raman microspectrometry, The Journal of Physical Chemistry. B 108 (2004) 1267-1278.

[141] S. Bian, L. Li, J. Kumar, D. Y. Kim, J. Williams, S. K. Tripathy, Single laser beam-induced surface deformation on azobenzene polymer films, Applied Physics Letters 73 (1998) 1817-1819.

[142] N. Viswanathan, S. Balasubramanian, L. Li, S. Tripathy, J. Kumar, A detailed investigation of the polarization-dependent surface-relief-grating formation process on azo polymer films, Japanese Journal of Applied Physics 38 (1999) 5928-5937.

[143] J. A. Delaire, K. Nakatani, Linear and nonlinear optical properties of photochromic molecules and materials, Chemical Reviews 100 (2000) 1817-1846.

[144] N. Viswanathan, D. Yu Kim, S. Bian, J. Williams, W. Liu, L. Li, L. Samuelson, J. Kumar, S. Tripathy, Surface relief structures on azo polymer films, Journal of Materials Chemistry 9 (1999) 1941-1955.

[145] A. Natansohn, P. Rochon, Photoinduced motions in azo-containing polymers, Chemical Reviews 102 (2002) 4139-4176.

[146] P. Rochon, Optically inscribed volume or surface structures in azobenzene polymer films, Opt. Spectrosc 103 (2007) 858-861.

[147] T. Srikhirin, A. Laschitsch, D. Neher, D. Johannsmann, Light-induced softening of azobenzene dye-doped polymer films probed with quartz crystal resonators, Applied Physics Letters 77 (2000) 963.

[148] N. Mechau, D. Neher, V. Börger, H. Menzel, K. Urayama, Optically driven diffusion and mechanical softening in azobenzene polymer layers, Applied Physics Letters 81 (2002) 4715-4717.

[149] N. Mechau, M. Saphiannikova, D. Neher, Dielectric and mechanical properties of azobenzene polymer layers under visible and ultraviolet irradiation, Macromolecules 38 (2005) 3894-3902.

[150] K. Yager, C. Barrett, Temperature modeling of laser-irradiated azo-polymer thin films, The Journal of Chemical Physics 120 (2004) 1089-1096.

[151] P. Lefin, C. Fiorini, J. Nunzi, Anisotropy of the photoinduced translation diffusion of azo-dyes, Optical Materials 9 (1998) 323-328.

[152] P. Lefin, C. Fiorini, J. Nunzi, Anisotropy of the photo-induced translation diffusion of azobenzene dyes in polymer matrices, Journal of the European Optical Society. Part A, Pure and Applied Optics 7 (1998) 71-82.

[153] T. Pedersen, P. Johansen, Mean-field theory of photoinduced molecular reorientation in azobenzene liquid crystalline side-chain polymers, Physical Review Letters 79 (1997) 2470-2473.

[154] T. Pedersen, P. Johansen, N. Holme, P. Ramanujam, S. Hvilsted, Mean-field theory of photoinduced formation of surface reliefs in side-chain azobenzene polymers, Physical Review Letters 80 (1998) 89-92.

[155] C. Barrett, A. Natansohn, P. Rochon, Mechanism of optically inscribed high-efficiency diffraction gratings in azo polymer films, Journal of Physical Chemistry 100 (1996) 8836-8842.

[156] C. Barrett, P. Rochon, A. Natansohn, Model of laser-driven mass transport in thin films of dye-functionalized polymers, The Journal of Chemical Physics 109 (1998) 1505-1516.

[157] D. Bergman, M. Stockman, Surface plasmon amplification by stimulated emission of radiation: Quantum generation of coherent surface plasmons in nanosystems, Physical Review Letters 90 (2003) 027402.

[158] H. Chorsi, Y. Lee, A. Alù, J. Zhang, Tunable plasmonic substrates with ultrahigh Q-factor resonances, Scientific Reports 7 (2017) 15985-9.

[159] O. Bitton, S. N. Gupta, Y. Cao, A. Vaskevich, L. Houben, T. Yelin, G. Haran, Improving the quality factors of plasmonic silver cavities for strong coupling with quantum emitters, The Journal of Chemical Physics 154 (2021) 014703.

[160] K. Li, Y. Wang, K. Jiang, Y. Ren, Y. Dai, Y. Lu, P. Wang, Large-area, reproducible and sensitive plasmonic MIM substrates for surface-enhanced raman scattering, Nano 27 (2016) 495402.

[161] V. K. Lin, S. L. Teo, R. Marty, A. Arbouet, C. Girard, E. Alarcon-Llado, S. H. Liu, M. Y. Han, S. Tripathy, A. Mlayah, Dual wavelength sensing based on interacting gold nanodisk trimers, Nanotechnology 21 (2010) 305501.

[162] Z. Wu, G. Kelp, M. Yogeesh, W. Li, K. McNicholas, A. Briggs, B. Rajeeva, D. Akinwande, S. Bank, G. Shvets, Y. Zheng, Dual-band moiré metasurface patches for multifunctional biomedical applications, Nanoscale 8 (2016) 18461-18468.

[163] Y. Jung, S. Sung, K. Lee, S. Surabhi, J. Jeong, E. Lee, J. Choi, J. Jeong, Configurable plasmonic substrates from heat-driven imprint-transferred ag nanopatterns for enhanced photoluminescence, RSC Advances 5 (2015) 547-553.

[164] A. Naweed, F. Baumann, W. Bailey, A. Karakashian, W. Goodhue, Evidence for radiative damping in surface-plasmon-mediated light transmission through perforated conducting films, Journal of the Optical Society of America. B, Optical Physics 20 (2003) 2534.

[165] M. Hill, M. Marell, E. Leong, E. Smalbrugge, Y. Zhu, M. Sun, v. Veldhoven, E. Geluk, F. Karouta, Y. Oei, R. Nötzel, C. Ning, M. Smit, Lasing in metal-insulator-metal sub-wavelength plasmonic waveguides, Optics Express 17 (2009) 11107-11112.

[166] Z. Madadi, K. Abedi, G. Darvish, M. Khatir, An infrared narrow-band plasmonic perfect absorber as a sensor, Optik 183 (2019) 670-676.

Appendices

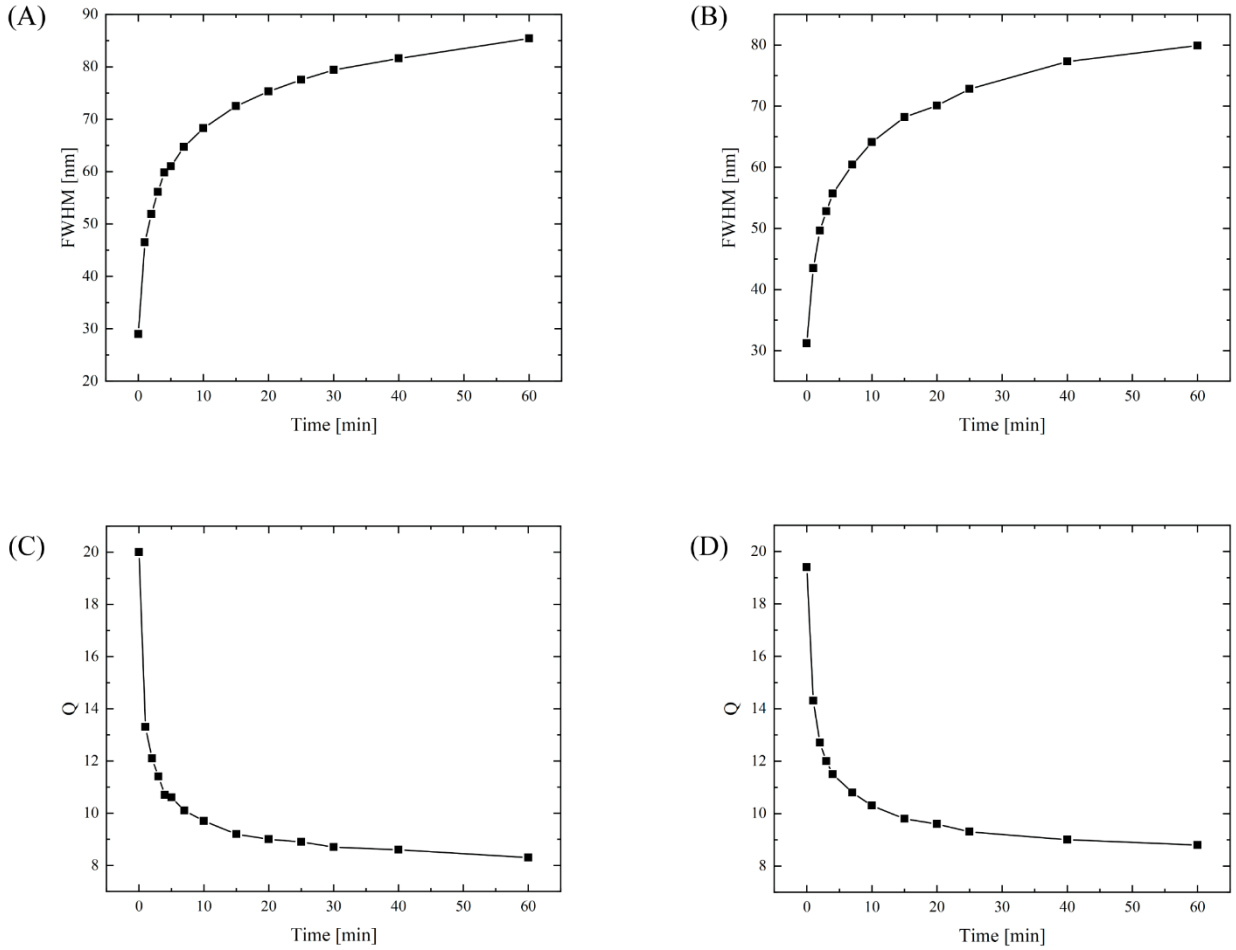

Figure A.1. Effect of the irradiation on the *FWHM* of DR1 samples plotted against time scale under: **(A)** Linearly polarized light; and **(B)** Circularly polarized light. Effect of the irradiation on the *Q* of DR1 samples plotted against time scale under: **(C)** Linearly polarized light; and **(D)** Circularly polarized light.

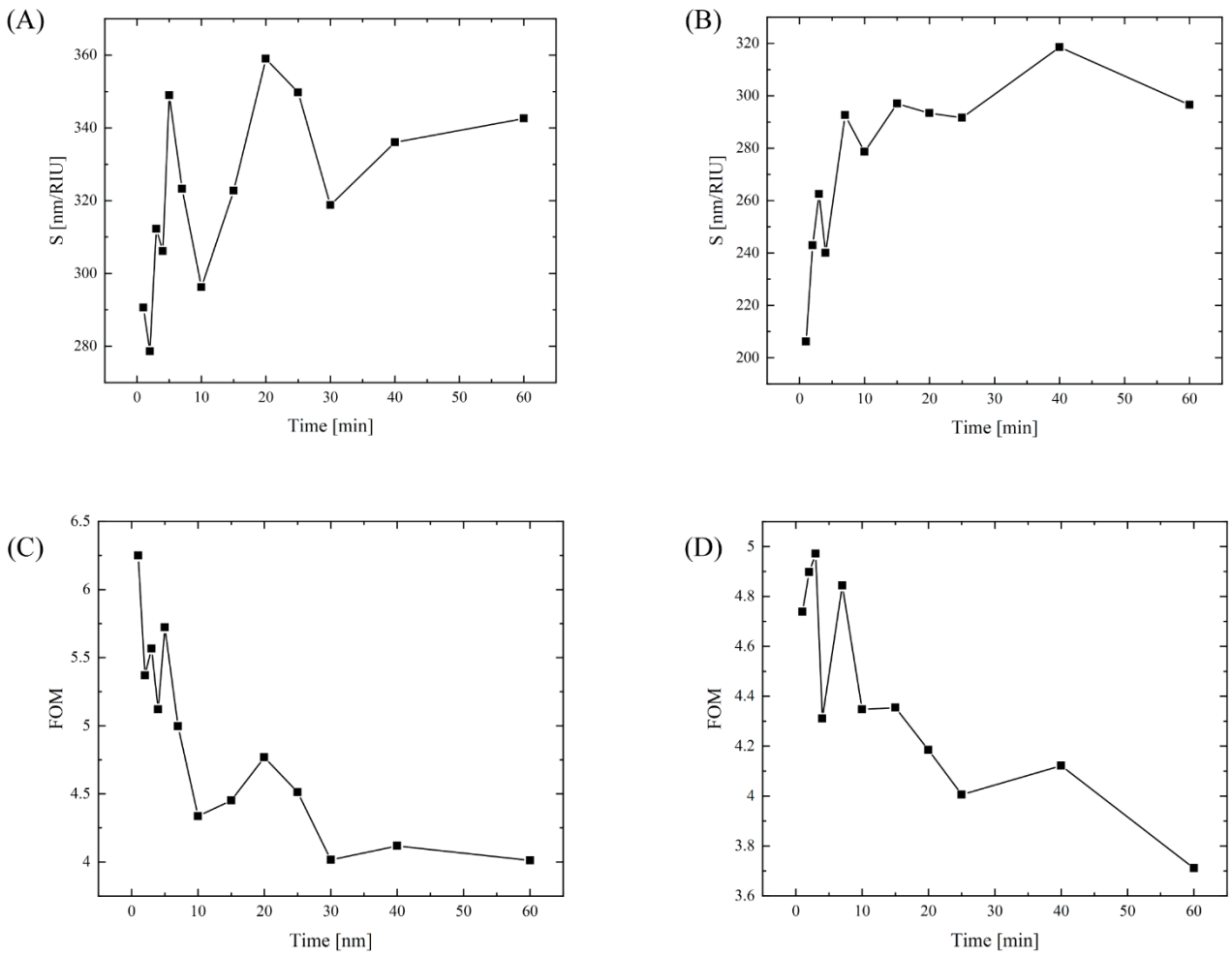

Figure A.2. Effect of the irradiation on the *S* of DR1 samples plotted against time scale under: **(A)** Linearly polarized light; and **(B)** Circularly polarized light. Effect of the irradiation on the *FOM* of DR1 samples plotted against time scale under: **(C)** Linearly polarized light; and **(D)** Circularly polarized light.

Table A.1. Data for the DR1 sample exposed initially to linearly polarized light for 60 min then circularly polarized light for 20 min.

Linear Polarizer							
Exposure Time [min]	*λ_r [nm]*	*FWHM [nm]*	*Q*	*η*	*k*	*S [nm/RIU]*	*FOM*
0	600	29	20	0.56144	0.82422	-	-
1	620	46.5	13.3	0.63027	0.88534	290.570972	6.248838107
2	630	51.9	12.1	0.66912	0.92988	278.6032689	5.3680784
3	638	56.1	11.4	0.68313	0.93818	312.2688799	5.566290195
4	642	59.8	10.7	0.69863	0.94963	306.1447627	5.119477638
5	648	61	10.6	0.69897	0.95428	349.0147604	5.721553449
7	654	64.7	10.1	0.7285	1.01246	323.2371603	4.995937563
10	660	68.3	9.7	0.76401	1.07787	296.1939083	4.336660443
15	670	72.5	9.2	0.77835	1.05889	322.7144899	4.451234343
20	680	75.3	9	0.78428	1.08109	359.0019745	4.767622503
25	686	77.5	8.9	0.80733	1.10926	349.7498882	4.512901783
30	688	79.4	8.7	0.83748	1.12855	318.7943776	4.015042539
40	698	81.6	8.6	0.85308	1.15309	336.0307228	4.118023564
60	712	85.4	8.3	0.88837	1.22957	342.5809806	4.011486893
Reverse with Circular Polarizer							
10	714	86.1	8.3	0.91235	1.24334	311.2444117	3.614917674
20	718	87.3	8.2	0.92993	1.3044	307.277628	3.519789554

Table A.2. Data for the DR1 sample exposed initially to circularly polarized light for 60 min then linearly polarized light for 20 min.

Circular Polarizer							
Exposure Time [min]	*λ_r [nm]*	*FWHM [nm]*	*Q*	*η*	*k*	*S [nm/RIU]*	*FOM*
0	604	31.2	19.4	0.55893	0.96534	-	-
1	620	43.5	14.3	0.63656	1.0229	206.1058869	4.738066366
2	630	49.6	12.7	0.66596	1.00882	242.9225451	4.897631957
3	636	52.8	12	0.68086	1.02167	262.4456655	4.970561847
4	640	55.7	11.5	0.70888	1.05036	240.0800267	4.310233872
7	652	60.4	10.8	0.723	1.11129	292.5580545	4.843676399
10	658	64.1	10.3	0.75273	1.11363	278.6377709	4.346923103
15	668	68.2	9.8	0.77442	1.12062	296.9975405	4.354802646
20	674	70.1	9.6	0.79755	1.1518	293.353449	4.184785292
25	680	72.8	9.3	0.81955	1.19671	291.6123091	4.005663587
40	694	77.3	9	0.84142	1.23019	318.5953485	4.121543965
60	704	79.9	8.8	0.89619	1.30391	296.5071458	3.710978045
Reverse with Linear Polarizer							
10	710	83	8.6	0.90364	1.30967	307.5048592	3.704877821
20	716	83.3	8.6	0.89471	1.27047	333.5517303	4.004222453